Sound Velocity And Internal Friction In Disordered Magnetic Alloys

Thesis submitted for the degree of

Doctor of Philosophy (Science)

in

Physics (Experimental)

by

Md Sarowar Hossain

Department of Physics

University of Calcutta

October 2019

To my Daughter.....

Samara Mahveen Aizah

Acknowledgements

The journey of a Ph.D. thesis work takes place in such an important phase of life that it shapes not only one's professional career but every aspects of life and I guess this is true for everyone pursuing a Ph.D. degree. My journey, albeit little longer than usual, has been a colourful, memorable and enjoyable one. I would like to take this opportunity to express my sincere gratitude to all those people who have guided me, motivated me and made this journey wonderful.

First and foremost, I would like to express my sincere gratitude to my supervisor Prof. Pratip Kr. Mukhopadhyay. It is his guidance which always kept me on the right track of the problem and his continuous enthusiasm and encouragement kept me motivated to complete this dissertation. His insistence with long-enduring patience on clarity and critical thinking improve the quality by bringing out various different aspects of the problems and made them presentable in an organized manner. His knowledge and ideas of setting up various experimental methods have always inspired me. Working with him was a rewarding experience and I am indebted to him for the freedom he has given me in exploring various scientific ideas.

I am thankful to TWAS, the academy of sciences for the developing world for awarding me the TWAS–Bose fellowship to pursue the Ph.D degree. I sincerely acknowledge the Directors of S N Bose National Centre for allowing me to carry my research work in this institute. I would like to deeply acknowledge Dean, Academic program, SNBNCBS for his continuous help for solving the visa and other academic related problems. Herewith I also acknowledge I sincerely acknowledge S. N. Bose National Centre for Basic Sciences for providing the opportunity and financial support to carry out this thesis work.

I owe my deepest gratitude to Prof. Priya Mahadevan, SNBNCBS for officiating supervise along with my thesis supervisor. I am grateful to Prof. M A Hakim, Dr. Sheikh Manjura Hoque and Prof. M A Basith for their collaboration and support during my journey of Ph.D life.

I am thankful to Prof. Madhusudan Roy and Prof. Barnana Pal, Saha Institute of Nuclear Physics for allowing me to do experiments in their lab. I am also thankful to Dr. Thirupathaiah Setti and Atindra Nath Pal for patiently waiting for me to finish experimentats in the laboratory.

I have been fortunate to have the company of Injamamul Arief introduced me to the various experimental set-up in the laboratory. He helped me with his expert advice

and unparalleled help from the initial stage of stay here in Kolkata. I am thankful to my lab senior Tanmoy Ghosh for his great support for learning to run the CCR and to write Labview program and also he helped me to analyze the low temperature resistivity data. It is my pleasure to thank my past and present lab-mates Sandeep Agarwal, Alo di, Tapas da, Abhishek Bagchi, Gurdeep Singh, Suman Sarker, Vinodh, Bishal Keshari, Dr. B. Rajini Kanth for providing a cooperative, pleasant and joyful atmosphere in the laboratory. Abhishek Bagchi and Gurdeep Singh helped me a lot for the correction of the thesis. Sandeep da helped me to analyze the magnetic data. Alo di helped me to learn the Reitveld refinement. I am warmly acknowledging Dipayan, Joy, Urmi di, Amit and Shakti Da for supporting with technical cell for experimental measurements.

I am pleased to acknowledge the one and only band group at SNBNCBS named "SNB Khaja Band" and the group members of the band which continuously encouraged me to remove monopolistic attitude during the Ph.D tenure. I would also like to acknowledge "Gobeshak Bandhugon" group and the group members, Deba, Subrata, Lalu, Somnath, Souvonik, Arindam da, Kartik, Aslam and Shirsendu.

I must also thanks the my seniors Subashis da, Pratik da and Pandey ji for their supports. I am thanking to Rabi and Anirban for their continuous support. I also thankful to Ejaj Tarif, Mehbub, Emadul, Ankan, Rajkumar Shadhu, Anindita, Saniur and Sudipta (Poti) and I have passed a great time along with them. I must show the gratitudes to all other juniors, Prantik, Debu, Juriti, Keshab, Purushottam, Atanu, Piklu, Shashank, Dhiraj, Ritam, Tuhin, Sayan Rauth and Sayan Pal, Edwin Tendong, Raghu, Jayita, Riju Pal, Shubham, Indranil, Subrata and Dipanjan, Abhishek Maiti, Partha, Saikat and Rahul Bandyopadhyay,

Finally, I would like to thank my parents and sister for their unconditional love and support which have been the pillars of my strength and made this journey possible. Their continuous enthusiasm and encouragement in my academic endeavours helped me to tread the path I have travelled so far. And also I am very much thankful to my wife Sanjeda Afreen for her continuous enthusiasm and encouragement of doing research work.

Md. Sarowar Hossain

Kolkata

September 2019

List of publications

1. **Effect of Annealing on Elastic Moduli of a FSMA**
   Md Sarowar Hossain, B. Rajini Kanth and P. K. Mukhopadhyay, Shap. Mem. Superelasticity, **3**, 199-205 (2017)

2. **Interesting low temperature magneto-elastic behavior of a FINEMET metglass**
   Md. Sarowar Hossain, M. A. Hakim and P. K. Mukhopadhyay; AIP Advances., **7**, 115221 (2017)

3. **Ultrasonic Characterization of Newtonian and Non-newtonian Fluids**
   Md Sarowar Hossain, Barnana Pal and P. K. Mukhopadhyay; Universal Journal of Physics and Application. **12(3)**, 41-46 (2018)

4. **Effect of annealing on the structural and magnetic properties of CoNiAl FSMA**
   Md Sarowar Hossain, Tanmoy Ghosh, B. Rajini Kanth, and P.K. Mukhopadhyay; Cryst. Res. Technol. **1800153**, 1-6 (2019)

5. **Correlation of dynamic elastic properties of a heat treated CoNiAl alloy system with its microstructural changes**
   Md. Sarowar Hossain, Gokul P, Barnana Pal and P K Mukhopadhyay, Shap. Mem. Superelasticity, (accepted, 2019).

6. **Size dependent magnetic and electrical properties of Ba-doped nanocrystalline BiFeO3**
   Mehedi Hasan, M. A. Hakim, M. A. Basith, Md. Sarowar Hossain, Bashir Ahmmad, M. A. Zubair, A. Hussain, and Md. Fakhrul Islam; AIP Advances, **6**, 035314 (2016)

7. **Saturation magnetization and band gap tuning in BiFeO3 nanoparticles via co-substitution of Gd and Mn**
   Mehedi Hasan, M.A. Basith, M.A. Zubair, Md. Sarowar Hossain, Rubayyat Mahbub, M.A. Hakim, Md. Fakhrul Islam, J. Alloys. Compds., **687**, 701-706 (2016)

8. **A soft chemical route to the synthesis of BiFeO3 nanoparticles with enhanced magnetization**

   Mehedi Hasan, Md. Fakhrul Islam, Rubayyat Mahbub, Md. Sarowar Hossain, M.A. Hakim, Materials Research Bulletin, **73**, 179–186 (2016)

9. **Preparation of high crystalline nanoparticles of rare-earth based complex pervoskites and comparison of their structural and magnetic properties with bulk counterparts**

   M. A. Basith, M. A. Islam, Bashir Ahmmad, Md. Sarowar Hossain and K Mølhave, Mater. Res. Express, **4**, 075012 (2017)

10. **Effect of CePO4 on structural, magnetic and optical properties of ceria nanoparticles**

    Md Abdullah Al Mamun, Manifa Noor, A K M Atique Ullah, Md. Sarowar Hossain, Matin Abdul, Fakhrul Islam and M A Hakim, Mater. Res. Express, **6**, 016102, (2019)

11. **Effect of Co addition to the dynamic elastic ptoperties in CoNiAl FSMA system.**

    Md. Sarowar Hossain and P. K. Mukhopadhyay

    Under Preparation

12. **Stress locked Martensitic transformation in a CoNiAl Ferromagnetic Shapememory alloys**

    Md. Sarowar Hossain, B. Rajini Kanth and P K Mukhopadhyay

    Under Preparation

13. **Magnetic field induced sound velocity and internal friction in a CoNiAl FSMA in vicinity of different stress level.**

    Md. Sarowar Hossain and P K Mukhopadhyay

    Under Preparation.

14. **Low temperature magneto-mechanical properties in Nb and Cr doped Finemet alloys.**

    Md. Sarowar Hossain and P K Mukhopadhyay

    Under Preparation.

Table of Content

List of Tables

List of figures

List of Abbreviations

SMA	Shape memory alloy
MT	Martensitic transition
MS, MF, AS, AF	Martensitic start, Martensitic finish, Austenitic start and Austenitic finish temperatures
FSMA	Ferromagnetic shape memory alloys
IF	Internal Friction
SV	Sound Veloctiy
e/a	Valence electron concentration per atom
FM	Ferromagnetic
T_C^A	Curie temperature at Austenite phase
M (T)	Temperature dependent magnetization measurement
EDAX	energy dispersive x-ray analysis
XRD	X-ray diffraction
DSC	differential scanning calorimetric
SEM	Scanning electron microscope
H	Magnetic field
M	Magnetization
χ'	Real part of liner ac susceptibility
χ''	Imaginary part of liner ac susceptibility
GPIB	General Purpose Interface Bus
VSM	Vibrating sample magnetometer
ZFC	Zero-field-cooled
FC	Field-cooled
FH	Fierromagnetic high
FL	Ferromagnetic Low
VBR	Vibrating Reed

Chapter 1

Introduction

In this chapter, we introduce the topic and give the motivation for the work undertaken in the thesis. We provide a general discussion for the background of the subjects.

1.1. Ordered and Disordered Magnetic Alloys:

A magnetic alloy is a solid composed of one or more metals with metals or non-metallic elements and contains at least one magnetic element such as Fe, Co or Ni. Based on the atomic arrangements, magnetic alloys are crystallized into ordered and disordered phases where disordered phases include substitutional, interstitial defects or amorphous structures.

In any ordered alloy crystal, the lattice sites can be described by $R_i = N_1 a_1 + N_2 a_2 + N_3 a_3$ where N_1, N_2, N_3 are all integers or half integers and a_1, a_2, a_3 are the lattice parameters. Each lattice site will be occupied by a particular type of chemical species with a probability $P(R_i)$ of one or zero. For example, NiAl alloy of B2 structure is a well known ordered magnetic alloy shown in Fig. 1.1 (a). There are also fcc based ordered structures such as $L1_2$ (example: Ni_3Al) and $L1_0$ (example: CuAu).

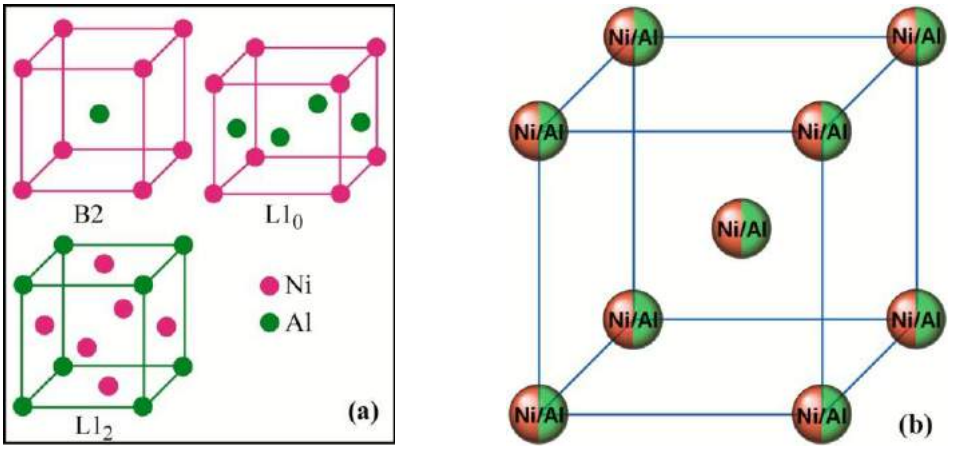

Figure 1.1: (a) Examples of ordered alloys of B2, $L1_0$ and $L1_2$ Structure. (b) Cubic A2 NiAl.

The substitution type disordered alloys are formed when dislocation takes place in any ordered phase. In such alloy the constituent atoms in the alloy randomly occupy the lattice sites [1-3] with $P(R_i) = 0.5$. NiAl of A2 structure is an example of a substitutional type disordered magnetic alloy shown in Fig. 1.1 (b). Sometimes, the low temperature ordered phase of an alloy transforms into a substitutional type disordered alloy at higher temperatures, known as order-disorder transformation [1-3]. During order-disorder transition as temperature increases, short-range order may take place along with the long-range order due to atomic diffusion into a wrong site. Instead of whole lattice, the substitutional disorder may be found in a selective portion of the lattice of any system such as Heusler alloys shown in Fig. 1.2.

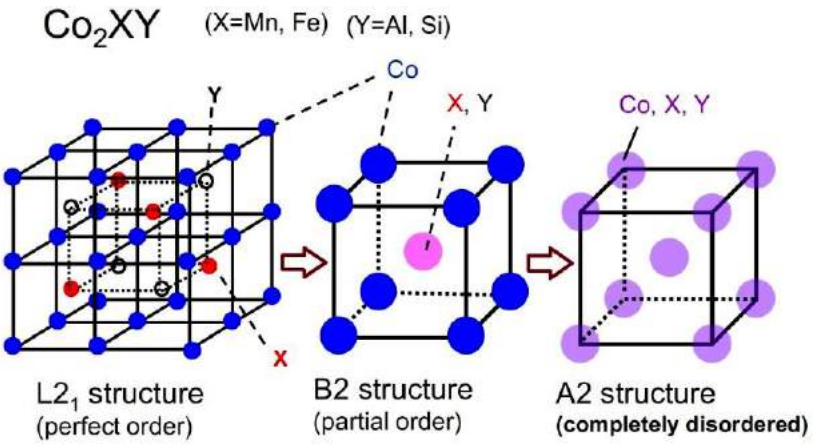

Figure 1.2: Order-Disorder transition in a Co-based full Heusler alloy; $L2_1$ is the perfectly ordered structure; B2 the partially ordered structure, in which the body centre sites are occupied randomly by X or Y atoms; and A2 completely disordered bcc structure. Image source Ref. [4].

In case of large size difference between the constituent atoms in any alloy, the smaller atoms become trapped in the spaces between the other atoms in the crystal matrix, called the interstices. Such alloys are known as interstitial alloys [5]. Fig. 1.3 (a) shows the interstitial mechanism. By Hume-Rothery Rules, solute atoms should have radius no larger than 15% of the radius of solvent atoms in any interstitial solid solutions.

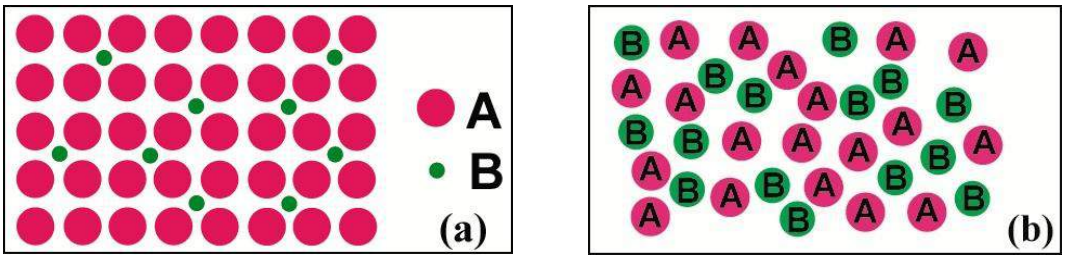

Figure 1.3: (a) Interstitial mechanism in a binary alloy AB; B atom is of sufficiently small radius to sit in interstitial positions of the lattice. (b) Atomic arrangements in an Amorphous AB alloy

Another type of alloys without any specific atomic configuration and defect are entirely different from any other alloys. It is known as amorphous alloy that are non-crystalline and have a glass-like structure [6]. Amorphous alloys have much lower electrical conductivity than corresponding crystalline variants. Fig. 1.3 (b) shows the randomness of the atoms in an amorphous alloy. Amorphous metals can be produced by different ways, like extremely rapid cooling, physical vapor deposition, solid-state reaction, ion irradiation, mechanical alloying, etc. [7]. The first reported metallic glass was an alloy ($Au_{75}Si_{25}$) produced at Caltech by W. Klement, R. H. Willens and Pol Duwez in 1960 [8].

1.2. Ferromagnetic Shape-memory alloy:

Ferromagnetic shape memory alloys (FSMA) is a fascinating class of shape memory alloys (SMA) for its ferromagnetic nature along with shape memory effect. The shape memory properties in these alloys can also be controlled by magnetic field apart from the thermal and stress control like only SMA [9, 10]. The most standard FSMA material is Ni-Mn-Ga full Heusler alloy, which is used to understand the conditions and mechanisms for ferromagnetic shape memory effect. The Ni based alloy of composition Ni_2MnGa is the most studied FSMA [11, 12] material. Over the years researchers developed the new FSMAs such as Fe-Pd [13], Fe_3Pt [14], Fe-Ni-Co-Ti, Ni-Fe-Al [15], and Co-Ni-Ga [16, 17]. Based on twin martensite variants remigration, different Ni based alloy like Ni-Mn-Ga [18-20], Mn-Ni-Sn [21] and Ni-Fe-Ga [22, 23] achieved more than 10% giant stain. However, the actuator and sensor made of FSMAs did not get a wide range of applications due to their low phase transition temperature and poor mechanical properties [24]. In the FSMAs family, recently developed Co-Ni-Al alloy overcame all of the barriers to the application with wide range phase transition temperature, superior mechanical strength and good hot/cold workability (ductility) [25, 26]. This happens due to the growth of non-FSMA γ phase precipitates as intergrain component of the main β (B2) phase grains of the FSMA material. The ratio of β to γ phase components can be changed by preparation and annealing conditions, due to alteration of grain and intergrain microstructure, thus even affecting structural transformation (B2 to $L1_0$) temperature range (90K to 390K) [26, 27].

Ferromagnetic shape memory alloys have the structure of Hesler alloys. Heusler alloy was first discovered in the form X_2YZ known as full Heusler where X is transition metal similarly Y is also a transition metal and Z lies in the p-block of the periodic table.

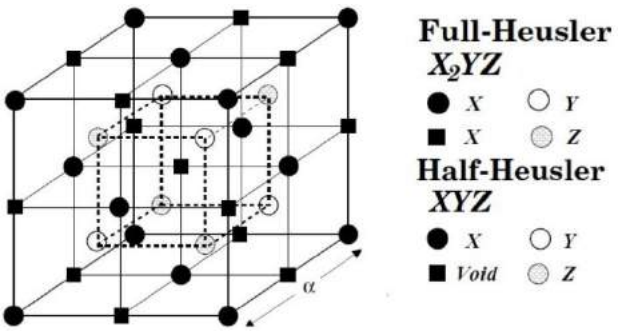

Figure1.4: Structures adapted by the half- and full-Heusler alloys. In ternary half-Heusler alloy (XYZ) X, Y and Z atoms are placed at (0,0,0), (¼,¼,¼) and (¾,¾,¾) respectively whereas in full-Heusler alloy (X_2YZ), the vacant site (½,½,½) is occupied by X atom. Image source Ref. [32]

X_2YZ alloy crystallizes in the $L2_1$ structure with four fcc sublattices where two of the four sublattices are occupied by the same type of X atoms, while Y and Z occupy the remaining two. In later another type, named half heusler alloy in the form XYZ was noticed. In contrast to full Heusler alloy, one sublattice remains unoccupied in the half Heusler alloy. These structures are shown in Fig. 1.4. In stable structure of a half-Heusler alloy X and Y atoms are located at the A(0,0,0) and B(¼,¼,¼) Wyckoff positions and the Z atom is located at the D(3/4,3/4,3/4) position respectively, leaving the C(½,½,½) position unoccupied [28–31] whereas in full-Heusler alloy C(½,½,½) is occupied by the X atom.

1.3. Some unique properties of FSMA:

1.3.1. Shape memory effect:

Shape memory effect (SME) is a phenomenon, in which an alloy by itself can recover the deformed shape into the pre-deformed (original) shape when temperature is increased and the alloy is known as shape memory alloy (SMA). A first-order diffusionless structural phase transition from the high temperature austenite phase to the low temperature martensite phase, known as martensitic transition (MT) which occurs via shear lattice distortion, plays the key role in the shape memory effect. The phase changes can be produced either by thermal action or by mechanical action that enable SMAs to present two unique properties like superelasticity and shape memory effect. During cooling into low temperature all of the SMAs transform from austenite phase to martensite phase transformation due to the stress accommodation and volume preservation by twinning mechanism shown in Fig. 1.5.

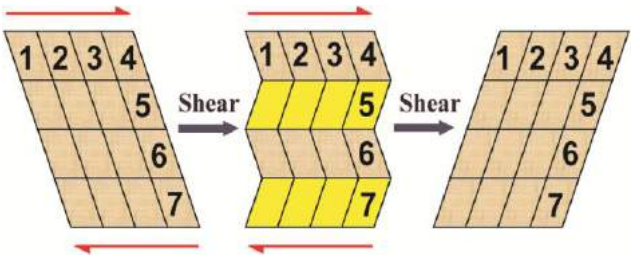

Figure 1.5: Arrangements of the variants after twinning.

In the twinning process, deformation takes place when all of the atoms are martensitically transformed from one place to other place. The crystal in martensitic phase has lower symmetry and is thus degenerate, which results in a certain number of structures which are energetically equivalent but with different crystallographic orientations; these are

called variants. These martensitic variants can exist either as a twinned martensite, which is formed by a combination of self-accommodated martensitic variants to minimize the elastic energy, or as a detwinned or reoriented martensite in which a specific variant is dominant. Fig. 1.6 (a) show microscopic diagram of shape memory effect in a SMA. This deformation occurs temporarily and starts to disappear as long as the material is heated to attain the higher symmetry phase. When the original shape of the material (pre-deformed shape) is restored twins become extinct from the whole system.

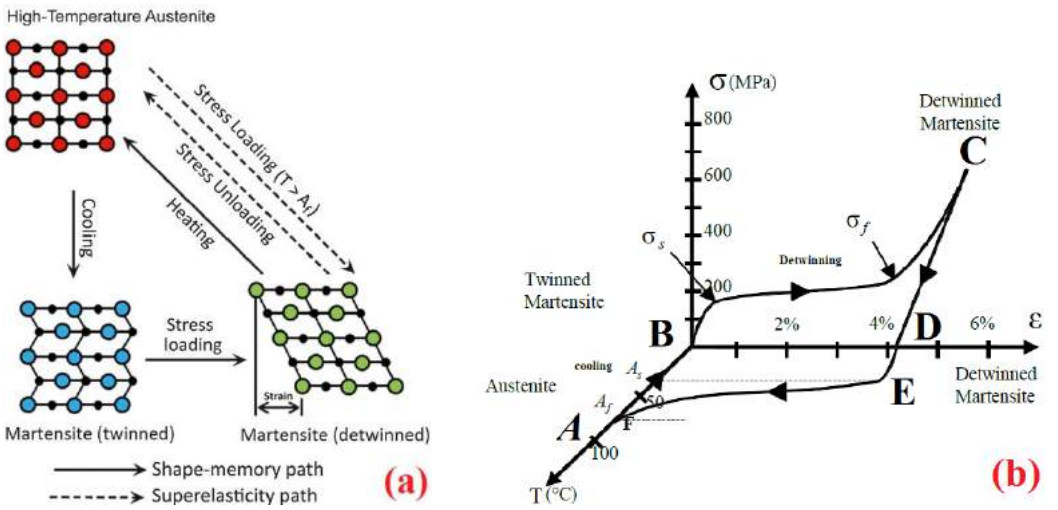

Figure 1.6: Schematic illustration of the deformation In a NiTi SMA (a) mechanism of the shape-memory effect and superelasticity. (b) Stress–strain-temperature curve showing superelasticity. Image source Ref. [33-36]

Hence, SMAs can exist in two different phases, with three different crystal structures (i.e. twinned martensite, detwinned martensite and austenite) and six possible transformations during cooling and heating. Detwinning can be induced by applying stress too. The schematic of stress loading with temperature has been shown in the Fig. 1.6 (a, b). The minimum stress required for detwinning initiation is termed as the detwinning start stress (σ_S) and at sufficiently high stress which results in complete detwinning of martensite is called the detwinning finish stress (σ_f). The detwinning results in macroscopic shape change. Reheating the material will result in transformation back to parent phase and shape recovery even while the load is still applied. The transformation to martensitic phase can also be induced by applying sufficient external stress at a temperature above A_F. The external stress result in formation of fully detwinned martensite created from austenite and complete shape recovery is observed upon unloading to austenite. This effect is known as superelasticity.

1.3.2. Magnetic shape memory effect:

Ferromagnetic shape memory alloy by itself can recover the deformed shape into the pre-deformed (original) shape when temperature is increased and the shape recovery is controllable either by magnetic field or applied stress or by both. The twin variants in FSMA have preferred directions of magnetization below the Curie temperature [9, 10]. The interface between two different variants in these martensites shown in Fig. 1.7 (a) are called twin-boundaries, and show very unique properties. When the applied magnetic field provides the magnetic anisotropic energy less than the energy required to move a twin boundary then magnetization within each variant changes and no shape change is observed as shown in the Fig. 1.7 (b). However if the magnetic anisotropy is high and the energy required to move twin boundaries is low enough, there will be a rotation of the structural domains in such a way that their easy axes get aligned along the externally applied field. In this case, the rotation of martensitic variants is promoted by the difference in the Zeeman energies between the variants, and thus results in a significant macroscopic shape change as shown in the Fig. 1.7 (b) and shape can be recovered once the field is removed [37–39].

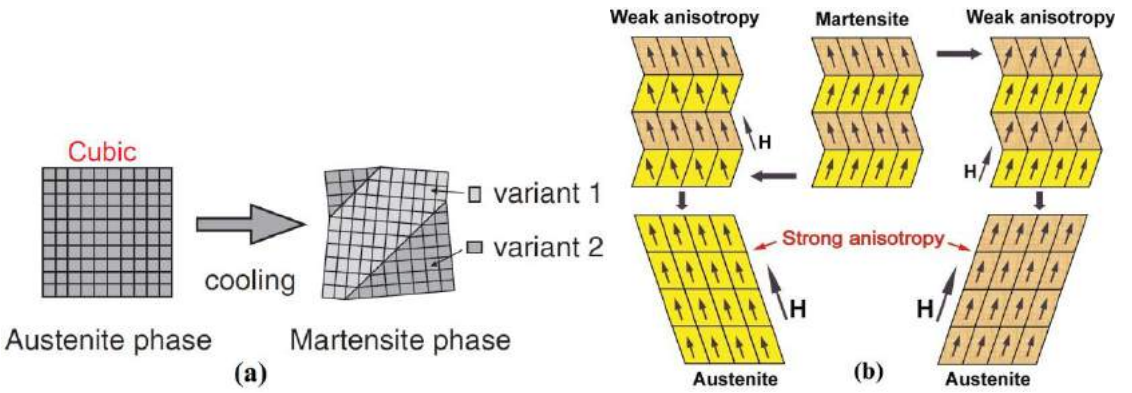

Figure 1.7: (a) Two regions with different orientations (variants) in martensitic phase (b) Rearrangement of the martensite variants in the magnetic field (H) when magnetocrystalline anisotropy is weak and when it is strong.

In any FSMA twin boundaries require a very low stress to move and when they move one variant grows in volume fraction of the crystal at the expense of the other. A compressive stress along the actuation direction favors the variants with short axis parallel to the actuation direction resulting into shortening the crystal, shown in Fig. 1.8 (left block). While a magnetic field perpendicular to the actuation direction favors the variants

with the long axis parallel to the actuation direction (or the short direction along the field direction) resulting in an elongation of the crystal, shown in Fig. 1.8 (right block).

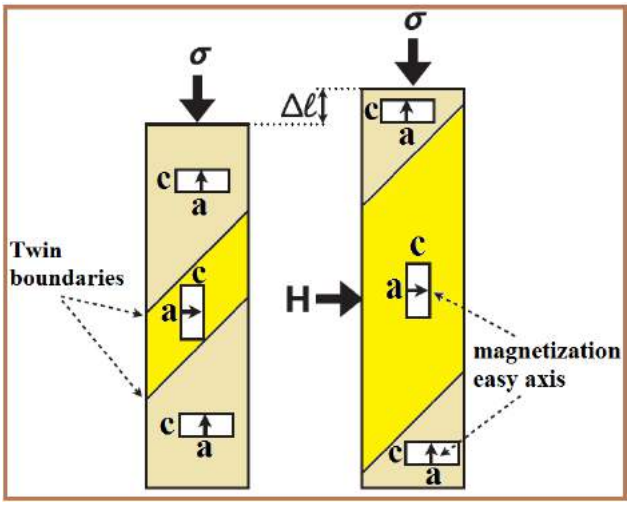

Figure 1.8: Deformation produced by the rearrangement of the variants in the FSMA under an applied magnetic field during dtructural phase transition in FSMA from cubic austenite to tetragonal martensite

In many case the threshold field for twin motion is in the order of 200 mT. When controlled amount of magnetic field and stress are applied in any FSMA in an alternatively cycle process the alloy can actuate.

1.4. Phase transition in Co-Ni-Al FSMA:

Co-Ni-Al ternary alloy has the structure of the alloy with duel phases (γ phase + β phase) in its austenite state [38-41]. The microstructure of the β phase (B2 body-centered cubic structure) is the only main FSMA phase that takes part in structural transition and is brittle, but the presence of the γ phase (A1 disordered face-centered cubic structure) can greatly improve ductility of the alloy. β phase is the austenitic phase that is a higher temperature phase compared to martensitic phase. The arrangements of constituent atomic species in Co-Ni-Al alloy for different phases (β, β' and γ) are shown in Fig. 1.9. (a) as reported earlier [42]. As NiAl- β phase with B2 structure martensitically is transformed into β' phase with $L1_0$ structure. The secondary phase γ or γ' or both present along with β does not show any phase transition during austenitic to martensitic or martensitic to austenitic transition except improving the sample strength. The difference between γ and γ' is that γ phase has Al type disordered face centered cubic structure while γ' phase has ordered $L1_2$ structure of Ni_3Al [43]. γ' phase may be grown in the Co-Ni-Al alloys annealed at comparatively lower temperature. From the earlier reports it is found that in Co-Ni-Al alloy

the Curie temperature T_C, the martensitic transformation starting temperature M_S and the austenitic finishing temperature A_f varies as a function of Co content. T_C increases and M_S decreases with an increase in Co content and the T_C and M_S curves cross at around 35% Co [42].

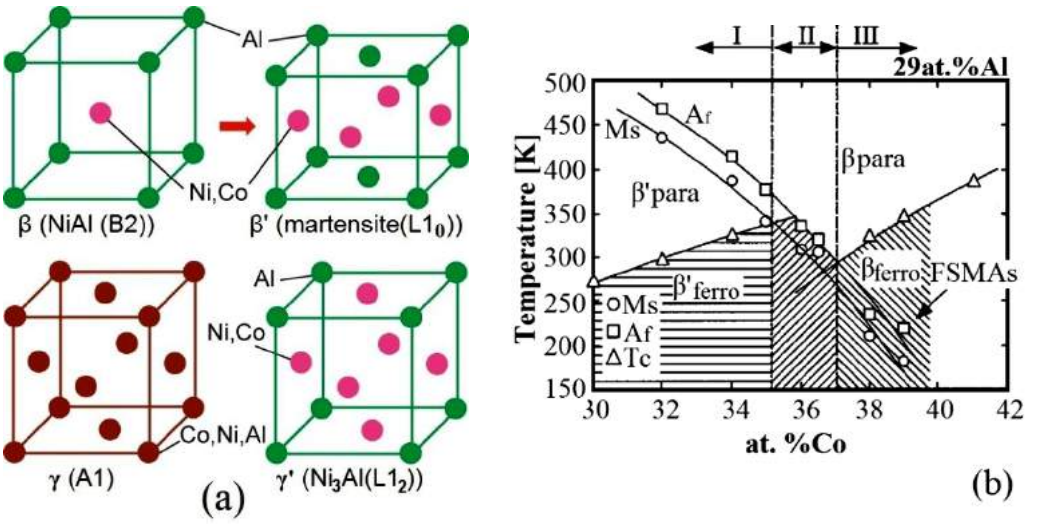

Figure 1.9: (a) Different phases present in Co-Ni-Al alloy under certain conditions (b) Composition dependence of the Curie temperature Tc, the martensitic transformation temperature Ms and the austenitic finishing temperature A_f in $Co_xNi_{(71-x)}Al_{29}$ Image source Ref. [42, 43]

The increase in T_C with the increase of Co content implies that β-phase alloys in the Co-rich portion of the Co-Al binary system are ferromagnetic., with high T_C. From the extrapolated curve of T_C shown in Fig. 1.9 (b) it is found that T_C for the martensite β' phase is about 85K higher than that in Austenitic phase (β) at the same composition. In Fig. 1.10 it is shown that T_C increases with an increase in the Co content and a decrease in the Al content, while Ms decreases with an increase in both the Co and Al contents.

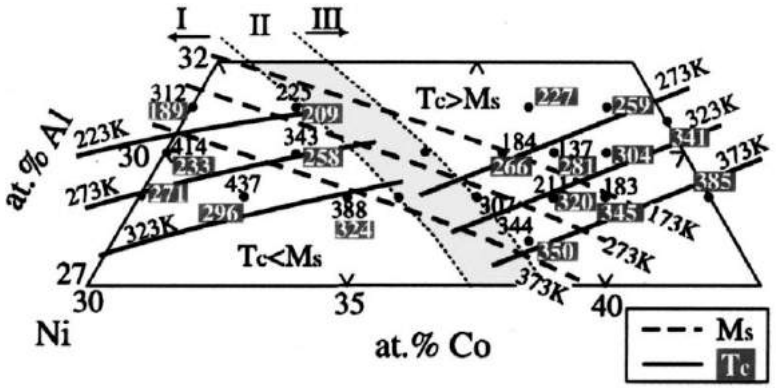

Figure 1.10: Composition dependence of the Curie temperature T_C and the martensitic transformation temperature Ms in the Ni–Co–Al ternary system. Image source Ref. [42]

The total phase transitions are grouped into three types as shown in Fig. 1.9 (b). Case I, paramagnetic β phase, martensitically transforms into paramagnetic β', and eventually transforms into the ferromagnetic β' upon cooling. Case II, paramagnetic β phase, martensitically transforms into ferromagnetic β' upon cooling. Case III, paramagnetic β phase, transforms into ferromagnetic β phase, and then martensitically transforms into ferromagnetic β' phase upon cooling.

Beside the compositional effect in Co-Ni-Al alloys, martensitic temperature Ms is influenced to increase with the elevated annealing temperature of this alloy [38]. Mechanical strength of the Co-Ni-Al is also increased by heat treatment as fraction of γ increased among the binary phases $(\gamma + \beta)$ present in such alloy.

1.5. Finemet alloy:

FINEMET® is the name derived from "Fine" and "metal" which indicates the materials features of being formed with fine crystal grains and having excellent magnetic properties. It was first discovered by Yoshizawa et al [44] in 1988 and has become a tremendously important system for electrical industry, is a Fe-based alloy having ultrasoft magnetic properties. It was a metglass having a composition $Fe_{73.5}Cu_1Nb_3Si_{13.5}B_9$, and could be crystallized by subsequent annealing above recrystallization temperature, giving a bcc Fe-Si solid solution with the grain sizes of around 10-15 nm embedded in a residual amorphous matrix. In these FINEMET alloys, small Cu-enriched particles have been found in the intergranular regions (Fig. 1.11).

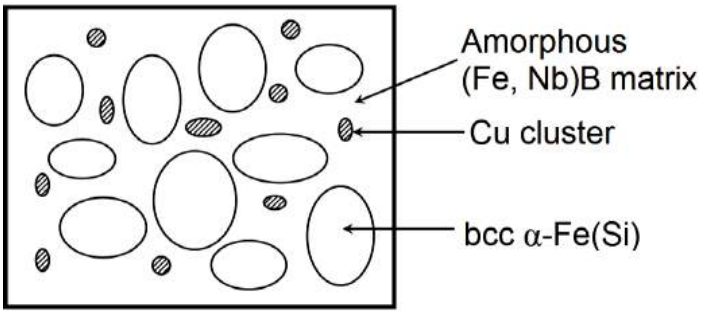

Figure 1.11: Schematic of the microstructure of FINEMET Fe–Cu–Nb–Si–B alloy

This microstructure is the basis of excellent soft magnetic properties due to averaging of the global anisotropy, <K>, related with ferromagnetic exchange length and average grain size and based on Random Anisotropy Model proposed by Herzer [45].

It is noteworthy that the magnetic softness is also due to decrease of magnetoelastic energy, i.e. magnetostriction $(\lambda_s) \longrightarrow 0$ and mechanical stress $\sigma \longrightarrow 0$ due to annealing. This implies that the ribbons in the amorphous state have higher magnetoelastic energy as compared to annealed ones. The additions of small amount of Cu and Nb to the Fe-Si-B are to control reaction kinetics where Cu helps to increase the nucleation rate of bcc Fe-Si phase and Nb hinders the grain growth, resulting in nanocrystalline structure. In addition to Nb as a grain growth inhibitor, other refractory metals such as Ta, Zr, Hf, V, Mo, Cr etc. are also frequently used. The amorphous precursor of this unique material has thickness of around 20-25 μm and width around 5-10 mm. They have high resistivity and high mechanical softness in the amorphous state. Therefore exploiting these exceptional properties, amorphous precursor of this FINEMET alloy may find commercial multifunctional utility like different frequency response, mechanical properties, etc.

The amorphous ribbon is the precursor material of Finemet®. So industrially this material is prepared in the ribbon form by rapid solidification process. The creation of amorphous ribbon for FINEMET® and a typical FINEMET® core is shown in Fig. 1.12.

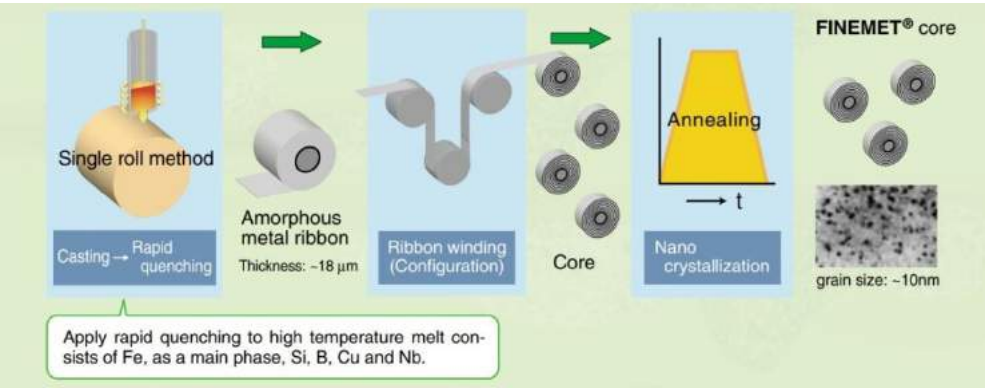

Figure 1.12: Manufacturing process of FINEMET® for commercial use.

Nanocrystallization of FINEMET® ribbon is achieved by annealing amorphous metal follows the crystallization process as amorphous → Cu rich area → the nucleation of bcc Fe from Cu bcc → Fe(-Si). At the final stage of this crystallization process, the grain growth is suppressed by the stabilized remaining amorphous phase at the grain boundaries. As a result nanocrystal grains are embedded in the residual amorphous matrix. The crystallization process is shown in Fig. 1.13.

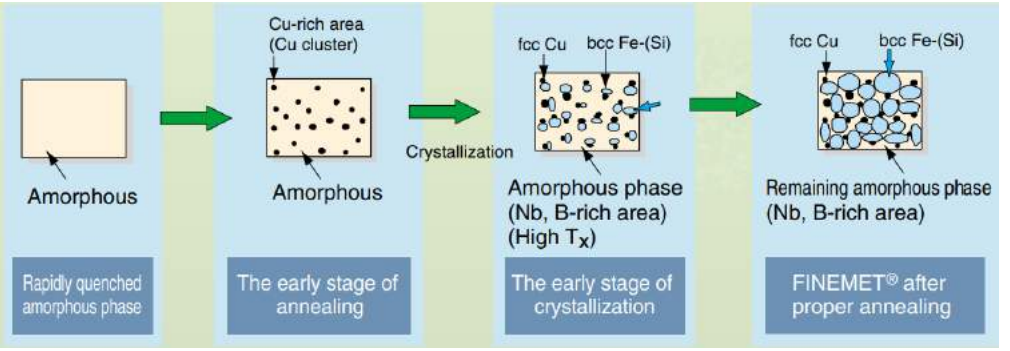

Figure: 1.13: Crystallization process of Finemet® alloys by heat treatment.

The applications of Finemet alloys are enormous. They are used in different conditions to prepare different essential objects. Due to high permeability they are used to make energy saving materials like EMI filters, common mode chokes, magnetic shielding sheets, electromagnetic wave absorbers, current sensors and magnetic sensors. The low core loss property of these alloys enables one to prepare high performance devices like magnetic amplifier, pulse power cores, surge absorbers, and high voltage pulse transformers. The application of low magnetstriction is useful for high frequency tools like high frequency power transformers, active fielters, smoothing choke coils and accelerator cavity.

1.6. Sound velocity and Internal friction in metallic alloys:

Sound velocity and internal friction are cores of mechanical spectroscopy that have been widely used to study the structural defects and their mobilities, transport phenomena and phase transformation in magnetic alloys, magnetoelastic changes in the FM phases. It is a non destructive method (NDT), that is greatly used to analyze the metallic alloys and their physical properties during phase transition. Dynamic elastic modulus, magneto elastic coupling, magneto mechanical damping and ferromagnetic shape memory effect are the mostly explained features of any kind of magnetic metals exploiting this NDT method.

1.6.1. Sound velocity:

Propagation of sound wave through any solid generates the mechanical loading and can be explained as a sum of elastic and anelastic deformation. So that the total strain increment is written as,

$$d\varepsilon = d\varepsilon_{elastic} + d\varepsilon_{anelastic} \quad [1.1]$$

Therefore, sound velocity represents the dynamic elastic modulus resulting lossless elastic strain in term of elastic modulus as

$$v_{solid} = \sqrt{\frac{E}{\rho}} \qquad [1.2]$$

where, E = appropriate elastic modulus (viz. Young's. Shear etc.)

Measurement of sound velocity gives a direct representation of elastic modulus as a function of temperature, magnetic field, etc. showing how the bonds behave as a function of external perturbation. During phase transition, sound velocity in a magnetic alloy gives temperature dependent damping and behaviour change. Focussing on the analysis of relative change of sound velocity $\left(\frac{\delta V}{V}\right)$, i.e. the real part of E, there are two different regions for elasticity that are before and after the transition starts and end. Therefore, assuming a Debye type model [46, 47] where the internal energy, U, can be written at low temperature as a series expansion:

$$U = U_0 + ET^2 + LT^4 \qquad [1.3]$$

Where, E and L are electronic and lattice contributions; the corresponding elastic moduli are then (ε is the elastic strain),

$$B = (d^2E/\, d\varepsilon^2) \quad \text{and} \quad \mathrm{C} = (\mathrm{d}^2\mathrm{L}/\, d\varepsilon^2) \qquad [1.4]$$

And the sound velocity is written as

$$\frac{\delta v}{v} = A + BT^2 + CT^4 \qquad [1.5]$$

Where A, B and C are the coefficients of each contribution as described above. Equation [1.5] is known to hold true for many metallic alloys. Strictly, it should be valid for $T \ll \theta_D$, but generally found to be useful till 300 K for alloys. A simplified model is due to Varshni, where Einstein model is used. For the background estimation, apart from the power law as suggested by Varshni and found to be valid for metals and alloys (both single and polycrystals) and the relation is as,

$$v(T) = v(0) - \frac{S}{e^{\frac{t}{T}} - 1} \qquad [1.6]$$

The relation is based on Einstein oscillator model of solids. Here, *t* is some characteristic temperature of the model and *s/t* is the high temperature ($T \gg t$) derivative dv/dT and $v(0)$ is the zero temperature sound velocity. Points down to $\approx 125K$ are used here to evaluate $(\delta v/v)_L$ down to 115K. The general form of the equation [8] we used for fitting the $\delta v/v$ as,

$$\frac{\delta v}{v} = A - \frac{B}{e^{\frac{C}{T}} - 1} \qquad [1.7]$$

Where A is the value of $\frac{\delta v}{v}$ at some reference temperature. B and C are the constants discussed in equation 1.6, evaluated from the fitting curve.

1.6.2. Internal Friction:

Internal friction is the dissipation of mechanical energy inside a gaseous, liquid or solid medium and contains unique microscopic information that cannot be obtained by other methods. It is the energy dissipation in any solid as manifested by stress–strain hysteresis loss during cyclic loading within elastic deformation range and is expressed as

$$Q^{-1} = \frac{\Delta W}{2\pi W} = \frac{\Psi}{2\pi} \qquad [1.8]$$

Where ΔW is the energy absorption in one cycle and W is the maximum elastic stored energy during that cycle. Ψ is the specific damping capacity and for most metallic materials this hysteresis is rather small, i.e., Ψ << 1 and Q^{-1} is stress dependent.

Anelastic relaxation, as the main source of internal friction is seen in Fig. 1.14 (a) (viscoelastic behaviour) both as a saturating "creep" strain ε(t) after loading, with "unrelaxed" and "relaxed" values ε_U and ε_R, and as a decaying "elastic after-effect" after unloading, and may also be observed as stress relaxation in case of a constant applied strain. It is characterised by a relaxation strength

$$\Delta = \frac{\varepsilon_R - \varepsilon_U}{\varepsilon_U} \qquad [1.9]$$

Using a time-dependent modulus E(t) defined for stress relaxation (generalised Hooke's law) and by a distribution of relaxation times τ relaxation strength can be written as

$$\Delta = \frac{E_U - E_R}{E_R} \qquad [1.10]$$

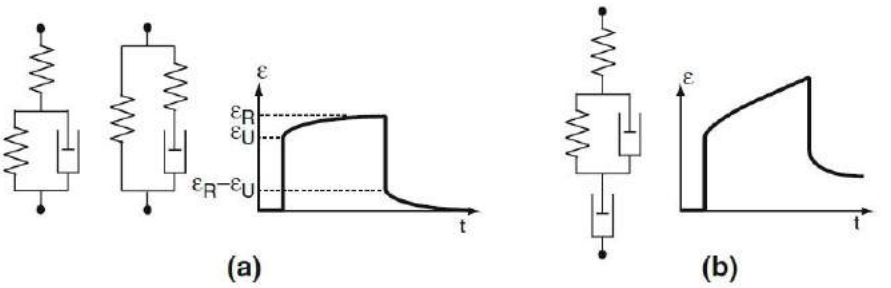

Figure 1.14: (a) completely recoverable three-parameter models ("standard anelastic solid") and (b) partially recoverable four-parameter model. Image source Ref. [48]

This model is the presentation of viscoelastic behaviour by which mechanical energy can be dissipated in a solid. During loading and unloading, the creep strain $\varepsilon(t)$ may result into relaxed strain (ε_R) or unrelaxed strain (ε_U) and the gap between relaxed and unrelaxed strain $(\varepsilon_R - \varepsilon_U)$ can be termed as the elastic deformation. In an anelastic solid defined by the two equivalent three-parameter models in Fig. 1.14 (a), the time dependent changes are of the form $e^{-t/\tau}$ with a single relaxation time τ (either τ_σ for constant stress or τ_ε for constant strain, with $\tau_\sigma = \tau_\varepsilon = \tau$ (for $\Delta << 1$).

In the linear theory of anelasticity [49], using the mathematically convenient complex notation (with complex quantities marked by an asterisk) for sinusoidally varying stress and strain,

$$\sigma^* = \sigma_o e^{i\omega t} \text{ and } \varepsilon^* = \varepsilon_o e^{i(\omega t - \phi)} = (\varepsilon' - i\,\varepsilon'')e^{i\omega t} \qquad [1.11]$$

Under a cycle of applied stress or strain, dynamic responses become as a function of circular frequency ω creating a phase lag "ϕ" between stress and strain. Hence a complex modulus is expressed using linear theory of anelasticity [49] as

$$E^*(\omega) = E(\omega)e^{i\phi(\omega)} = E'(\omega) + iE''(\omega) \qquad [1.12]$$

Where the quantities $E(\omega)$, $E'(\omega)$ and $E''(\omega)$ are called absolute dynamic modulus, storage modulus and loss modulus respectively; the phase lag "ϕ" between stress and strain is denoted as the loss angle and sometimes it is defined as the internal friction [49]. Hence, the internal friction can be expressed in terms of storage modulus and loss modulus as

$$Q^{-1} = tan\phi = E''/E' \qquad [1.13]$$

The storage modulus ($E^{'}$) and frequency dependent internal friction $Q^{-1}(\omega)$ for a standard anelastic solid are given by the well-known Debye equations [49] as,

$$E^{'}(\omega) = E_R\left(1 + \Delta\frac{\omega^2\tau_\varepsilon^2}{1+\omega^2\tau_\varepsilon^2}\right) = E_U\left(\left(1 - \frac{\Delta}{1+\Delta}\right)\left(\frac{\omega^2\tau_\varepsilon^2}{1+\omega^2\tau_\varepsilon^2}\right)\right) \qquad [1.14]$$

and $$Q^{-1}(\omega) = \left(\frac{\Delta}{\sqrt{1+\Delta}}\right)\left(\frac{\omega\sqrt{\tau_\sigma\tau_\varepsilon}}{1+\omega^2\tau_\sigma\tau_\varepsilon}\right) \qquad [1.15]$$

Where E_R and E_U are the modulus for relaxed and unrelaxed strain as in quasi-static considered above. Hence, τ_σ and τ_ε are the relaxation time at constant stress and constant strain respectively for the same case. Δ is the stress relaxation expressed as $\Delta = (E_U - E_R)/E_R$. In case of $\Delta \ll 1$, equations [1.9] and [1.10] simplify to

$$E(\omega) = E^{'}(\omega) = E_R\left(1 + \Delta\frac{\omega^2\tau^2}{1+\omega^2\tau^2}\right) = E_U\left(1 - \frac{\Delta}{1+\omega^2\tau^2}\right) \qquad [1.16]$$

and $$Q^{-1}(\omega) = \Delta\frac{\omega\tau}{1+\omega^2\tau^2} \qquad [1.17]$$

The resulting Debye peak $Q^{-1}(\omega)$, as shown in Fig. 1.15 (a). At $\omega\tau = 1$ the damping is maximum. Losses are detectable only in a certain range around $\omega\tau = 1$ (dynamic hysteresis) and for $\omega\tau \to 0$ and $\omega\tau \to \infty$ the loss angle ϕ vanishes. Fig. 1.15 (b) represents the Internal friction as a function of temperature at constant temperature.

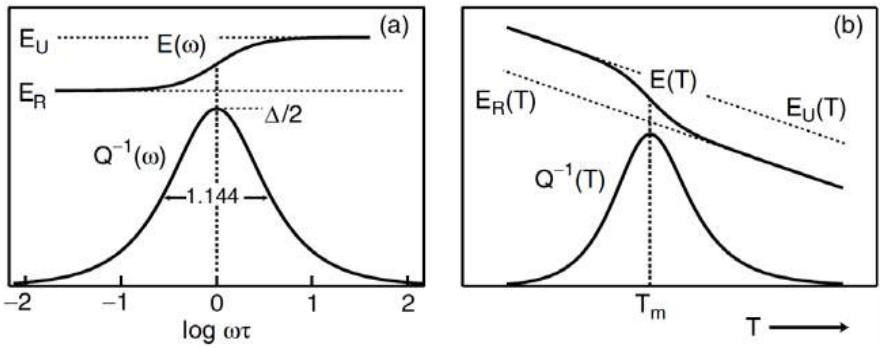

Figure 1.15: Dynamic modulus E and internal friction Q^{-1} of the standard anelastic solid: (a) as a function of frequency on a log ωτ scale and (b) as a function of temperature at constant frequency. Image source Ref. [48].

The relaxation strength Δ and the peak maximum Q_m^{-1} for a polycrystalline material depends on many factors of , such as

a) The orientation of the stress applied to the crystal lattice
b) Dissolved element concentration
c) Temperature
d) Grain size of a polycrystal

In materials in which the two phases connected by the phase transformation can coexist over a certain temperature range, one should consider three separate contributions to the total internal friction [50] illustrated in Fig. 1.16

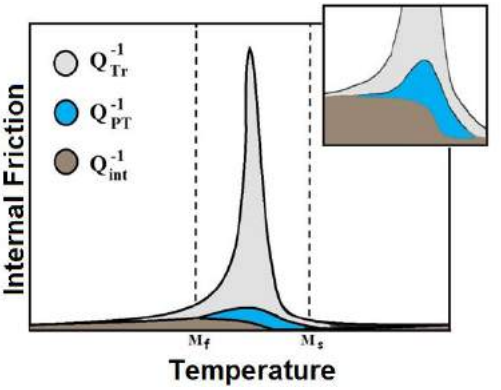

Figure 1.16: Scheme of the three contributions to IF during a martensitic phase transformation: the transitory term Q_{Tr}^{-1} , the phase transition (or isothermal) term Q_{PT}^{-1} and the intrinsic term Q_{int}^{-1}. Image source Ref. [51].

The total internal friction Q_{tot}^{-1} associated with a phase transformation consists of three components:

$$Q_{tot}^{-1} = Q_{Tr}^{-1} + Q_{PT}^{-1} + Q_{int}^{-1} \qquad [1.18]$$

(Q_{Tr}^{-1}) is the transient part of (Q_{tot}^{-1}) that exists only during cooling and heating $(\dot{T} \neq 0)$. It depends on external parameters like temperature rate $(\dot{T})$, oscillation frequency (ω) and oscillation amplitude. (Q_{Tr}^{-1}) is proportional to the rate of volume fraction transformed. (Q_{PT}^{-1}) is related to mechanisms of the phase transformation (PT), which are independent of the transformation rate, such as in here where there is the movement of parent/martensite and martensite/martensite interfaces. (Q_{PT}^{-1}) exhibits a small peak when the interface mobility is maximum. (Q_{int}^{-1}) is composed of the IF contributions of each phase and is strongly dependent on microstructural properties (interface density, vacancies), especially in the martensitic phase. This factor takes into account as:

$$Q_{int}^{-1} = VQ_{mart}^{-1} + (1 - V)Q_{\beta}^{-1} \qquad [1.19]$$

Q_{mart}^{-1} and Q_{β}^{-1} are the intrinsic damping of the martensite and the β phase, respectively, and V is the volume fraction of the martensite phase.

In any ferromagnetic materials there are enormous changes in both elastic moduli during structural and magnetic transformation. Applying a stress to a ferromagnetic material under applied magnetic field causes a variation of magnetization due to the magneto-elastic coupling (magnetostriction), which results in the reduction of Young's modulus below the purely elastic value found in the magnetically saturated state so-called "ΔE effect" four main mechanisms of magneto-mechanical damping are:

a) Magnetoelastic hysteresis damping (Q_h^{-1})
b) Macroeddy-current damping (Q_a^{-1})
c) Microeddy-current damping (Q_μ^{-1})
d) Damping at magnetic transformations (Q_{PhT}^{-1})

Therefor the total magnetomechanical damping

$$Q_M^{-1}(\varepsilon, f, T) = Q_h^{-1}(\varepsilon, f, T) + Q_a^{-1}(\varepsilon, f, T) + Q_\mu^{-1}(\varepsilon, f, T) + Q_{PhT}^{-1}(\varepsilon, f, T) \qquad [1.20]$$

FSMA follows thermoelastic martensitic transition. Internal friction is originated from several kinds of phase transformations:

a) Polymorphic or martensitic transformation or dissolution of second phases
b) Dislocation motion
c) Magnetostriction in ferromagnets.

In amorphous alloys (metallic glass) the structural and mechanical relaxation are closely connected. Structural relaxation is the time dependent equilibration of the atomic structure of condensed matter after any kind of external perturbation. In the classical range of material science the IF (Q^{-1}) generally increases exponentially with temperature increase in any metallic glass. This is shown in Fig. 1.17.

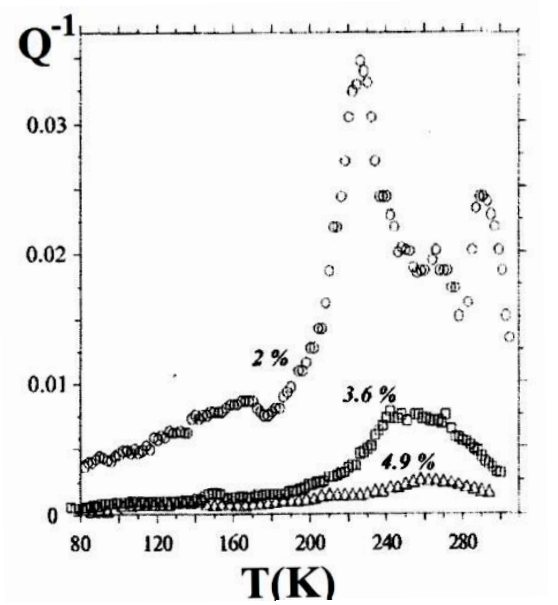

Figure 1.17: Low temperature IF peak in amorphous $Ni_{78}Si_8B_{14}$ after cold rolling at constant strain amplitude (7×10^{-6}) and different rolling degrees. Image source Ref. [48]

The origin of deformation-induced IF lies in local structural changes (i.e., "defects") produced in the shear bonds which carry the highly localised plastic deformatior of metallic glass at low temperature.

1.7. Overview of the thesis:

Magnetic materials due to variety of important technological applications, we focused to investigate the structure and microstructures and different physical that occur in these alloys. Some special properties like dynamic elastic properties, electric resistivity, magnetizability etc of these alloys attracted our attention.

In general, shape memory phenomenon in FSMAs are seen from calorimetry, magnetization and even electrical resistivity measurements at low temperature whereas transmission and scanning electron microscopy, EDAX and X-ray diffraction measurements help us to explore crystal structure and local inhomogeneities in various FSMA and Finemet® alloys with greater accuracy. It is for the first time that low temperature elastic measurements were done on them. Finemet® alloys showed unexpected reversible phase transition at low temperature that is confirmed only from elastic nature at this temperature measurement. Hence in this thesis we focused on the dynamic elastic behavior of FSMAs and FINEMET® alloy systems. The relative change in sound velocity $(\delta v/v)$ and internal friction (Q^{-1}) measurements are main tools to

explain elastic nature [52, 53]. The metallic alloys have been prepared in both the ribbon and reed form.

The primary aspect of this thesis is to explore structural enhancement in magnetic alloys and the magnetoelastic effects on transport properties in disordered alloys. The various novel phenomena described in Sec. 1.7 are explored in various situations. Due to brittleness of most of the FSMAs CoNiAl [42, 43] were proposed as an alternative. The interplay and alteration of β and γ phases of microstructure enhance the mechanical strength of this alloy. These are performed with the heat treatment and by changing the compositions. There should be a maximum limit of increment of γ phase fraction to β phase for the use of proper application as more β decrease ductility with more FSMA properties and more γ increases ductility with less FSMA properties. The increased γ phase fraction also causes increase in disorder and consequently, increased electron scattering, which is also evident from the higher value of resistivity for the alloy annealed at higher temperature. This also may not be desirable. Exploring to low temperature analysis of resistivity (ρ) data, a spin-glass like phase is found below 25K in $Co_{39}Ni_{34}Al_{27}$ annealed at 1373K/24h and post-annealed at 1473K/72h for the first time.

The as-quenched phase of FINEMET metglass with a nominal composition $Fe_{76.5}Cu_1Si_{13.5}B_9$ is partially amorphous as a peak at $2\theta = 44°$ corresponding to the (110) plane of the crystalline bcc-Fe (Si) phase and a broad hump at $82°$ signifying amorphousness of the sample. The thermo-resistivity at low temperature confirms to be entirely metallic during and heating cycle. The only thermal hysteresis found in thermo-elastic nature confirms the phase transition was magnetic in origin. The changes in elastic properties like severely affected electronic part and phononic part in magnetic field of 300 Oe is the evidence of existing strong magnetoelastic coupling in these materials. In parallel, increase in attenuation must be coming from amorphousness of the metglass in low temperature, wherein the fine particles were presumably offering more scattering to the phonons.

The thesis is organized as follows:

I. The basic experimental techniques to prepare the metallic alloys and optimize the physical properties of these alloys are discussed in Chapter-2. In this respect, the descriptions of major instruments used are provided briefly in this chapter. Some

important methods, particularly used to analyze the structural and transported properties of metallic alloys are also prearranged from the related theoretical aspects.

II. Chapter 3 deals with two different compositions of CoNiAl FSMA. Both the samples were characterization by structures and microstructures. We analyzed the phase fractions present inside the samples analyzed from these and the dynamic elastic properties as well as other physical properties affected due to structural anomalies.

III. Chapter 4 describes the effect of heat treatment on CoNiAl FSMA alloys of different compositions. The physical properties in Co-Ni-Al based system and their enhancement due to change in structure and microstructure due to heat treatment are analyzed. The affected mechanical properties are also analyzed in terms of sound velocity (SV) and internal friction (IF).

IV. In chapter 5 we have discussed the stress locking effect in a CoNiAl FSMA. Due to the application of stress for the long time there arises some structural change and the mechanical behavior was also affected. This results to some interesting change in other physical properties also. Hence, we figure out the unexpected results for the same sample here in this chapter.

V. Chapter 6 presents the microstructures in metglass materials. This chapter discusses about the partially amorphous structure in Finemet® alloys that are used as metglass materials. Effects of addition Cr and Nb on microstructure in Finemet alloys are also presented in this section. The existence of a phase transition at low temperature found by SV and IF in Finemet alloys and presented in this chapter. The effect of addition of Cr to the magnetization and phase transitions are also described in this chapter.

VI. Chapter 7 is the conclusion of this thesis and the future scopes are discussed in it.

Chapter 2

Experimental methods

Basic experimental techniques to prepare metallic alloys in the form of ribbon and ribbon and to measure different physical properties have been described in this chapter. Generally X-Ray Diffraction (XRD), Atomic force microscopy (AFM), Scanning Electron Microscopy and Energy Dispersive Spectroscopy (SEM and EDS) etc are used to analyze the structural parameters of the prepared samples. Additionally magnetic susceptibility, resistivity, calorimetry etc. are used to characterize the transition temperatures. Vibrating reed technique has been introduced to this system both in presence of magnetic field or without magnetic field for dynamic elastic behavior as well as magnetoelastic natures. The experimental methods are described in details in this chapter.

2.1. Sample Preparation Technique (FSMA):

It is still a complex and difficult task to prepare a ferromagnetic shape memory alloys with optimum desired properties, Knowledge and control of chemical composition, homogeneity and microstructures are very crucial. As the most of the properties needed for shape memory applications are not intrinsic but extrinsic, preparation of samples has to encounter added complexity. Hence, the homogeneity is the main fact to be kept for fabricating a sample with a ferromagnetic nature as well as shape memory effect. At present the majority of FSMA are made by the convectional melting-quenching [26] method.

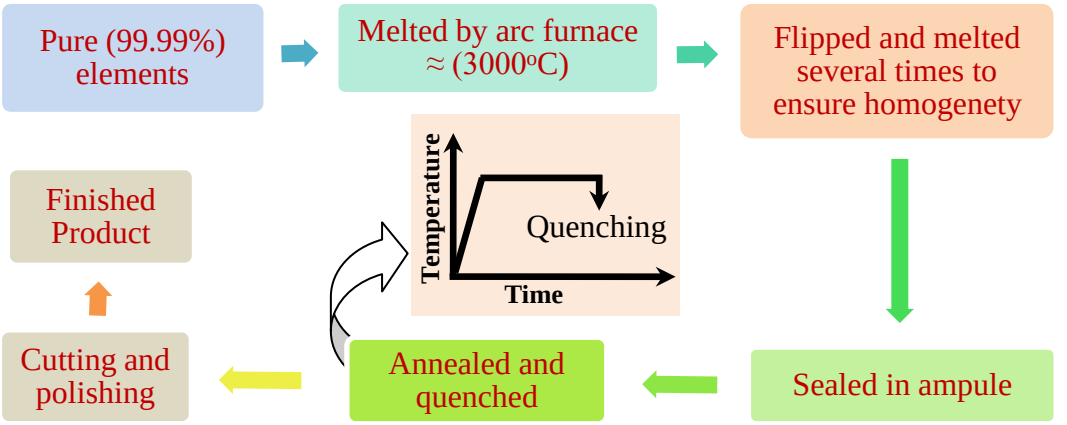

Figure 2.1: Flow chart of a ferromagnetic shape memory alloy preparation route.

2.1.1. Arc melting

Pure (99.99%) Co, Ni, and Al metals were taken at an appropriate weight to make the nominal composition of Co-Ni-Al alloy. The raw materials were kept in the water cooled Cu hearth and melted in an arc furnace with three electrodes, under flowing Ar. The cooled button was flipped in situ, and remelted. This process was repeated three times, so as to achieve chemical homogeneity of the melt. Another check was to measure the weight loss, that is the difference between total input weight and that of the finished button. It was accepted only if the weight loss was less then 2%. The tri-arc furnace we used for sample preparation is shown in Fig. 2.2 (a) and to evacuate the chamber the vacuum pump shown in Fig. 2.2 (b) was used. A diffusion pump was also attached with that vacuum pump. Proper Ar atmosphere inside the chamber was done by repeating evacuation and Ar flashing by turns for 3 times and then finally continuous flowed Ar in.

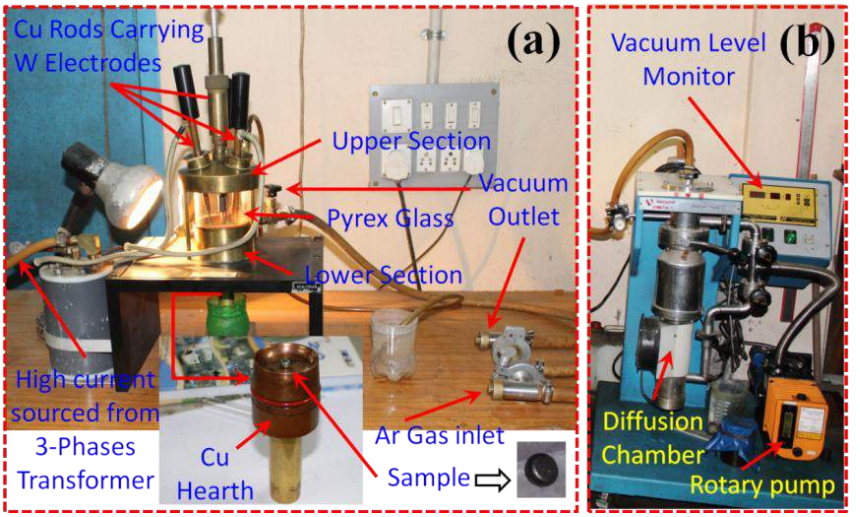

Figure 2.2: (a) A tri-arc furnace used for melting and (b) Vacuum pump to make vacuum of the sample chamber.

2.1.2. Sealing and quenching:

After the arc-melted ingots cooled down to room temperature, they were vacuum sealed in quartz ampules. Before sealing, the quartz tubes were evacuated using the rotary pump and purged with argon gas for 3 – 4 times. A typical vacuum-sealed quartz ampule containing a sample ingot is shown in Fig. 2.3.

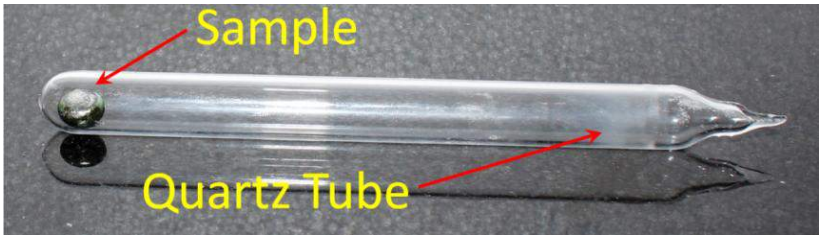

Figure 2.3: A typical vacuum sealed quartz ampule containing arc-melted sample ingot used for annealing.

The quartz ampules containing the ingots were then placed inside a high temperature furnace for annealing. A box type programmable furnace shown in Fig. 2.4, KSL1700X was used for annealing purposes. The box type furnace has $MoSi_2$ heating elements and the system could reach temperature up to 1600 °C. The furnace have programmable temperature controllers for controlling the annealing time as well as heating and cooling rates. After annealing the quartz ampule containing sample ingots were quenched into ice cooled water. The details of this along with the annealing temperature and the duration of the samples are given in the respective chapters.

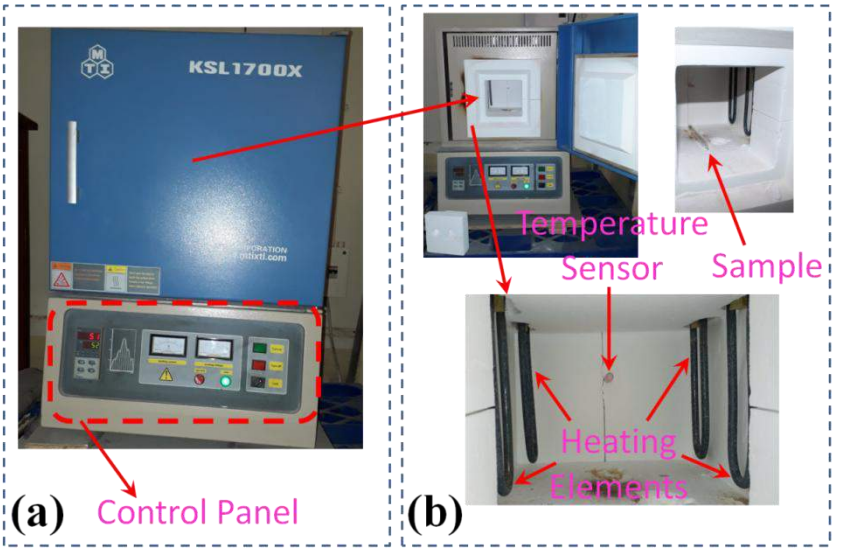

Figure 2.4: A high temperature (1600°C) furnace used for annealing of the samples: (a) outside view (b) inner part of the furnace with sample placing.

2.1.3. Cutting and polishing:

Next step was to cut the arc melt sample into several parts which was done in the isomet diamond cutter which took approximately 5 to 6 hrs under constant 3 rpm and load. It was necessary to use coolant while cutting the samples, because the diamond cutter could create inhomogeneous surface or stress induced surface due to friction on the surface. We used Isomet^{TM} cutting oil for the cutting purpose. Fig. 2.5 (a) is showing the cutting machine we used for our sample preparation and Fig. 2.5 (b) is the prepared sample for resistivity and sound velocity measurement. We cut the drop shaped as-prepared bulk alloy into several pieces of rectangular shape. The screw gauge of the cutting machine was of great use for getting the sample of desirable thickness.

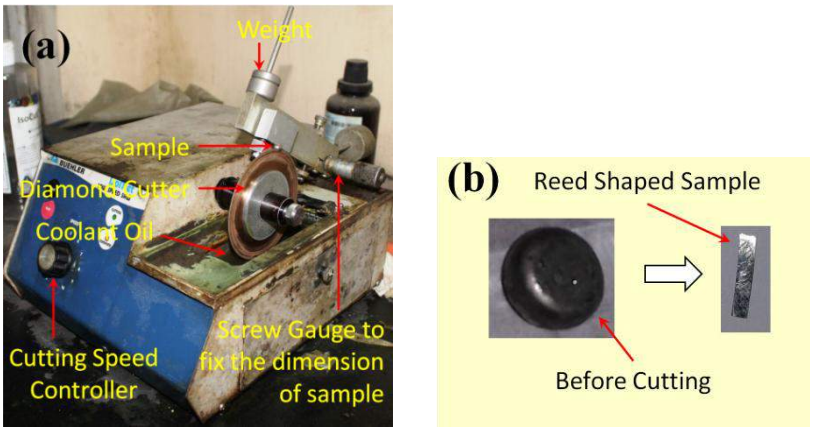

Figure 2.5: (a) Isomet Diamond Cutter (b) Sample prepared for measuring SV & ρ

To make the surface smooth the rough sides of the tablet of each sample were first rubbed with 320, 600, 800 and 1200 grade emery paper respectively. EXTEC ® Labpol 8-12 Convertible Polishing Machine shown in Fig. 2.6 was then used to avoid any unwanted dust or impure particles from the surfaces of each sample. A velvet polishing cloth with synthetic Rayon fibers bonded to a woven cotton cloth was mounted on the lapping wheel. Sample was placed on this cloth as shown in Fig. 2.6 (b) and finer polishing was done using fine chromium oxide powder (Cr_2O_3<1µm) dispersed in a liquid.

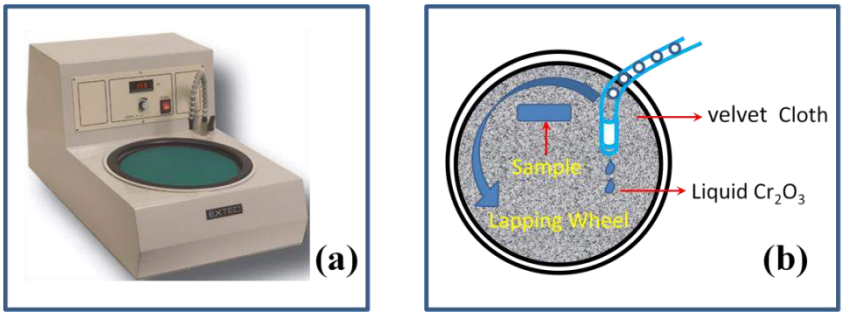

Figure 2.6: (a) Polishing machine with controlled rotation (b) lapping polishing by chromium powder and water.

After polishing, the samples were cleaned using ultrasonic cleaner and dried in air. The ultrasonic cleaner cleans the sample by vibration. The sample was put in a glass vessel of acetone and the vessel with the sample was placed into the ultrasonic cleaner for 5 minutes.

2.1.4. Sample Preparation Technique (FINEMET®):

We prepared FINEMET$^{(R)}$ alloys with nominal compositions of $Fe_{76.5}Cu_1Si_{13.5}B_9$, $Fe_{75.5}Cu_1Nb_1Si_{13.5}B_9$ and $Fe_{56}Cr_{17.5}Cu_1Nb_3Si_{13.5}B_9$ in the form of ribbon shaped amorphous metals. The preparation involved two steps as,

(i) Casting the ingot, which contained all the desired elements of the multicomponent system.
(ii) The remelting and immediate rapid cooling.

The first step, casting the ingot involved vacuum arc remelting to attain homogenous distribution of the alloying components. Hence, at the beginning we have chosen the raw materials with appropriate weight to prepare the nominal compositions. The purity and origin of the constituent elements were Fe (99.98%), Cu (99%), B (99.5%), Si (99.9%), Nb (99.8%) and Cr (99.99%) as obtained from Johnson Mathey (Alfa Aesar Inc.). The

required amounts of constituent elements were taken from pure metal bars or flakes weighed carefully with a sensitive electronic balance. Then alloy balls of these compositions were prepared in an arc furnace on a water-cooled copper hearth under an atmosphere of pure Ar as discussed in 2.1.1. For casting the ingot a melt spinning furnace was used. The melt spinning furnace has mainly two parts: a quartz tube with induction coil arrangement and a copper wheel for rapid solidification of the molten objects. Fig. 2.7 shows the schematic of a melt spinning furnace.

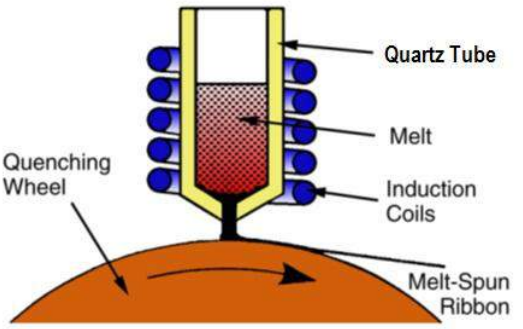

Figure 2.7 (a): A close look at melt-spinning and its schematic. Image source Ref. [54]

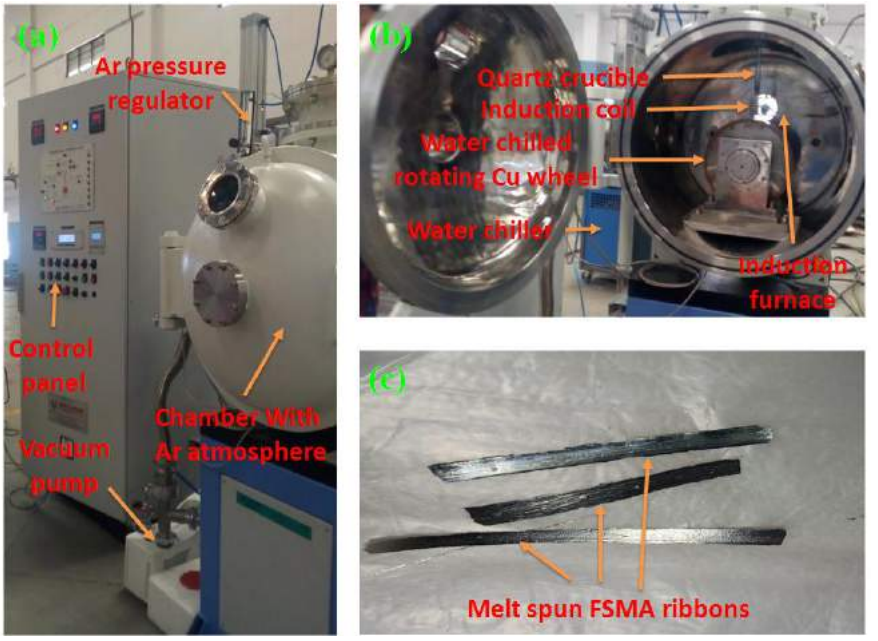

Figure 2.7 (b): RF Induction furnace used for Finemet Sample preparation

The arc melted master alloy was put inside the quartz tube crucible for re-melting in the induction furnace with a maximum power of 25 kW at a nominal frequency of 10 kHz. Hence remelting was done approximately at 1450^{o}C under an argon pressure of 0.5 atm. The quartz crucible has in its bottom part a rectangular nozzle tip of 8 mm length and 0.7 mm width. The position of the nozzle tip can be adjusted with respect to the copper wheel

surface, so that the molten alloy was perpendicularly ejected onto the wheel surface from a distance of about 0.3 mm. The molten metal was ejected with an over pressure of 250 mbar of 99.9% pure Ar supplied from an external reservoir through a nozzle, onto the rotating copper wheel with surface velocity of 30 m/sec. The temperature was monitored by an external pyrometer from the upper surface of the molten alloy through a quartz window. The metal alloys were ejected at a temperature of about 150-250 K above the melting point of the alloy. The resulting ribbon samples had thickness of about 20-22 μm and width of ~6 mm. Processing parameters such as the thermal conductivity of the rotating quench wheel, wheel speed, ejection pressure, thermal history of the melt before ejection, distance between nozzle of quartz tube and rotating wheel, as well as processing atmosphere have marked influence on the microstructure and properties of melt-spun ribbons.

2.2. Microstructure and compositional analysis:

2.2.1. Field Emission Scanning Electron Microscopy (FESEM):

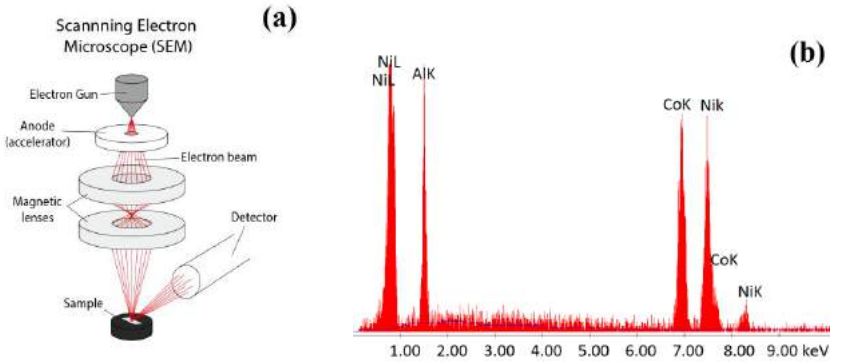

Figure 2.8: (a) Schematic of Scanning Electron Microscope (SEM) (b) EDAX measurement performed on a FSMA of Co-Ni-Al system

The Field Emission Scanning Electron Microscope (FESEM) is a non-destructive analytical technique and is widely used to probe the chemical composition of the metallic samples. The schematic of a scanning electron microscope is shown in Fig. 2.8 (a). It works by using a beam of electrons emanating from an electron gun in vacuum and is accelerated by a high potential difference and collimated. The electron beam has an energy ranging from 0.2 keV to 40 keV and operational accelerating voltage 200V-30KV. The beam is focused onto sample with the help of electrostatic field. Sufficiently high energy electrons interact with an innermost K- level electron of an atom in the material, ejecting it form the

shell and creating a vacancy. Another electron in higher energy level fills this vacancy thereby emitting electromagnetic radiation equal to difference of the two energy levels, which is mostly in region of X-ray [55]. For imaging purpose, secondary and backscattered electrons are commonly used. Each element emits its own characteristic X-ray, thus by measuring the number of X-ray photons and the energy of X-ray by using energy-dispersive X-ray (EDAX) detector placed inside the SEM chamber one can determine composition of sample nondestructively. A typical EDAX curve for a Co-Ni-Al sample is shown in the Fig. 2.8 (b).

2.2.2. Atomic Force Microscopy (AFM):

Surface topography study of the Ribbon samples was carried out by Atomic Force Microscopy (AFM) by quantitative roughness analysis. The AFM consists of a cantilever with a sharp tip (probe) at its end that is used to scan the specimen surface. The cantilever is typically silicon or silicon nitride with a tip radius of curvature on the order of nanometers. When the tip is brought into proximity of a sample surface, forces between the tip and the sample lead to a deflection of the cantilever according to Hooke's law. Depending on the situation, forces that are measured in AFM include mechanical contact force, van der Waals forces, capillary forces, chemical bonding, electrostatic forces, and magnetic forces. Typically, the deflection is measured using a laser spot reflected from the top surface of the cantilever into an array of photodiodes. The AFM can be operated in a number of modes, depending on the application. In general, possible imaging modes are divided into static (also called contact) modes and a variety of dynamic (non-contact or "tapping") modes where the cantilever is vibrated. Fig. 2.9 (a) shows the schematic of a atomic force microscopy and 2.9 (b) shows a 3d topography measured for a CoNiAl ribbon system.

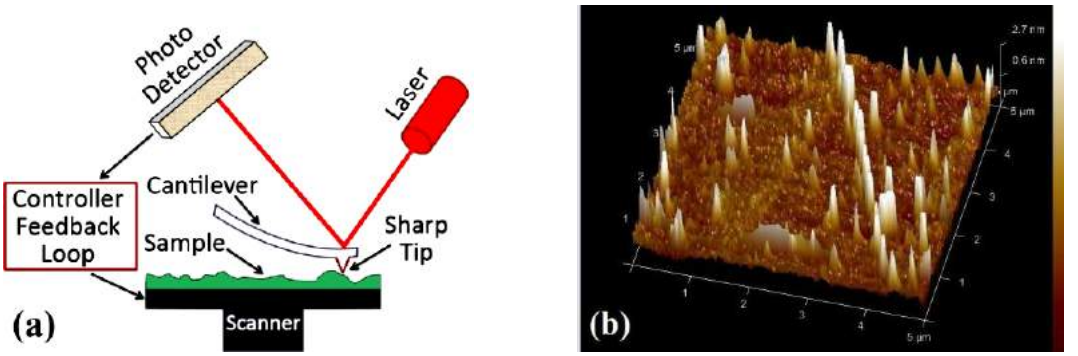

Figure 2.9: (a) working principle of atomic force microscopy (b) 3D topography of a CoNiAl ribbon.

2.3. Structural Characterization

2.3.1. X-ray diffraction:

X-ray diffraction (XRD) is the most used technique for structural characterization and phase identification of polycrystalline materials. All the crystalline materials have a periodic arrangement of lattice points which can be described by the Bravais lattice system. The constituent atoms of a material sit on these lattice points and form regular atomic arrangements that can be described by lattice planes which are generally indicated by Miller indices (*h k l*). When an X-ray beam falls on the material, it gets scattered at the lattice sites by the electrons of the constituent atoms. The scatterings can be both elastic and inelastic in nature. Here in x-ray diffraction, we are concerned only with the elastic scattering so that the incident and scattered waves have the same wavelength and a definite phase relationship among them. Bragg-scattering [56] experiment is used so much in X-ray studies, the regularly spaced atoms in the crystal act like partially reflecting planes, scattering the waves in definite preferred directions (Fig. 2.10). In these preferred directions the waves reflected from adjacent planes differ from each other by exactly one wavelength and being in phase with each other, produce constructive interference.

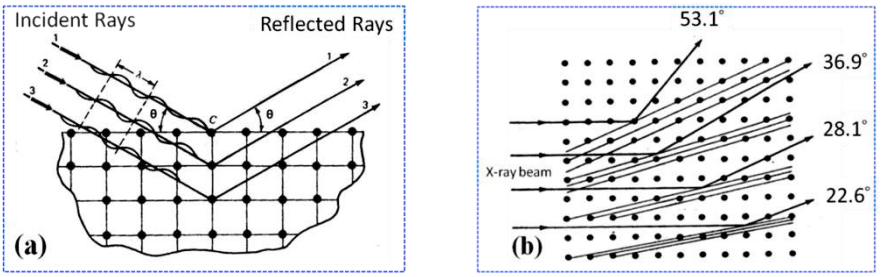

Figure 2.10: (a) Geometry illustrating the Bragg rule of reflection for X-ray from the surface layers of a crystal and (b) Diagram of reflection of X-rays from the various atomic planes in a crystal lattice.

Bragg reflection is a coherent elastic scattering (energy is conserved on reflections) if a beam of monochromatic radiation of wavelength λ incident on a periodic crystal plane at an angle θ is diffracted in the same angle abides by the Bragg's law as,

$$2d_{hkl}sin\theta = n\lambda \qquad [2.1]$$

Where d = separation of planes, θ = angle of diffraction, λ = wavelength of X-rays and n is an integer (Fig. 2.11).

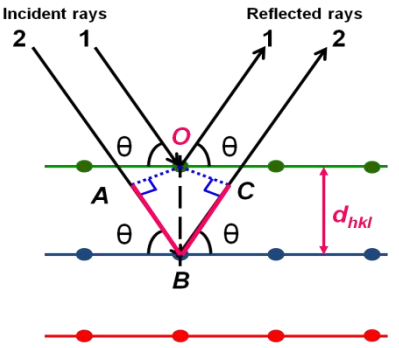

Figure 2.11: Schematic of Bragg's diffraction condition $2d_{hkl}sin\theta = n\lambda$ from a lattice.

The X-Ray diffraction measurements were done using either a PANalytical X'Pert PRO diffractometer with MoKα (wavelength $(\lambda = 0.71\text{Å})$ source or a RIGAKU MiniFlexII diffractometer with Cu Kα $(\lambda = 1.54\text{Å})$. PANalytical^{TM} X'Pert PRO diffractometer the sample stage was fixed while both the source and the detector rotated. However, in the Rigaku MiniFlex^{II} diffractometer the source was fixed while the sample stage and the detector rotated. The reed or ribbon shaped sample was kept in the middle of the sample holder and XRD pattern was obtained with scan rate of 1°/min and step size of 0.02°.

2.3.2. Interpretation of the XRD Data:

The XRD data consisting of θ_{hkl} and d_{hkl} values corresponding to the different crystallographic planes are used to determine the structural information of the samples like lattice parameter and constituent phase. As discussed earlier in the section 1.3 and 1.5 in stable arrangement of half Heusler alloy (XYZ) crystallize in the BCC (B2) structure in austenitic phase for Co-Ni-Al system. In this alloy X and Y atoms are located at the A(0,0,0) and B(¼,¼,¼) Wyckoff positions and the Z atom is located at the D(3/4,3/4,3/4) position respectively. The other phase of non-FSMA γ has the FCC (A1) structure. Hence, the odd/even arrangement of (h,k,l) for this system is found as (100), (111), (110), (200), (210), (220), (211).

The structural parameters was obtained by Reitveld refinement using Fullproof software. Mathematical analysis of Rietveld analysis has been reported earlier [57–60]. Here the weight fraction *W* of phase *p* has been calculated by the equation [61]

$$W_P = \frac{S_P(ZMV)_P}{\sum_i S_i(ZMV)_i} \qquad [2.2]$$

where *S, Z, M* and *V* express the Rietveld scale factor, the number of formula units per unit cell, the mass of the formula unit and the unit-cell volume respectively. The crystallite size was calculated by Debye Scherer formula where line broadening at half the maximum was measured by Gaussian fittings and the formula is as,

$$D_g = \frac{k\lambda}{\beta \cos(\theta)} \qquad [2.3]$$

Where Dg is the grain size and λ is the wave length of Cu-Kα radiation. β is the full width at half maximum (FWHM) measured in radians.

2.4. Transport measurements by differential scanning calorimetry (DSC):

Differential scanning calorimetry (DSC) is a thermo-analytical technique to determine the structural transition in any material. The ability to determine transition temperatures and enthalpies makes DSC a valuable tool in producing phase diagrams for various chemical systems. It is based on the energy absorbed or released by a sample when it is heated or cooled, providing quantitative data on endothermic (heat absorption) and exothermic (heat evolution) processes. When the sample undergoes a 1st order phase transition, greater or less heat will need to flow to it than the reference to maintain both at the same temperature. Whether less or more heat must flow to the sample depends on whether the process is exothermic or endothermic. By measuring the difference in heat flow between the sample and reference, differential scanning calorimeters are able to measure the amount of heat absorbed or released during such transitions. In ferromagnetic shape memory alloy (FSMA) exothermic or endothermic peak is observed during Austenite to Martensite phase transition. Both the sample and reference were maintained at nearly the same temperature throughout the experiment. Generally, the temperature program for a DSC analysis is designed such that the sample holder temperature increases linearly as a function of time. The reference sample should have a well-defined heat capacity over the range of temperatures to be scanned. DSC heat flow signals is given below,

$$\frac{dH}{dt} = C_p \frac{dT}{dt} + f(T,t) \qquad [2.4]$$

where, $C_p = \text{Sample Heat Capacity}$, $f(T,t) = \text{Heat flow rate that is function of time at an absolute temperature (kinetic) and } \frac{dT}{dt} = \text{Heating Rate}$. The DSC measurement for the

present metallic alloy systems were measured using the standard TA instrument of model DSC Q 2000. The schematic diagram is shown in Fig. 2.12

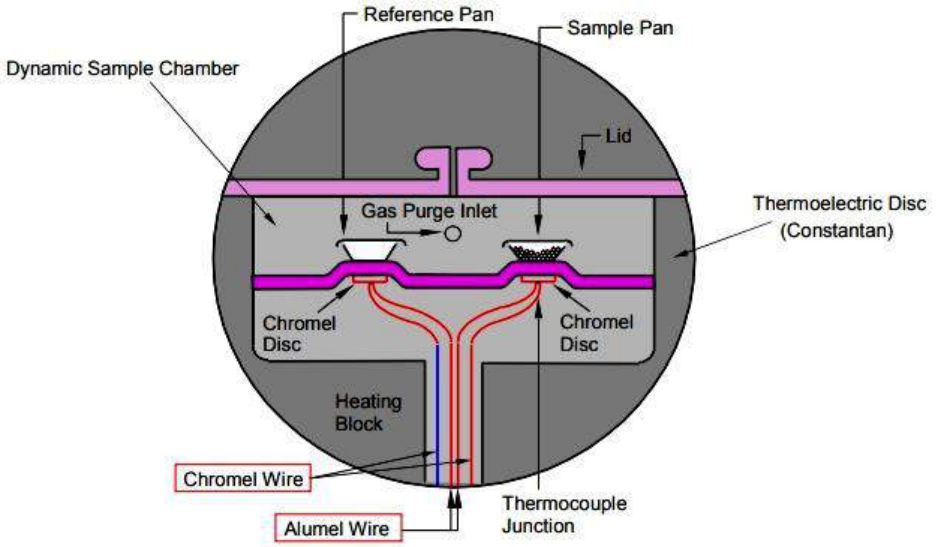

Figure 2.12: Schematic Diagram of DSC measurement process

In a "heat flux" DSC, the sample material, encapsulated in a pan, and an empty reference pan sit on a thermoelectric disk surrounded by a furnace. As the temperature of the furnace is changed (usually by heating at a linear rate), heat is transferred to the sample and reference through the thermoelectric disk. The differential heat flow to the sample and reference is measured by area thermocouples using the thermal equivalent of Ohm's Law.

$$q = \frac{\Delta T}{R} \qquad [2.5]$$

Where $q =$ sample heat flow, $\Delta T =$ temperature difference between sample and reference and $R =$ thermal resistance of the thermoelectric disk.

2.5. Resistivity Measurement:

Resistivity measurement is a good method for structural transition observation [47, 62] in any material. The values and changes in resistivity correspond to the structural changes due to rearrangement of scattering centre. Four probe method is one of the standard and most commonly used method for the accurate measurement of resistivity. It overcomes the problem of contact resistance and also offer several other advantages as four Point arrangement are especially useful for quick measurement. This setup can measure samples of reasonably wide resistivity range (micro ohm to mega ohm).

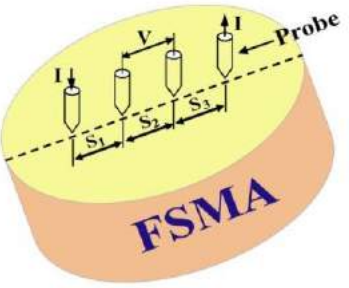

Figure 2.13: Model for the four probe resistivity measurements

We have implemented the four probe method with temperature control unit to measure very low resistances ($\sim m\Omega$) of metallic alloys in this thesis [63]. A schematic of the method of the full setup is shown in Fig. 2.14.

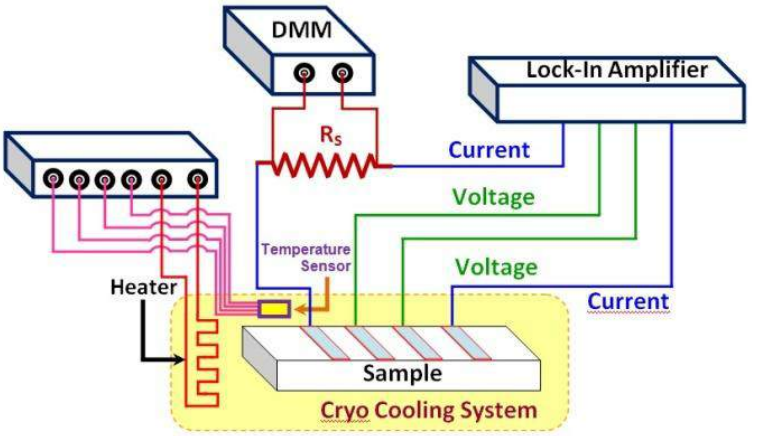

Figure 2.14: Schematic of low temperature resistance measuring system using four probe method where R_S is the standard resistance and DMM refers to digital multimeter.

The probe current was passed through the outer leads, while inner leads were used to sense the voltage drop. As negligible current passed through the voltage leads, lead and contact resistances were avoided in this method. To minimize the effects of thermoelectric effect at the contacts we used ac excitations for which polarity changed according to the frequency of the ac signal and consequently emf generated due to thermoelectric effect got canceled. As the current passing through the sample and the standard resistance is same we can write

$$i = \frac{V_{Sample}}{R_{Sample}} = \frac{V_{Std}}{R_{Std}} \qquad [2.6]$$

where V_{Std} and V_{Sample} are the voltage drops across the standard resistance and the sample respectively, R_{Std} and R_{Sample} are the resistances of the standard resistance and the

sample. Thus by measuring the V_{Sample} , V_{Std} and knowing R_{Std} we can get the sample resistance as

$$R_{Sample} = V_{Sample} \times \frac{R_{Std}}{V_{Std}} \quad [2.7]$$

An ac current $(\sim 1\ to\ 2\ mA)$ at a frequency of 111.11 Hz was sourced from a lock-in amplifier through a standard resistance $(\sim 1K\Omega)$ and the voltage drop across the sense leads was detected also using the lock-in amplifier.

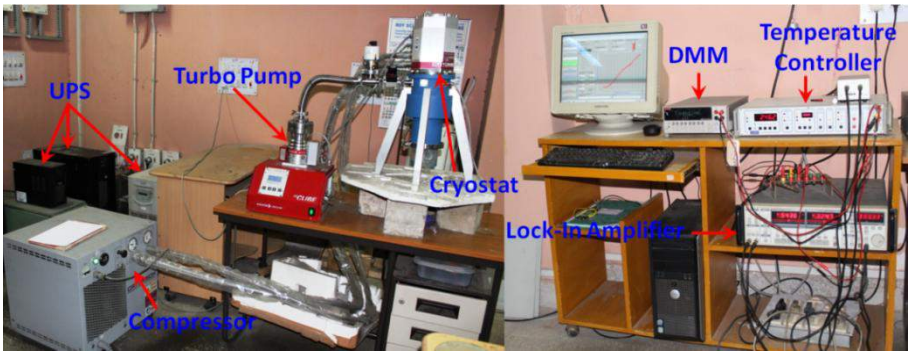

Figure 2.15: The picture of the experimental setup for measuring low temperature resistivity.

A Stanford Research Systems^{TM} 830 (SR830) digital signal processing (DSP) lock-in amplifier was used for the source of ac current and the measurement of the voltage across the sample. The voltage drop across the standard resistance was measured using a Keithly 2000 digital multimeter (DMM) again in four probe configuration. A closed cycle cryostat (CCR) from Oxford Instrument^{TM} (Optistat AC-V®) with pulsed tube refrigerator (PTR) was used to obtain the low temperature environment needed for the measurement of resistivity data at low temperature. In this system resistance could be measured in the temperature range about 5K to 300K. The temperature of the sample was detected using Rh-Fe thermometer mounted on the low temperature stage of the cryostat and the temperature inside the cryostat was controlled by an Oxford Instrument ITC-503 temperature controller. The sample chamber was evacuated using a turbo molecular pump from Pfeiffer Vacuum TechnologyTM AG which provided low pressure environment inside the sample chamber to $\leq 5 \times 10^{-5}$ mbar. The photo of the resistivity set-up is shown in Fig. 2.15. The measurements were performed by slowly heating the sample at a rate 1 K/min. The entire set-up was connected to a computer via GPIB (General Purpose Interface Bus) and controlled by a program developed in LabVIEW^{TM}. The front panel control and block diagram of the software developed for resistivity measurement are shown in Fig. 2.16.

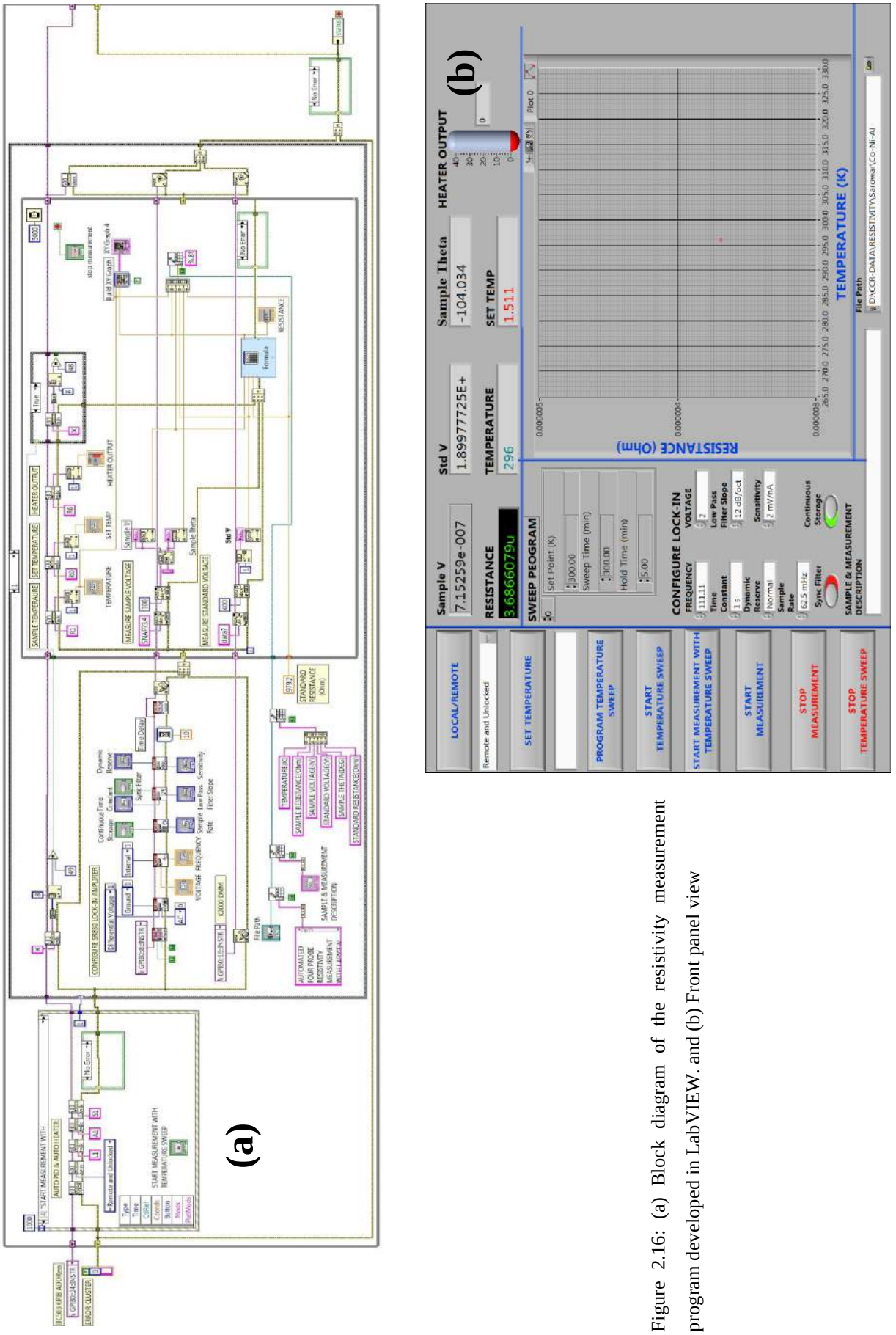

Figure 2.16: (a) Block diagram of the resistivity measurement program developed in LabVIEW. and (b) Front panel view

2.6. Resonance Ultrasound Spectroscopic (RUS) Method:

The elastic modulli of the alloy was studied using Resonance Ultrasound Spectroscopic Method (RUSpec, Quasar International, Albuquerque, NM). It is a nondestructive method of measuring dynamic elastic properties of metallic alloys. The RUS scan frequency ranged between kHz to MHz for any alloys such that the resonant frequencies in the frequency range were obtained. The elastic modulii were calculated from the RUS spectra using inbuilt software (RPModel, Quasar International). The software analyzed the experimental data, starting with initial guess values and calculated the elastic moduli along with an error%. We repeated measuring unless the error% was reduced to minimum value. Fig. 2.17 shows a good simulated data with less error%.

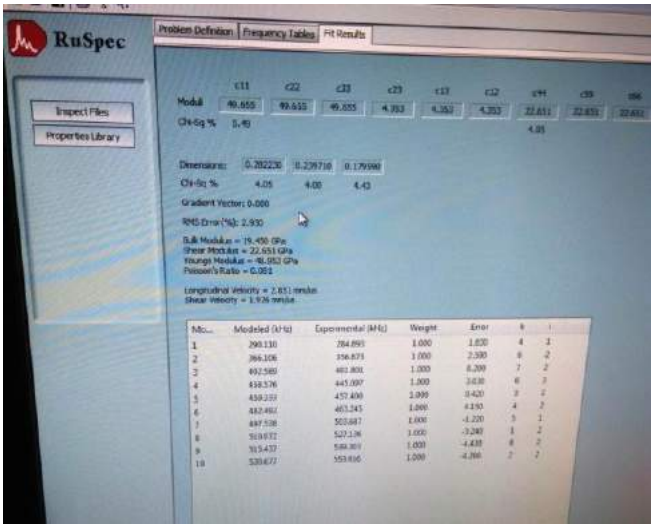

Figure 2.17: Simulation of resonance spectroscopy data and the output data with error (%)

The resonant ultrasonic spectrometer consists of two transceducers. One transceducer is responsible of generating purturbation of different frequencies through the rectangular sample placed while other transceducer act as a receiver of that signal. As the normal mode frequencies of a sample is highly sensitive to its elastic structure [64], RUS is a preferable nondestructive way to study the elastic modulli. The prepared samples were in rectangular parallelepiped shape, about 2.5 mm long, 2.4 mm wide and 1.8mm thickness. In our present work the RUS scan frequency ranged between 200-750kHz for the Co-Ni-Al alloys such that the first 10 resonant frequencies in the lower frequency range were obtained. From these resonance frequencies the homogeneity of the sample and the elastic tensor of the sample have been studied with high degree of accuracy [65].

A schematic of RUS measuring tool is given in Fig. 2.18 where (a) represents the instrumental setup of the RUS method and (b) represents the resonance spectrum of a Co-Ni-Al alloy which was scanned in the range of 200-750kHz.

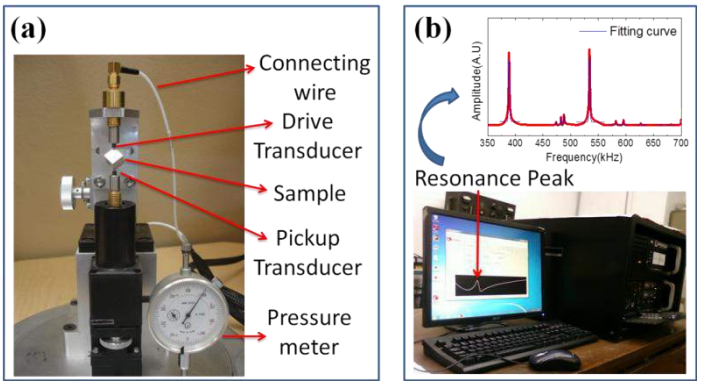

Figure 2.18: (a) RUS setup with rectangular shape of sample (b) Output and computation of the resonance frequencies including Lorentzian fitting

The internal friction Q^{-1} was calculated using the formula:

$$Q^{-1} = \Delta f / f_{res} \qquad [2.8]$$

Where, Δf is the width of resonance curve between the points where the value of amplitude is $\frac{A_{max}}{\sqrt{2}}$ and f_{res} is found at A_{max}. The values of Δf and f_{max} were measured from the Lorentzian fitting of the resonance graph. The average internal friction (Q^{-1}) for the lowest ten measured resonance frequencies [66] was calculated by,

$$Q^{-1} = \frac{1}{10}\sum_{n=1}^{10}\frac{\Delta f}{f_{res}} \qquad [2.9]$$

We measured the Q^{-1} at room temperature and in this setup the temperature was not varied and also no magnetic field was applied.

2.7. Sound velocity and Internal friction Measurements by vibrating reed:

Sound wave propagation through any solid provides information of its elastic property. This measurement gives crucial data for tracking structural changes in the phase transitions and evaluate the magnetoelastic changes in the FM phases. Temperature

dependent anomaly of sound velocity v or its change $\left(\frac{\delta v}{v}\right)$ in any magnetic alloy is used to measure the temperature dependent electronic, lattice and magnetic contributions in it.

The vibrating reed technique is widely used to study elastic moduli and internal friction in solids which are in the form of thin strips [52, 53, 67-70]. The method is particularly suitable for studying metallic glasses and other rapidly quenched alloys which can only be produced as thin foils. In our present work, sound velocity, $\left(\frac{\delta v}{v}\right)$ and internal friction, (Q^{-1}) have been measured using a vibration reed technique (VBR) [52, 53].

2.7.1. Theory of measurement:

The vibrating reed apparatus is based on flexural oscillation of a clamped free bar. The forces are principally those that arise in the bending of a beam. The strains give both elongation and contraction on the opposite sides of the neutral axis and the elastic modulus is concerned is Young's modulus (E). The general wave equation for flexural waves passing along a bar is given by

$$\frac{d^4y}{dt^2} + \left(\frac{\rho_o}{Er^2}\right)\frac{d^2x}{d^2y} = 0 \qquad [2.10]$$

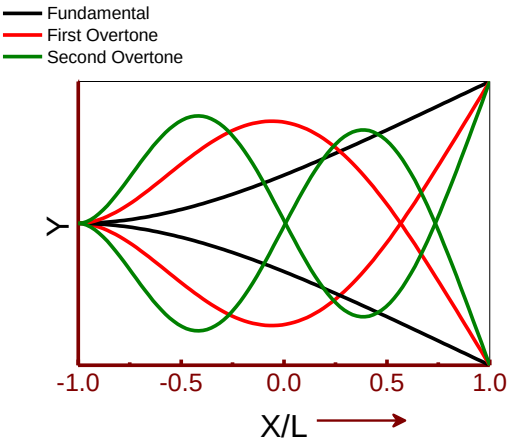

Figure 2.19: Flexural eigen shapes of the fixed-free vibrating reed.

Where, E =Young's modulus
$r = d/\sqrt{12}$ = radius of gyration of the cross-sectional
d = Thickness of the bar
ρ = Density of the material
y = transverse displacement of the bar where the x-axis coincides with the neutral axis.

The phase velocity of this wave is given as

$$v = \frac{\omega}{k} = (\omega v_E r)^2 \qquad [2.11]$$

Where $v_E = \sqrt{E/\rho}$ is the sound velocity in the reed. The eigen frequencies of natural modes are obtained by graphically solving the relation

$$\cosh\left(\frac{\omega L}{v_E}\right) cos\left(\frac{\omega L}{v_E}\right) = -1 \qquad [2.12]$$

Where $\omega = 2\pi f$ and $L =$ length of the reed. The frequencies are expected as

$$f_n = \frac{d}{4\pi\sqrt{3}}\left(\frac{\beta_n}{L^2}\right)^2 v_E \qquad [2.13]$$

Where, d is the thickness of sample and β_n are constants depending on the mode of oscillation (n=1 for fundamental, =2 for the first overtone. etc.) $\beta_1 = 1.875$, $\beta_2 = 4.694$, $\beta_3 = 7.855$ etc. We measured for the fundamental mode only.

The apparatus is based on phase sensitive detection of the resonance by a two-phase lock-in amplifier. The quadrature output of the lock-in amplifier is then used to drive a voltage controlled oscillator (VCO) to achieve automatic frequency locking (AFL). The AFL technique has been used before [71] by utilising a frequency modulation technique. In our case the phase sensitive detection is done by a lock-in amplifier [52, 53]. The AFL allows us to monitor and continuously record the resonance frequency and amplitude of oscillation in computer. The system was easy to assemble and was built by using instruments which were generally available in a research laboratory (like lock-in amplifiers, oscillators, frequency counters. computer, etc). The schematic of the apparatus is shown in Fig. 2.20.

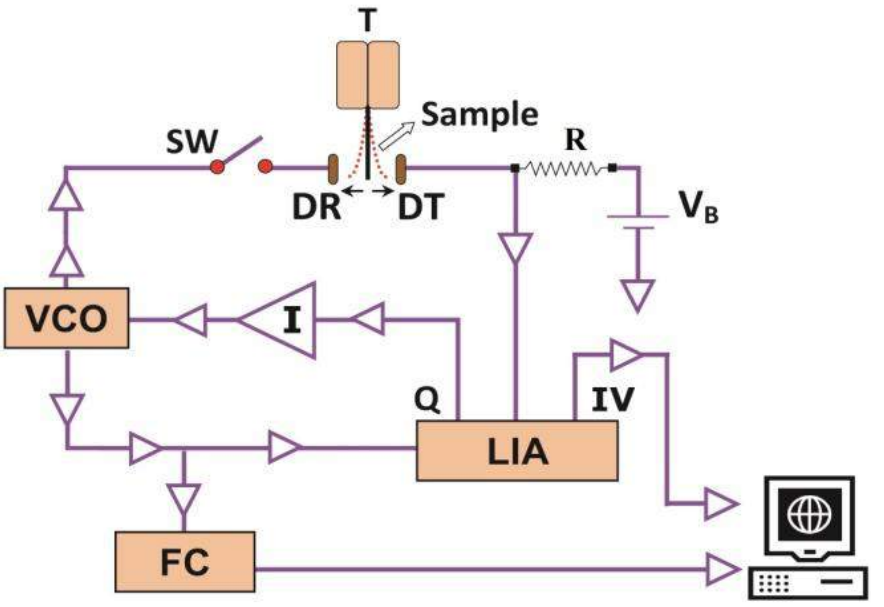

Figure 2.20: Schematic of the basic of vibrating reed apparatus.

Here the keywords are represented as temperature-controlling block (T), driver electrode (DR), detector electrode (DT), biasing resistor (R) (50 MΩ), bias voltage (V_B) (typically 90 V), lock-in amplifier (LIA), quadrature output (Q), integrator and feedback control (I), voltage-controlled oscillator (VCO), frequency counter (FC) (with averaging facility), frequency to voltage controller (FVC) switch (SW) to turn the excitation on or off. A resonating fixed free cantilever method was used to measure the dynamic elastic properties (real part- $\frac{\delta v}{v}$, imaginary part- Q^{-1}) of the sample. One end of the sample was clamped firmly between two well polished copper blocks attached to the base plate of the cryostat. The coaxial and insulated electrodes were kept on both sides at the other end of the sample, such that there was a small gap between the electrode and the sample. Since the sample holder was grounded, the whole system was grounded through the cryostat, hence electrode are well shielded. One of the electrodes, denoted by DR (Drive electrode) was connected to a VCO which generated a sine wave of frequency f_o that set the cantilever to oscillation due to electro-static coupling. The other electrode, DT, electrostatically picked up the signal from the oscillating bar and fed to the lockin amplifier, LIA, for detection. When there was a resonance of the bar while driving frequency is scanned, the output signal reaches maximum. The equation for resonance is

$$f_r = \left(\frac{d}{4\pi\sqrt{3}}\right)\left(\frac{1.875}{l}\right)^2 v = \left(\frac{d}{4\pi\sqrt{3}}\right)\left(\frac{1.875}{l}\right)^2 \sqrt{\frac{Y}{\rho}} \qquad [2.14]$$

Where d and l are the thickness and length of the resonating bar and f_r is frequency. It can be seen that the frequency is dependent on $1/l^2$, but there is a problem in its inaccurate determination. That is because there is always a small yielding of the damping substrate adding to an uncertainty in accurate determination of l. Therefore we measured $\frac{\delta v}{v} \propto \frac{\delta f}{f_{ref}}$ where f_{ref} was the resonance frequency at a reference temperature (generally the starting temperature) was taken, so $\frac{\delta v}{v} = 0$ at this point and we can write $\frac{\Delta v}{v_o} = \frac{\Delta f}{f_o} = \left(\frac{f - f_o}{f_o}\right)$. The absolute value of internal friction Q^{-1} was then calculated using the formula:

$$Q^{-1} = \Delta f / f_{res} \qquad [2.15]$$

Where, Δf was the width of resonance curve between the points where the value of amplitude was $\frac{A_{max}}{\sqrt{2}}$ and f_{res} was found at A_{max}. Since it is less ambiguous to find the zero crossing than look for a peak amidst noise in the data, we opt to find out Q^{-1} by fitting a Lorentzian in the real part, as following -

$$y = \frac{A({x_o}^2 - x^2)}{(x^2 - {x_o}^2)^2 + {x_o}^2 * \Gamma^2} \qquad [\Gamma = 2\pi\Delta f \text{ and } x_o = 2\pi f_{res}] \qquad [2.16]$$

In order to continuously measure Q^{-1} and $\frac{\delta v}{v}$ as the sample temperature was varied, a special phase locking loop was provided. That tracked the system in resonance all the time. The f_{res} at any temperature was now available in the frequency counter (Fc) and

$${Q^{-1}}_T = Q_r^{-1}\left(\frac{f_T}{f_r}\right)^2\left(\frac{A_r}{A_T}\right) \qquad [2.17]$$

Where f_r, A_r are resonance frequency and amplitude at a reference temperature and f_T, A_T are at any arbitrary temperature, T. Q_r^{-1} is the absolute value of Q^{-1}at the reference temperature.

2.7.2. Measurement:

Fig. 2.21 is showing the inner side and outer part of the cryostat. In the inner part a sample (~12.7 mm long) was clamped by two copper flats like a cantilever. The free end of the sample was placed between two coaxial electrodes. The inner side has a temperature controlled block to measure the temperature with a PT100 thermometer as shown in Fig. 2.21 (left side). The free end of the sample vibrated with maximum amplitude for resonance frequency f_{res}. The outer part is shown in Fig. 2.21 (right side) is covered with a Helmholtz coil that had 20Ω resistance. We could apply an uniform 300 Oe magnetic field into the sample, when this was dipped in LN_2, so that its resistance was lowest. The earth magnetic field was ignored due to very small value compared to our applied magnetic field.

The cryostat was connected with the rotary vacuum including diffusion pump. So when the cryostat was in well vacuum condition ($\sim 10^{-3}\ mBar$) then it is dipped inside in

liquid nitrogen. Due to big cryostat the inner chamber was slowly cooled down to 100K as well as the sample was also cooled down by conduction process by copper block without any heat loss. Then the heating process was done by removing the LN_2 bath slowly.

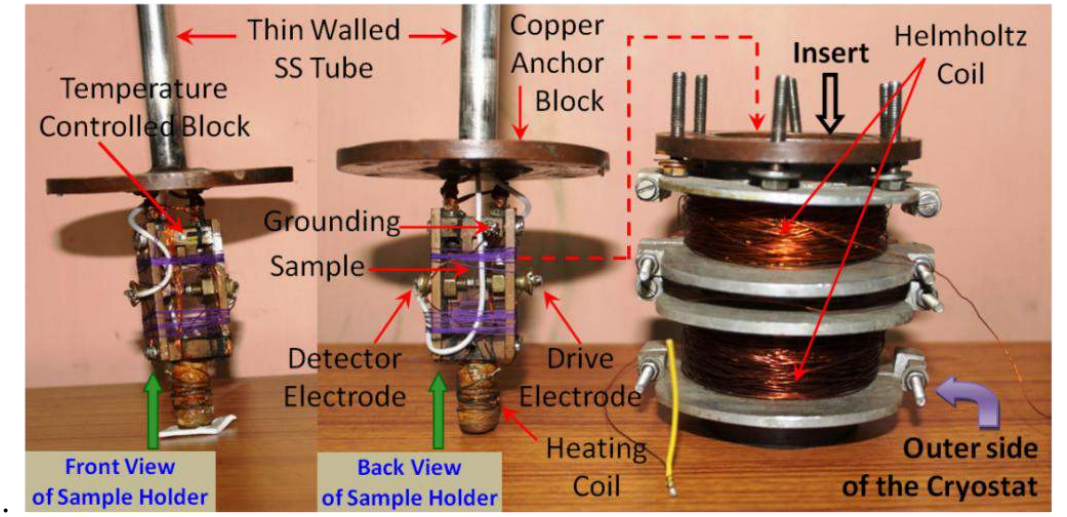

Figure 2.21: Vibrating reed apparatus with outer side with Helmholtz coil, sample holder and cryostat assembly

All the hardware parts is shown in Fig. 2.22 which includes multimeters, Lock-in amplifier, cryostat, frequency counter and a vacuum pump as the main parts of the VBR apparatus.

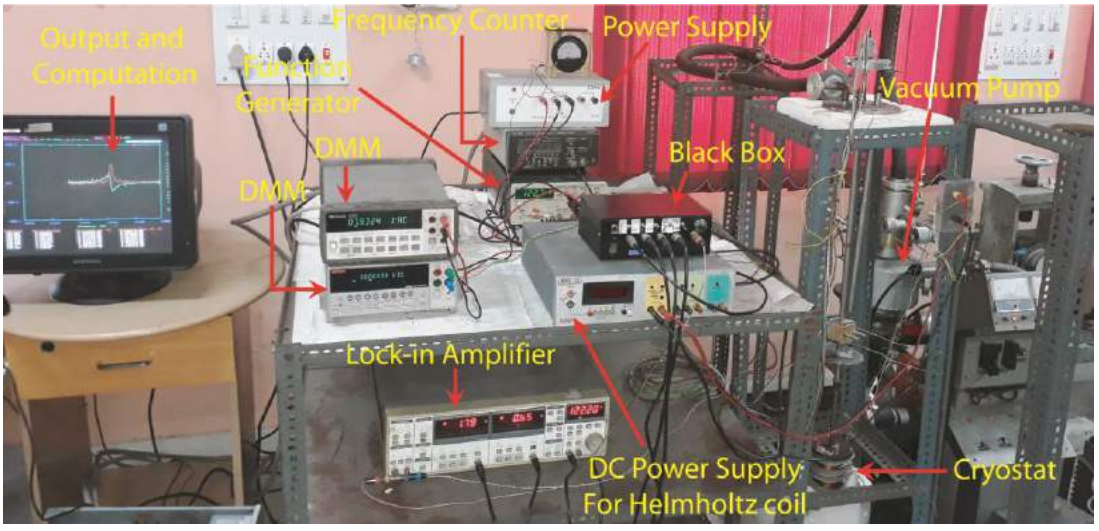

Figure 2.22: Experimental arrangement of the components used for sound velocity and internal friction Measurement.

2.8. DC Magnetization Measurement:

2.8.1. Measurement by vibrating sample magnetometer (VSM):

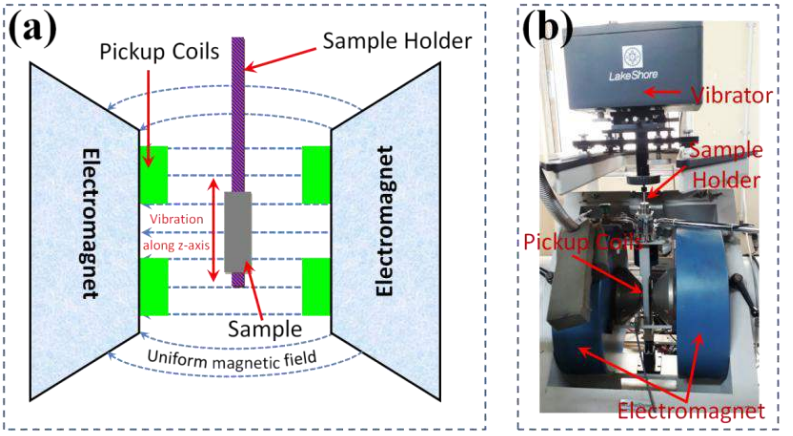

Figure 2.23: Schematic of vibrating sample magnetometer (VSM)

Vibrating sample magnetometer (VSM) [72] was used to measure dc magnetization of the samples as a function of temperature and magnetic field. The basic principle which this measurement relies on is the Faraday's law of induction according to which changing magnetic flux induces a voltage. Under a magnetic field H, a moment m is induced in the material. The sample to be studied is placed within suitably placed pick-up coils under an applied magnetic field which magnetizes the sample. The sample is given a vertical sinusoidal mechanical oscillation due to which magnetic flux enclosed by the pick-up coils changes as a function of time. Consequently, according to Faraday's law, this changing magnetic flux induces a voltage in the pick-up coils. The induced voltage in the pick-up coil is given by $V_{coil} = \frac{d\phi}{dt} = \frac{d\phi}{dz}\frac{dz}{dt}$ where ϕ is the magnetic flux enclosed by the pick-up coil, z is the vertical position of the sample with respect to the coil. For sinusoidal oscillation of the sample, Vcoil is proportional to the magnetic moment of the sample and is given by $V_{coil} = KmA\omega\sin(\omega t)$ where K is the coupling constant, m is the dc magnetic moment of the sample, $\omega = 2\pi f$ where f is the frequency of oscillation of the sample and A is the amplitude of oscillation. A schematic of a VSM system is shown in Fig. 2.23. We used a commercial VSM system for magnetization measurement of the samples from Lake Shore Cryotronics™ VSM. The VSM system from Lake Shore Cryotronics has two different cryostats, one for low temperature measurement in the temperature range 80 K – 400 K and another one for measurement in the high temperatures in the range 300 K – 1273 K. The maximum magnetic field available in this system is ±1.6 T.

2.8.2. Measurement by SQUID:

The superconducting quantum interference device (SQUID) is a highly sensitive magnetometer which operates based on Josephson effect and flux quantization (a magnetic flux quantum $\Phi = \frac{h}{2e} = 2.0678 \times 10^{-15} Tm^2$ where h is the Plank constant and e is the electron charge). The Josephson effect [73] is an example of macroscopic quantum phenomena: when two superconductors are separated by a thin insulating layer, tunneling of Cooper pairs of electrons through the junction occur even in the absence of an applied voltage. In dc Josephson effect, a current proportional to the phase difference of the wave functions flow through the junction in absence of an externally applied voltage while in ac Josephson effect the Josephson junction oscillates with a characteristic frequency proportional to the voltage applied across the junction. SQUID based on both dc Josephson effect (dc-SQUID) and ac Josephson effect (RF-SQUID) have been made. In a dc-SQUID, a superconducting loop is interrupted by two Josephson junctions placed in parallel. When a magnetic flux is applied perpendicular to the plane of the loop, the loop responds with a current due to the quantization of flux. The critical current and the SQUID output voltages are periodic functions of the externally applied flux.

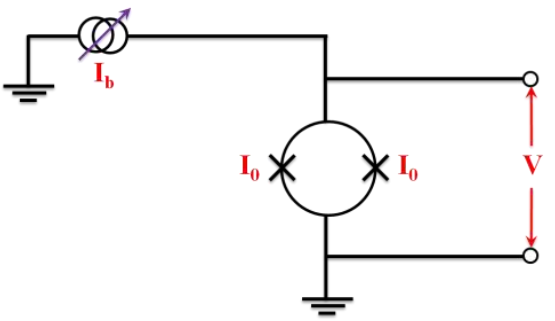

Figure 2.24: Schematic of a SQUID where I_b and I_0 are respectively the bias current and critical current, Φ is the flux threading the SQUID and V is the voltage response of that flux.

A schematic of SQUID is shown in Fig. 2.24. In this thesis Quantum Design™ magnetic property measurement system® (MPMS) SQUID was used to measure magnetization of the samples in the temperature range 2 K – 300 K and in the field range up to 7 T. Here the measurements are performed by moving the sample through superconducting detection coils. As the sample moves through the superconducting coils, the magnetic moment of the sample causes the change in magnetic flux enclosed by the pick-up coils. These superconducting pickup coils are inductively coupled to a SQUID

sensor and so the change in the signal of the pick-up coils is reflected in the SQUID output voltage. The SQUID magnetometers have sensitivity higher than that of a conventional VSM system (about 100 times) and can be used to detect very small magnetizations in the samples that are otherwise unreliable when measured using a conventional VSM system.

2.9. AC susceptibility setup and measurement:

Magnetic susceptibility is directly associated with the magnetic response of any system in a nondestructive way. During measurement, the moment of the sample changes in response to an applied magnetic field, allowing dynamics of the magnetic system to be studied, this provide a wide variety of information about its magnetic properties like the phase transition and relaxation phenomena. . The susceptibility measurement can be performed by either dc magnetometer (χ_{dc}) or an ac susceptometer (χ_{ac}), both techniques give slightly different information about the magnetic character of the samples. The χ_{ac} measurement can be performed under very small oscillating magnetic field, with or without an external dc biasing field. In the ac measurement, the moment of the sample changes in response to an applied ac field, allowing dynamics of the magnetic system to be studied, this provide a wide variety of information about its magnetic properties. The ability to measure higher harmonics as a function of both temperature and frequency help in distinguishing various kinds of interaction taking place in the system.

2.9.1. Theory of measurement:

In general, the magnetic susceptibility (χ) of an isotropic substance is defined as the intensity of magnetization acquired by an infinitely thin bar placed lengthwise in a uniform field of unit magnetic force. For an ideal sample (no demagnetizing force is present) placed in the uniform magnetic field (H) with magnetic moment per unit volume(M), the magnetic susceptibility is defined as

$$\chi = \frac{M}{H} \qquad [2.18]$$

Usually χ is measured using above relation, by applying static magnetic field H and measuring corresponding magnetization M in the sample [74, 75]. However, this method fails when M is not directly proportional H, the susceptibility is then measured using ac susceptibility technique. In order to measure ac susceptibility, the sample is generally driven with an applied ac magnetic field (H_{ac}). The magnetic moment of the sample

follows the applied field cycle. As a result, χ is due to the changing moment of the sample as it responds to the ac field and not to the moment itself as in dc technique. The χ in this case is given as

$$\chi_{ac} = \frac{\partial M}{\partial H_{ac}} \qquad [2.19]$$

Thus, the χ_{ac} is actually the slope (dM/dH) of the magnetization curve (M versus H curve) in the limit of small ac fields, and this is why sometimes referred to as a differential susceptibility. A small amount of dc biasing field can be added with this ac field so that sample moment remains uniform during the measurement time. In such a case sample will experience an external magnetic field $(H_{ext} = H_{dc} + H_{ac})$ having the static component H_{dc} and ac component H_{ac} characterized by the frequency $f = \omega/2\pi$ and amplitude H_a given by,

$$H_{ac} = H_a \cos(\omega t) \qquad [2.20]$$

In general, using equation (2.20) the ac susceptibility of a material with magnetization (M) can be expanded in power series of oscillating magnetic field (H) as,

$$M(t) = \sum H_{ac}(\chi_n^{'} \cos(n\omega t) + i\chi_n^{''} \sin(n\omega t)) \qquad [2.21]$$

where n represent the order of the harmonics. The real $(\chi_n^{'})$ and imaginary $(\chi_n^{''})$ part of the susceptibility are then given by:

$$\chi_n^{'} = \frac{1}{\pi H}\int_0^{2\pi} M(t) \sin(n\omega t)\, d(\omega t) \qquad [2.22]$$

$$\chi_n^{''} = \frac{1}{\pi H}\int_0^{2\pi} M(t) \cos(n\omega t)\, d(\omega t) \qquad [2.23]$$

Here n=1 denotes the fundamental susceptibility while n= 2, 3, 4… etc are the higher order harmonics associated with nonlinear terms in χ. $\chi_1^{'}$ and $\chi_1^{''}$ represent the fundamental real and imaginary components associated with the dispersive magnetic response and adsorptive dissipation within the sample respectively [74, 75]. In addition we measured χ upto second and third order harmonics and used the modulus χ_2 and χ_3 respectively in this thesis.

2.9.2. Instrumental setup and measurement:

The ac susceptibility is measured using a indigenous ac magnetic susceptometer. Here also for the measurement, mutual inductance principle [75] was utilized. Hence, this susceptometer consists of a secondary coil covered by a primary coil as illustrated in Fig. 2.25. These two coils were wrapped on a hollow type cylindrical Borosil^{TM} tube of 4cm diameter and 15cm length. In the primary coil, roughly 864 turns of 28 gauge copper wire was made and the resistance at the end of the wire was 11.7Ω. On the other hand the secondary coil consisting of two counter wound coils in opposite directions and electrically connected in series. Roughly, 850 turns were given per coil using 36 gauge enamelled copper wire and total resistance was 173Ω. These were used as pickup coils occupying opposite halves of the primary coil volume.

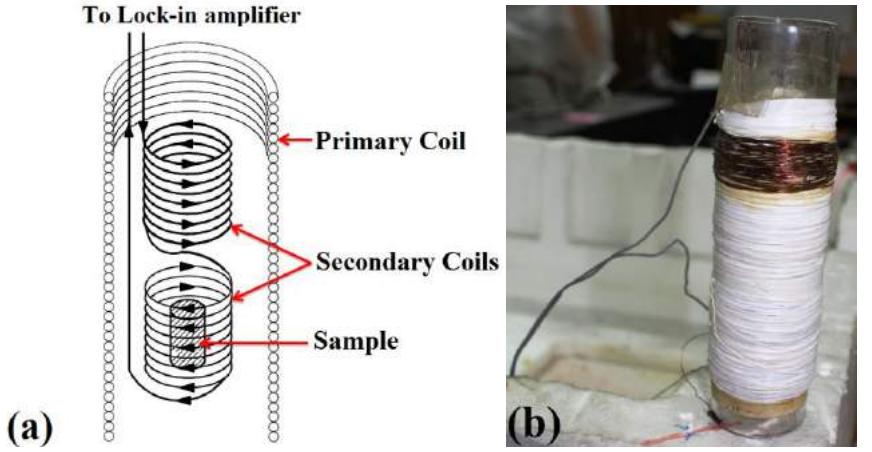

Figure 2.25: Arrangement of the susceptometer (a) primary coil (cut-away), the secondary coil and the sample and (b) the ac susceptibility system used in measurement

The sample is placed in one of the pickup coils while the other pickup coil is left empty. The primary (excitation) solenoid coil produces a nearly uniform ac magnetic when driven by an ac source. The ac voltage V across the secondary coil is due to Faraday induction

$$V = -\frac{d\Phi}{dt} \qquad [2.24]$$

Where, Φ is the net flux through the entire secondary coil (both the sample and reference coil) and includes contributions from both the applied field and the field due to the sample magnetization. The self-induced flux from the secondary can be neglected because the

secondary is connected only to high impedance $(10M\Omega)$ voltage metering equipment (oscilloscope, lock-in) and thus carries negligible current. The net secondary flux due to the applied field should be zero as two pickup coils were wound in opposite directions and connected in series. But a small amount of net secondary flux due to an effective mismatch area of winding wire was present that was responsible to create some secondary signal of $V = -d\Phi_{mm}/dt$ (called the mismatch signal) even with no sample present. This problem was solved by calibrating the primary coil by slight modification of the turns in primary coil at liquid N_2 temperature to zero offset. Hence, the flux was balanced enough resulting the secondary voltage nearly zero without sample. Fig. 2.26 is a schematic of the experimental setup of susceptibility measuring tool.

In the complete setup the primary coil was driven by ac source consisting of Stanford Research System DS-360™ Ultra Low Distortion Function Generator followed by a power amplifier. In parallel to the power amplifier, a Kiethley 2000™ multimeter and an HP 34401™ multimeter were connected in parallel to the coil to measure the AC and DC inputs through the primary coil respectively.

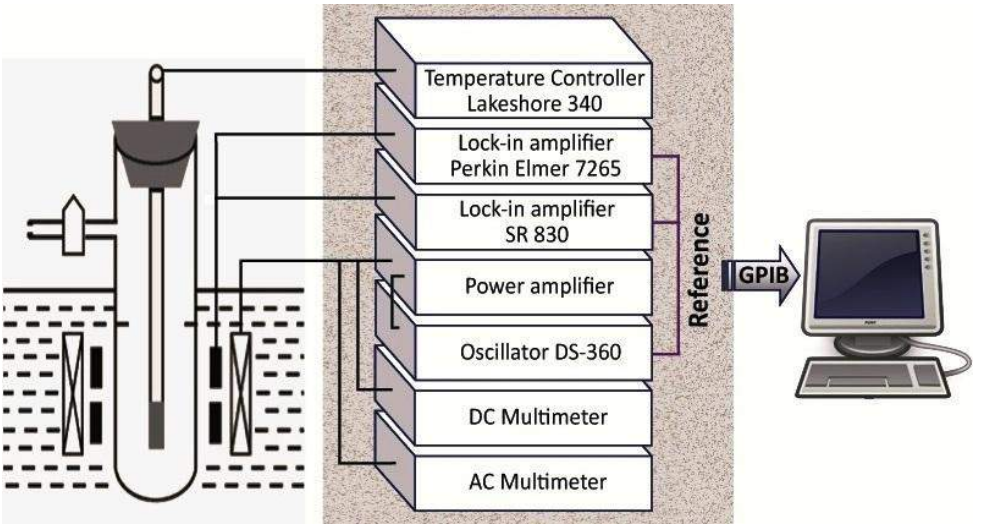

Figure 2.26: Schematic of the experimental setup used for ac susceptibility measurement.

The secondary coil was connected in parallel to Perkin Elmer DSP 7265™ and SR-830™ lock-in-amplifiers. One two channels digital oscilloscope from Metravi DSO-5025E was connected at the input and output to see both the signals together. A cryostat was also made to perform measurements within temperatures of 80 K to 400 K. The design and picture of the cryostat is given in Fig. 2.27.

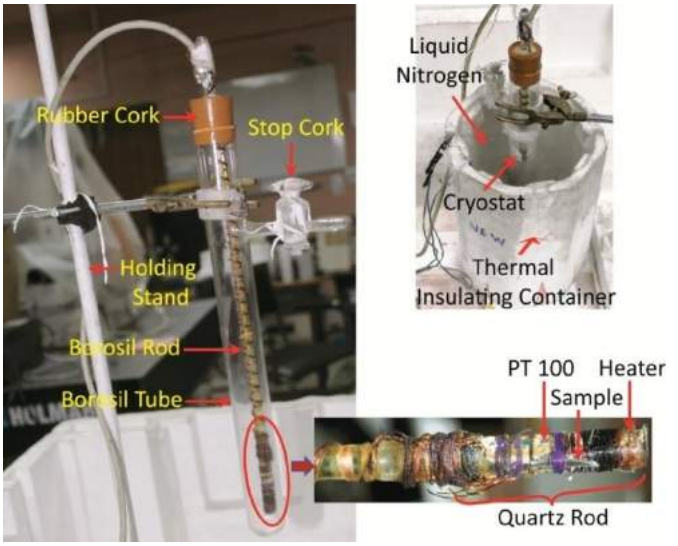

Figure 2.27: Cryostat set up for ac susceptibility measurement in temperature range of 80-400 K. The enlarged region shows the magnified view of the sample area, heater and thermometer.

Sample was kept on sample holder made of quartz (it is also very weakly diamagnetic and is a good thermal conductor). A calibrated Pt-100 thermometer was placed on sample holder such that sample could be placed in contact with it. The quartz holder was attached to a Borosil® rod at one end to provide thermal isolation. To heat the sample assembly a heater wire was wound at the other end of the sample holder in bi-filler arrangement to prevent any magnetic field from generating. A rubber cork was attached on the Borosil rod as shown in the Fig. 2.27, wires were taken out to connect the thermometer and heater wires with LakeShore 340™ temperature controller to measure and control the temperature. The rod assembly was then inserted in a Borosil tube which had a pumping valve to create vacuum using a rotatory vacuum pump. The real and imaginary parts of liner susceptibility were measured by the DSP 7265 lock-in-amplifier and higher harmonics were mostly measured using a SR-830 lock-in-amplifier. The entire set-up was connected to computer using GPIB and automated using a visual Quick Basic programming language. Program was designed to make compensation for the off-set voltage in the secondary coil using DSP 7265 lock-in-amplifier. The Lock-in amplifiers were used to measure the susceptibilities simultaneously, so the experiments could be finished together. In fact, since it was possible to program DSP 7265 as two virtual lock-in-amplifier, running at different harmonics simultaneously, we used it to measure two harmonic susceptibilities $\chi'(2\omega)$, $\chi''(2\omega)$, $\chi'(3\omega)$, $\chi''(3\omega)$ simultaneously running the SR830 in parallel to measure the fundamental $\chi'(\omega)$ and $\chi''(\omega)$ all at the same temperature and time.

2.9.3. Calibration of the ac susceptibility setup:

At first the magnetic field inside the coil was measured as a function of depth of the coil (kept in vertical position). A current of 1 A DC was passed through the primary coil at room temperature and the resultant magnetic field was measured with a Hall probe. We marked the depth position near the lower coil where the magnetic field is maximum and uniform. The cryostat was positioned in a manner such that the sample area lied within the lower coil of the secondary system. To determine the value of the field at which measurement was performed, we measured the maximum field inside the coil by varying current through the primary coil up to 1.8A dc as shown in the Fig. 2.28.

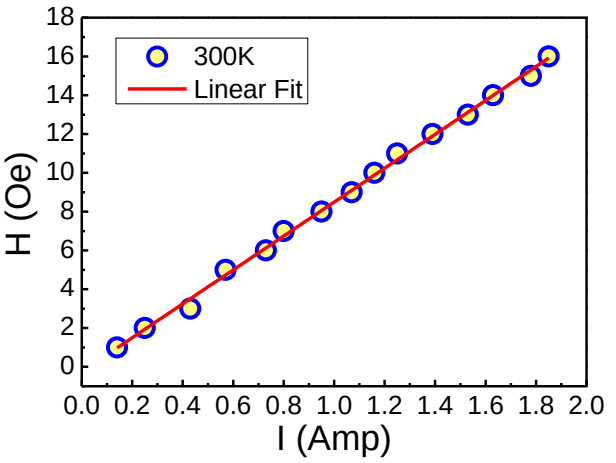

Figure 2.28: Magnetic field inside the secondary coil as a function of current in the primary coil of ac susceptometer.

The field in the coil increased linearly with increasing the current at 300K. The slope and offset were calculated from the linear fitting ($Y = mX + C$). Therefore, the coil was kept deep inside the liquid Nitrogen for half an hour and the measured resistance (R_{LT}) of the primary coil was 2.4Ω at low temperature ($\sim 80K$). Hence, for the applied $2V$ of ac electric field the ac current (I_{ac}) was 0.83A and for 0.2V dc current (I_{dc}) was 0.08A. Now with the value of slope and offset the measured magnetic field for ac current was about 7 Oe and for dc current it was 0.48 Oe. Finally the whole system including thermometer was calibrated using Fe-Ni-Cr as a standard sample because the T_C of this sample is well-known and the measured value matches with the standardized data of this sample.

Chapter 3

Investigations on $Co_{(42-x)}Ni_{(31+x)}Al_{27}$ (x=0, 1) System

Structure and microstructure play the key role in any physical properties of an alloy. We have choosen the Co-Ni-Al system as FSMA material due to superior mechanical strength and good hot/cold workability. This happens due to the growth of non-FSMA γ phase precipitates as intergrain component of the main β phase grains of the FSMA material. In this chapter we shall discuss about such an FSMA with the chemical formula of $Co_{(42-x)}Ni_{(31+x)}Al_{27}$ $(x = 0, 1)$. *Slight amount of Co decreasing in general shifted the structural transition temperature towards room temperature. By preparation these Co-Ni-Al FSMAs formed polycrystalline structure and contains dual phases (β and γ). The percentage of γ phase fraction was higher in the sample with less Co which enhanced the mechanical strength of the sample and this highly impacts on the dynamic elastic properties as well as magnetization and the other physical properties. Thermal hysteresis during structural transitions was also increased due to lowering the at% of the Co in that Co-Ni-Al system.*

3.1. Co-Ni-Al system with two different compositions:

3.1.1. Structures and microstructures:

We prepared Co-Ni-Al system with different nominal compositions using the chemical formula as $Co_{(42-x)}Ni_{(31+x)}Al_{27}$ $(x = 0,1)$. Both the alloys were prepared by using the Tri-arc furnace as described in section 2.1.1. To homogenize, samples were sealed in evacuated quartz tubes, annealed at 1473K for 72 hours and then quenched in ice water as mentioned in section 2.1.2. EDAX analysis was used to confirm the composition of the alloys. The XRD analysis of these two samples in Fig. 3.1 shows the peaks corresponding to two different phases in the two samples. The respective arrangements of odd/even super lattice peaks of (100), (111), (110), (200), (210), (220), (211) confirm the presence of β phase (B2 structure) and γ phase (A1 structure) [59]. The β phase is the Austenite phase that carries the main FSMA properties and has the BCC structure of Pm3m space group. [76]. The B2 phase matrix undergoes martensitic transformation into the tetragonal L10 structure (space group P4/mmm). The transformation mechanism is very similar to the Ni-Al alloy including precursors, tweed structure and softening of the phonon modes [77]. The other one is non-FSMA γ phase with of Fm3m space group and has A1 type disordered structure only enhance of mechanical strength as well as ductility [26]. Two adjacent peaks at approximately $2\theta = 45°$ is the characteristic peaks of presence of β and γ adjointly.

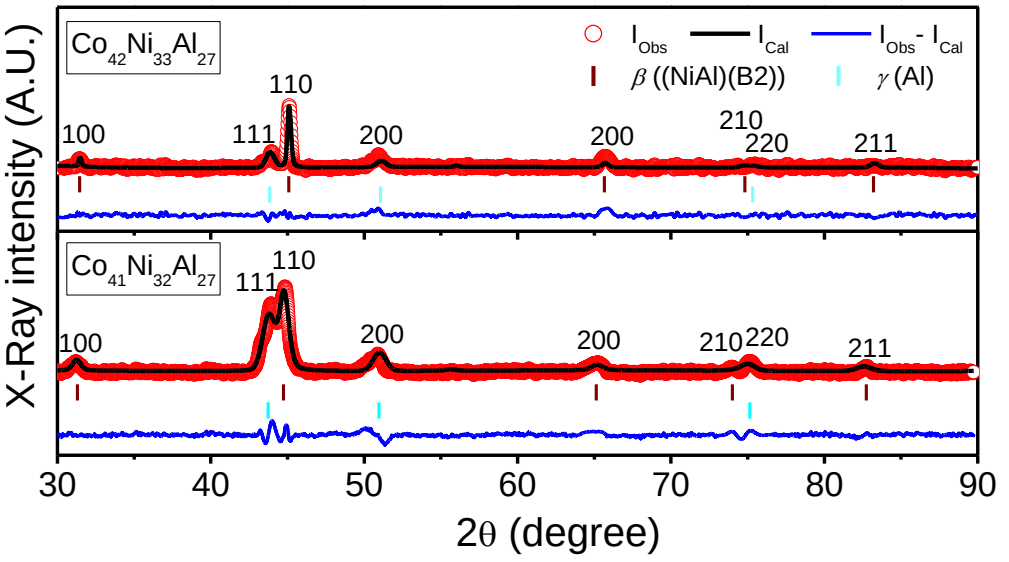

Figure 3.1: XRD patterns (I_{Obs}) of $Co_{42}Ni_{31}Al_{27}$ and $Co_{41}Ni_{32}Al_{27}$ along with the calculated patterns (I_{Cal}), differences between the observed patterns and calculated patterns ($I_{Obs} - I_{Cal}$) and peak positions fitted (vertical bar)

Scanning electron micrographs (SEM) of $Co_{42}Ni_{31}Al_{27}$ and $Co_{41}Ni_{32}Al_{27}$ shown in Fig. 3.2 also corroborate the findings of XRD. The darker spots are β and γ is shown in the lighter contrast [78].

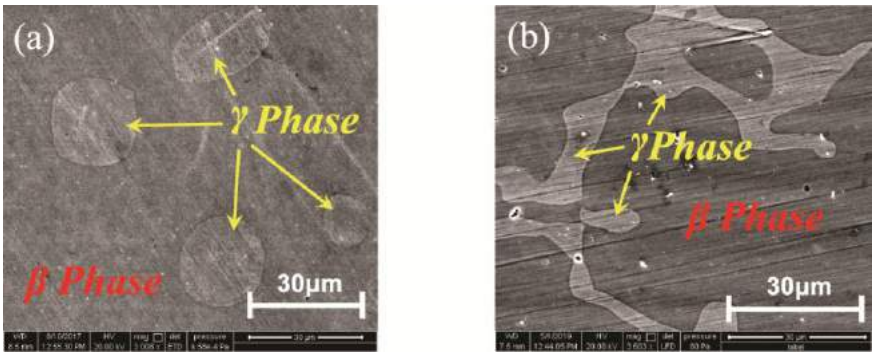

Figure 3.2: SEM micrograph (B2 matrix surrounded by γ phase) and spectroscopy of energy dispersive X-Ray (EDAX) analysis of (a) $Co_{42}Ni_{31}Al_{27}$ and (b) $Co_{41}Ni_{32}Al_{27}$

However, the structural parameters as well as the improvement of γ phase by heat treatment was obtained by Reitveld refinement using Fullproof software [79]. Fig. 3.1 shows the fitting of experimental data with the calculated data for Fm3m and Pm3m space group from this software. The red circles are the experimental data (I_{obs}), the solid black line is the calculated pattern (I_{cal}) and the bottom curve is the difference between the observed and calculated patterns$(I_{obs} - I_{cal})$. For good fitting of data the difference between observed and the calculated value should be minimum. In the vertical marks below the profile show the Bragg positions corresponding to β and γ phase. The mathematical analysis of Rietveld analysis has been reported earlier [57–60]. From the analysis of data it is found that in $Co_{41}Ni_{32}Al_{27}$ the volume fraction (%) of γ phase is higher. We compared in between 42% and 41% of Co keeping Al percentages fixed in the whole composition. The unit cell parameters and volume fractions of these alloys have been revealed into table 3.1.

Table 3.1: XRD data analysis and Structural parameters of the unit cell obtained by Rietveld refinement; χ^2 shows the Goodness of fitting $\left(\text{GOF} = \sqrt{\chi^2}\right)$ and V is the unit cell volume.

Compositions	Crystal Structure	Phase Fraction (%)	Cell Parameters	χ^2
$Co_{42}Ni_{31}Al_{27}$	Phase: β (B2) Space group: Pm-3m	97.6 ± 1	a = b = c = 2.84 (Å) V = 22.95 (3) ($Å^3$)	1.88
	Phase: γ (Al) Space group: Fm3m	2.3 ± 0.1	a = b = c = 3.57 (Å) V = 45.65 (1) ($Å^3$)	
$Co_{41}Ni_{32}Al_{27}$	Phase: β (B2) Space group: Pm-3m	94.2 ± 0.7	a = b = c = 2.86 Å V = 23.44 (1) ($Å^3$)	2.81
	Phase: γ (Al) Space group: Fm3m	5.8	a = b = c = 3.58 Å V = 45.93 (2) ($Å^3$)	

EDAX studies confirmed nominal compositions of the alloys. We then calculated the ratio of electron to atom (e/a) using following expression as described in detail in [80]

$$e/a = \frac{[9X_{Co} + 10X_{Ni} + 3X_{Al}]}{[X_{Co} + X_{Ni} + X_{Al}]} \qquad [3.1]$$

where X is the at% of the elements measured by EDAX. The nominal percentage and the e/a ratio have been shown in table 3.2.

Table 3.2: Elemental at% and (e/a) inside different compositions of Co-Ni-Al FSMA.

Compositions	Elements (At%)			e/a (at.%)
	Co	Ni	Al	
$Co_{42}Ni_{31}Al_{27}$	42.4 ± 0.1	31 ± 0.1	26.6 ± 0.5	7.71
$Co_{41}Ni_{32}Al_{27}$	40.3 ± 0.6	32.7 ± 0.1	27 ± 0.2	7.70

3.1.2. Resistivity:

The resistivity measurement is a standard method for structural transition observation for any FSMA [47]. Here the values and changes in resistivity correspond to the structural changes due to rearrangement of scattering centres. The low temperature resistivity of $Co_{42}Ni_{31}Al_{27}$ and $Co_{41}Ni_{32}Al_{27}$ was measured in an Oxford Instruments (T_M) closed cycle refrigerator using an a.c. excitation at 111.11 Hz and the temperature sweep was performed at 1 K/min for both heating and cooling cycles in between 4K to 300K. The data for two alloys are shown in Fig. 3.3 (a). The transformation temperatures were obtained from the slope changes in the cooling and heating parts of resistivity curves and given into table 3.3. The large changes allow us to mark out the four transition temperatures of each system. The temperatures are marked as martensite start (M_S), martensitic finish (M_f), Austenite start (A_S) and Austenite finish (A_f) shown in Fig. 3.3. In this case, for constant Al content, increasing Co amount M_S decreases and increases Curie temperature [81].

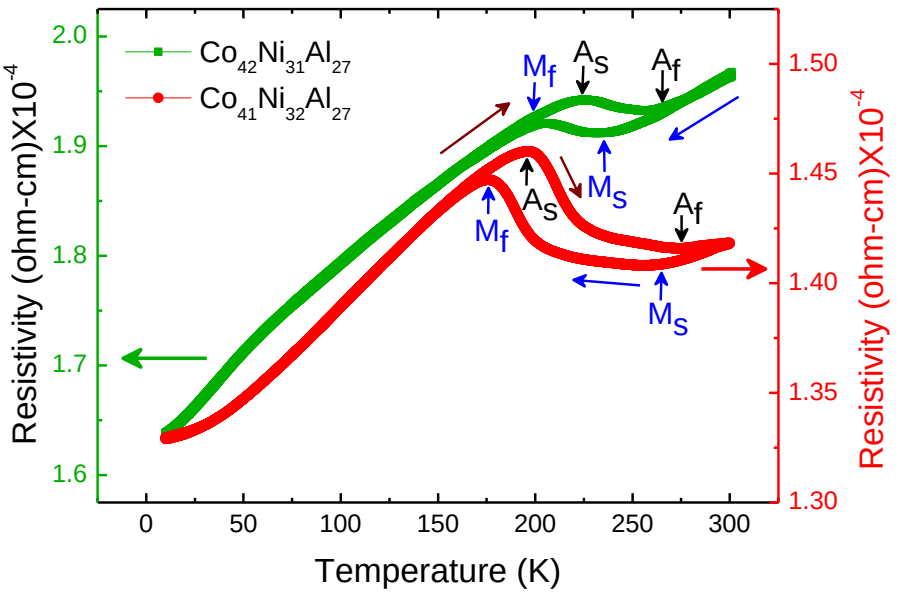

Figure 3.3 (a): Temperature dependence of resistivity of $Co_{42}Ni_{31}Al_{27}$ and $Co_{41}Ni_{32}Al_{27}$ annealed at 1473K for 72h showing SME during heating and cooling cycle.

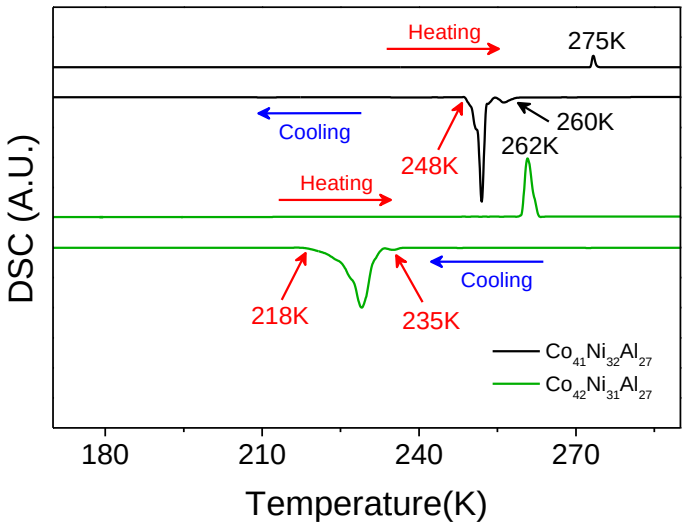

Figure 3.3 (b): Differential scanning calorimetry for $Co_{42}Ni_{31}Al_{27}$ and $Co_{41}Ni_{32}Al_{27}$ annealed at 1473K for 72h

Table.3.3: Structural transition temperatures and thermal hysteresis obtained from resistivity vs temperature.

Sample	T_{M_s}(K)	T_{M_f} (K)	T_{A_s} (K)	T_{A_f} (K)	ΔT (K) $\left(T_{M_s} - T_{M_f}\right)$	ρ (Ωcm) at 300K
$Co_{42}Ni_{31}Al_{27}$	235	201	224	263	34	1.97×10^{-4}
$Co_{41}Ni_{32}Al_{27}$	265	175	194	290	90	1.42×10^{-4}

3.1.3. Sound velocity and Internal friction:

Sound velocity and internal friction measurements were done on reed-shaped samples, about 11 mm long, 2.3 mm wide and 500 μm thick. A vibrating reed technique that is discussed in details in chapter 2 (Sec. 2.5) was used to measure changes in sound velocity $\left(\frac{\delta V}{V}\right)$ and internal friction (Q^{-1}) simultaneously on the sample as the temperature was varied. The Young's modulus (E) is proportional to the square of sound velocity ($v = \sqrt{E/\rho}$, ρ being the density of the material); therefore we plotted the sound velocity directly as a function of temperature, to reflect the changes in elastic property. Simultaneously temperature variations of the Q^{-1} shows the dissipation of mechanical energy inside that system during phase transition. Fig. 3.4 shows temperature dependent sound velocity $\left(\frac{\delta V}{V}\right)$ and internal friction (Q^{-1}) for the sample $Co_{42}Ni_{31}Al_{27}$ and $Co_{41}Ni_{32}Al_{27}$ alloy annealed at 1473K for 72h. The heating and cooling curves show remarkable elastic property changes near the transformations.

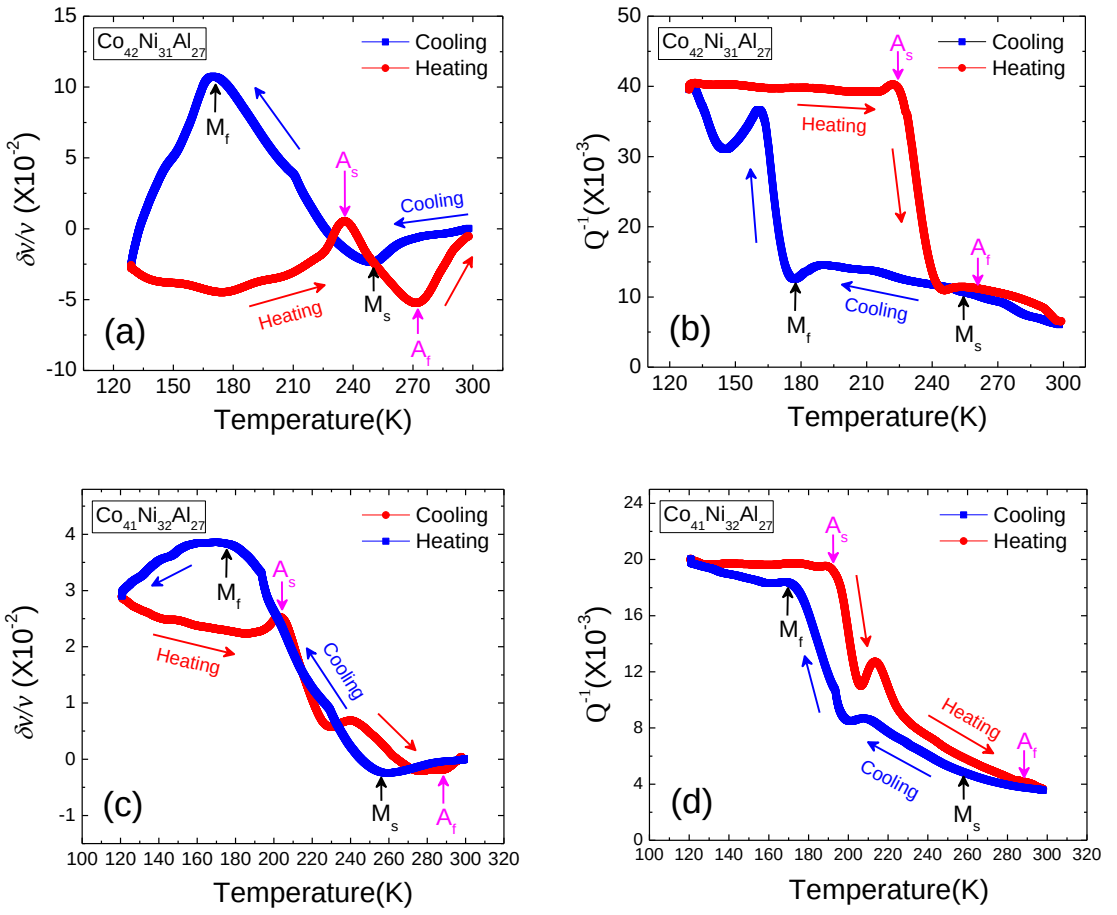

Figure 3.4: (a) Sound velocity and (b) internal friction (Q^{-1}) of CoNiAl FSMA for low temperature cycling of $Co_{42}Ni_{31}Al_{27}$ and $Co_{41}Ni_{32}Al_{27}$

However, the Co rich sample had the lower M_s temperatures. The $(\delta v/v)$ in the austenite phase initially decreased from room temperature values in both the samples, this seems to be the general trend of the FSMA materials. However, below the T_{MS}, the elastic property was regained at a marked pace in both. There was a rise below T_{AS} with lowering of temperature. This implies that there was an elastic recovery in the system. During heating up, the reverse process was retraced and the value at room temperature was regained. IF measurements showed similar trends. These showed kinks near structural transformations, while the Co rich sample showed a lot of damping at lower temperatures where the sound velocity also showed anomalous behaviour.

For the analysis of $\left(\frac{\delta V}{V}\right)$, i.e. the real part of E, we see from the Fig. 3.4 (a) that there are two different regions for elasticity that is before and after the transition starts and ends. This corresponds to pure Austenite and Martensite phases. As we discussed in previous chapter, total contribution was a sum of a temperature independent part coming from general elastic background and temperature dependent electronic and lattice ontributions during phase transitions. To estimate these extra contributions, we subtracted out the background by assuming a Debye type model [46, 47] as discussed in Sec.1.7.1 temperature dependent $\left(\frac{\delta V}{V}\right)$ is fitted using the relation as,

$$\frac{\delta v}{v} = A + BT^2 + CT^4 \qquad [3.2]$$

Where, $B = (d^2E/\,d\varepsilon^2)$ and $\mathrm{C} = (\mathrm{d}^2\mathrm{L}/\,d\varepsilon^2)$ as E and L are electronic and lattice contributions respectively for the corresponding elastic strain ε. Equation 3.2 is known to hold true for metallic alloys. Strictly, it should be valid for $T \ll \theta_D$, but generally found to be useful till 300 K for alloys. These contributions have been calculated from the fitting of $(\delta v/v)$ vs T from Fig. 3.4 (a). The fittings were done for both phases and for both cooling and heating parts of each run (Fig. 3.5 a–d). Since the experiment was not done in a magnetic field, we neglect the magnetic contribution. The fitting are found to be reasonably good. The numerical values of each contributions are given in Table 3.4.

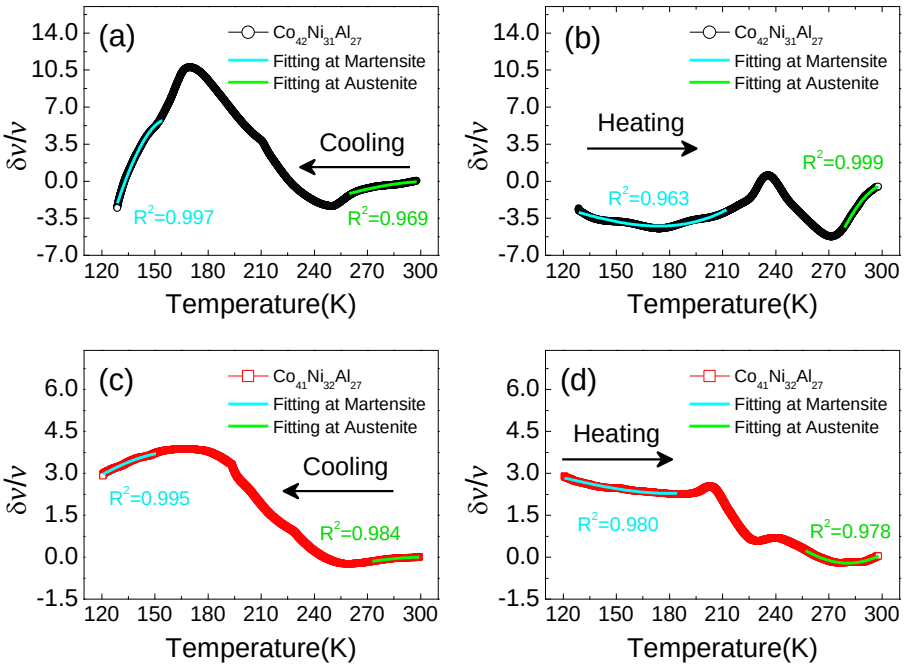

Figure 3.5: Power law fitting of SV curve for cooling and heating cycles of $Co_{42}Ni_{31}Al_{27}$ and $Co_{41}Ni_{32}Al_{27}$

Table 3.4: Variation of different contributions with the crystal structure calculated by power law fitting, B and C express from electronic contribution and lattice contribution respectively.

Samples	Cycle	Martensite region				Austenite region			
		Temp. Range (K)	A	B	C	Temp. Range (K)	A	B	C
$Co_{42}Ni_{31}Al_{27}$	Cooling	129-154	-0.77	5.8×10^{-5}	-1.2×10^{-9}	260-298	-0.14	3.1×10^{-6}	-1.6×10^{-11}
	Heating	129-212	0.02	-4.2×10^{-6}	6.9×10^{-11}	279-298	-1.65	3.6×10^{-5}	-1.9×10^{-10}
$Co_{41}Ni_{32}Al_{27}$	Cooling	121-151	-0.01	3.2×10^{-6}	-6.1×10^{-11}	273-299	-0.04	8.46×10^{-7}	-4.56×10^{-12}
	Heating	121-184	0.04	-1.1×10^{-6}	1.8×10^{-11}	257-298	0.16	-4.2×10^{-6}	2.7×10^{-11}

From the table it is found that in the austenitic region during heating and cooling B and C has higher variation in $Co_{41}Ni_{32}Al_{27}$.

3.1.4. DC Magnetization:

Magnetization measurements were performed in a LakeShore made vibrating sample magnetometer as discussed in Sec. 2.7 Temperature variations of zero-field-cooled (ZFC), field-cooled (FC), and field-heated (FH) measurements were carried out under an applied magnetic field of H = 150 Oe. The FC and ZFC magnetizations in H = 150 Oe for both the samples $Co_{42}Ni_{31}Al_{27}$ and $Co_{41}Ni_{32}Al_{27}$ are shown in Fig. 3.6 (a-b). During austenite to martensite transition in Co-Ni-Al system, a ferromagnetic to ferromagnetic

transition appears in the austenite phase (marked by T_C^A in Fig. 3.6 (a-b) in both the alloys where as the $Co_{41}Ni_{32}Al_{27}$ is showing the T_C^A above room temperature. We call the magnetic transition as ferromagnetic low (FL) and ferromagnetic high (FH) phases and this type of behavior is commonly encountered in these systems, for example, see ref. [42, 82].

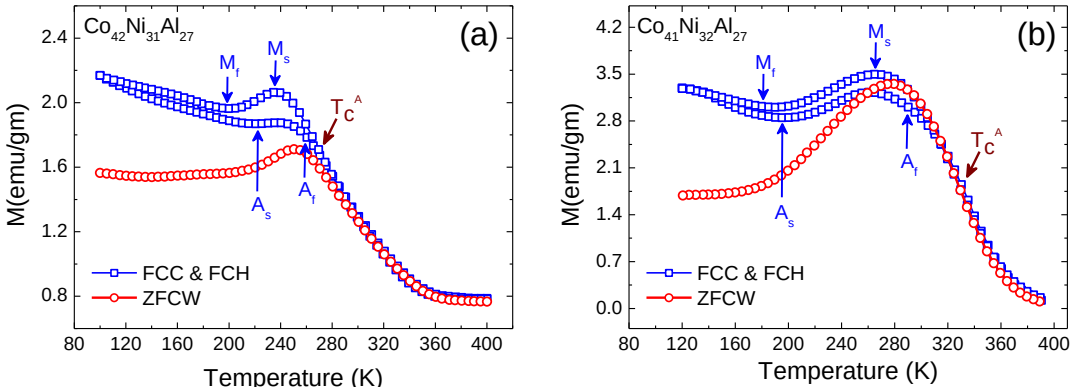

Figure 3.6: Temperature dependent ZFC, FCC and FCW magnetizations measured at H = 150Oe of $Co_{42}Ni_{31}Al_{27}$ and $Co_{41}Ni_{32}Al_{27}$ annealed at 1473 K for 72h. Arrows show the transition temperatures obtained from resistivity data.

3.1.5. AC susceptibility:

Susceptibility measurements were performed on the $Co_{42}Ni_{31}Al_{27}$ and $Co_{41}Ni_{32}Al_{27}$ from 300 K to 120 K at a frequency of 111 Hz and the data of ac susceptibility are shown in the Fig. 3.7. The real part (χ') of ac susceptibility are shown in Fig. 3.7 (a) and the imaginary part (χ'') in Fig. 3.7 (b). As temperature was lowered (χ') increased at the beginning and the peak fell, which shows that upon subsequent martensitic transition. The data showed similar features of similar FC of magnetization.

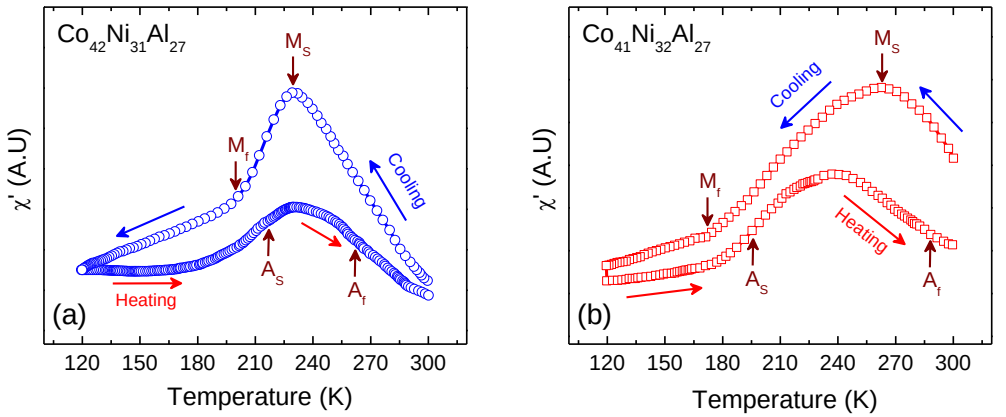

Figure 3.7: The real part of AC susceptibility in heating and cooling cycle at the frequency of 111Hz for sample (a) $Co_{42}Ni_{31}Al_{27}$ annealed at 1473K/72h and (b) $Co_{41}Ni_{32}Al_{27}$ annealed at 1473K/72h

We have also performed second and third harmonic measurements of on the sample and its magnitude χ_2 and χ_3 respectively. Fig. 3.8 (a), (b) and (c) shows the moduli of ac susceptibility with fundamental, second harmonic and third harmonic conditions respectively.

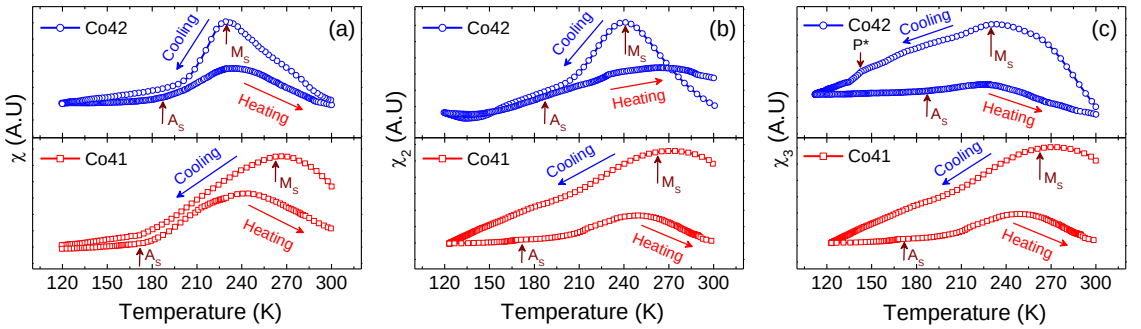

Figure 3.8: AC susceptibility obtained during same run (a) Fundamental (b) 2nd Harmonic and (c) 3rd harmonic of ac susceptibility obtained during same run.

We see that the nature of the fundamental modulus in Fig. 3.8 (a) is similar to χ'. In the 2nd and 3rd harmonic the blunt rise in susceptibility was found during heating shown in Fig. 3.8 (b) and (c). A small bump (P^*) near 145K is observed in 3rd harmonic susceptibility during cooling for the sample $Co_{42}Ni_{31}Al_{27}$ shown in Fig. 3.8(b). This is possibly due to completion of intermartensitic structural transformation which is also observed in internal friction (Q^{-1}) during cooling for the same sample.

3.2. Discussion:

We have prepared the CoNiAl FSMA with the variations of Co keeping the Al concentration fixed. In both the sample, the amount of γ phase volume fraction (%) was very less. The small amount of change in the Co concentration effected drastically on the structure and other physical properties. The γ phase had increased by ~ 2 times in $Co_{41}Ni_{32}Al_{27}$ sample due to favourable environment for less Co to form the γ phase. The thermal hysteresis has been increased in this sample also.

Chapter 4

Effect of heat treatments on CoNiAl FSMA

We followed a route of enhancement techniques to improve the structures and microstructures of CoNiAl system with different compositions and analyzed their crystal structures. The ratio of β to γ phase components can be changed by heat treatment and due to alteration of grain and intergrain microstructure, thus even affecting the structural transformation temperature range. Since the structural transformations involve a significant amount of change in elasticity, study of change of elastic modulus should show up during the transformations. We have reported here the sound velocity and internal friction (Q^{-1}) *measurements on CoNiAl system under different annealing conditions. The effect of annealing on other physical properties are also discussed in this chapter.*

4.1. Effect of Annealing on $Co_{39}Ni_{34}Al_{27}$:

4.1.1. Structures and microstructures:

Pure (99.99%) Co, Ni, and Al metals were taken at an appropriate weights to make the nominal composition of $Co_{39}Ni_{34}Al_{27}$. The sample was prepared by melting process as before in an tri arc furnace. The preparation techniques are discussed in sec. 2.1. The raw materials were melt to make a alloy ball. It was then sealed in a quartz ampoule and annealed at 1373 K for 24 h and then was quenched in ice cooled water. A piece of the sample was cut from the same ingot, followed by further annealed at a temperature of 1473 K for 72 h and similarly water quenched. The XRD patterns at the room temperature presented in Fig. 4.1 for $Co_{39}Ni_{34}Al_{27}$ show the peaks corresponding to both β and γ phases in the samples. The odd/even super lattice peaks of (100), (111), (110), (200), (220) and (211) found in these samples is the confirmation of FSMA β phase surrounded by the γ phase as before

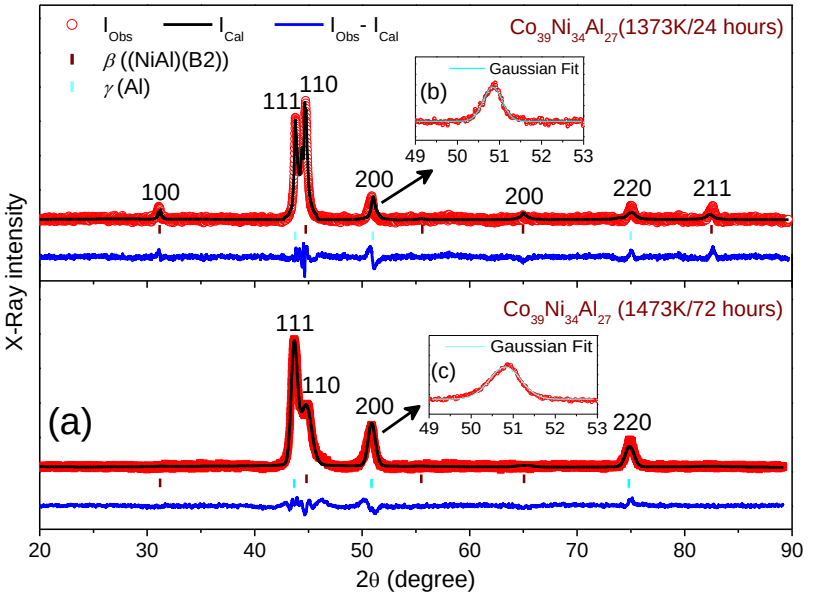

Figure 4.1: (a) Rietveld refinement plot of XRD data of $Co_{39}Ni_{34}Al_{27}$ annealed at 1373K/24h and 1473K/72h. (b) Gaussian fitting of the peak corresponds to γ phase of $Co_{39}Ni_{34}Al_{27}$ annealed at 1373K/24h. (c) Gaussian fitting of the peak corresponds to γ phase of $Co_{39}Ni_{34}Al_{27}$ annealed at 1473K/72h.

The SEM micrographs of $Co_{39}Ni_{34}Al_{27}$, given in Fig. 4.2 (a) and (b), show a two-phase structure with different contrasts, in both the samples. This gives evidence to the presence of β and γ phases, confirming the XRD data.

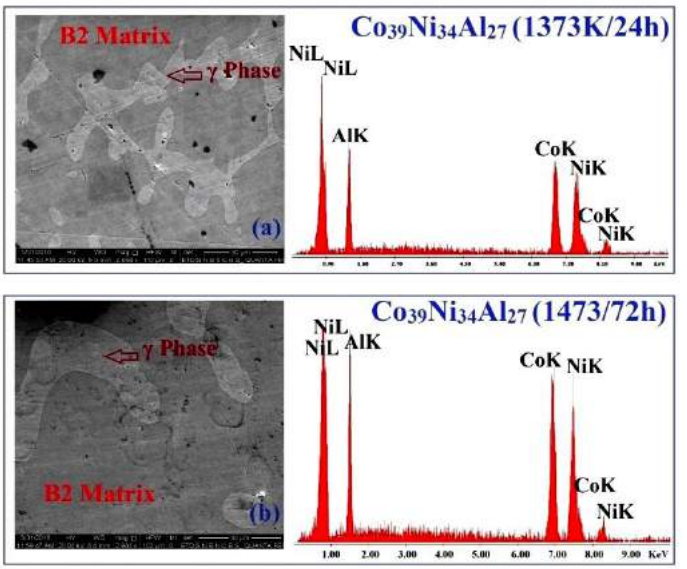

Figure 4.2: SEM micrograph (B2 matrix surrounded by γ phase) and spectroscopy of energy dispersive X-Ray (EDAX) analysis of (a) $Co_{39}Ni_{34}Al_{27}$ annealed at 1373K/24h and (b) $Co_{39}Ni_{34}Al_{27}$ annealed at 1473K/72h.

The structural parameters and phase volume fractions of $Co_{39}Ni_{34}Al_{27}$ obtained by Reitveld refinement are given in table 4.1. The crystallite size was calculated by Debye Scherer formula where line broadening at half the maximum was measured by Gaussian fittings. These are also included in that table.

Table.4.1: XRD data analysis of the $Co_{39}Ni_{34}Al_{27}$ and Structural parameters of the unit cell obtained by Rietveld refinement; χ^2 shows the Goodness of fitting $\left(\text{GOF} = \sqrt{\chi^2}\right)$ and V is the unit cell volume

Annealing Temperature (K)	Crystal Structure	Phase Fraction (%)	Cell Parameters	χ^2	Crystallite size in γ phase (m)	Lattice strain in γ phase
1373 For 24h	Phase: β (B2) Space group: Pm-3m	93.7	a = b = c = 2.87×10^{-10} (1) (m) V = 23.59×10^{-30} (m^3)	8.17	17.55×10^{-9}	0.0094
	Phase: γ (Al) Space group: Fm3m	6.3	a = b = c = 3.58×10^{-10} (1) (m) V = 45.85×10^{-30} (m^3)			
1473 For 72h	Phase: β (B2) Space group: Pm-3m	84.0	a = b = c = 2.86×10^{-10} (6) (m) V = 23.51×10^{-30} (3) (m^3)	4.64	9.67×10^{-9}	0.0170
	Phase: γ (Al) Space group: Fm3m	16.0	a = b = c = 3.59×10^{-10} (1) (m) V = 46.12×10^{-30} (m^3)			

It is observed that beside compositions, the γ phase is increased due to heat treatment in CoNiAl based alloys also. As for example we prepared a sample with nominal composition of $Co_{39}Ni_{34}Al_{27}$ that is annealed at 1373K for 24 h and then followed by1473

K for 72 h and water-quenched. We determined the chemical compositions in each area separately, to estimate the phase amounts and they are shown in table 4.2. It is interesting to note that the effect of annealing was to affect the chemical composition of β phase less markedly than that of the γ phase. It is seen that in the γ phase the amount of Ni remained practically constant, while there seem to be a lot of migration of the other two atomic species. This seems to have been observed before also [42]. The overall effect was to reduce the e/a ratio by only a tiny amount, but that profoundly changes the structural transformation temperatures, as shown later.

Table 4.2: Phase equilibria between β and γ phase and electron concentration in $Co_{39}Ni_{34}Al_{27}$

Temperature (K) of heat treatment	β (at%)		γ (at%)		e/a (at.%)
	Co	Al	Co	Al	
1373K/24h	32.26	33.8	51.09	19.17	7.5
1473K/72h	34.85	33.31	47.34	23.40	7.4

4.1.2. Resistivity:

The low temperature resistivity of $Co_{39}Ni_{34}Al_{27}$ was measured in an Oxford Instruments (T_M) closed cycle refrigerator using an a.c. excitation at 111.11 Hz and the temperature sweep was performed at 1 K/min for both heating and cooling cycles in between 4K to 300K temperature range. Temperature variations of resistivity (ρ) of alloys annealed at 1373K for 24h and 1473K for 72h are shown in Fig. 4.3 (a-b) for both heating and cooling cycles. The austenite to martensite transition is evident in both annealing conditions along with hysteresis between heating and cooling cycles as expected for this transition. The austenite start (T_{A_s}) and finish (T_{A_f}) and martensite start (T_{M_s}) and finish (T_{M_f}) temperatures are extracted conventionally from the breaks in the smooth background curve. Evidently, the post annealing at higher temperature increased the temperature difference between (T_{A_s}) and (T_{A_f}) and finish temperatures as well as the temperature difference between (T_{M_s}) and (T_{M_f}). Such observations have also been made earlier in one FSMA system [82].

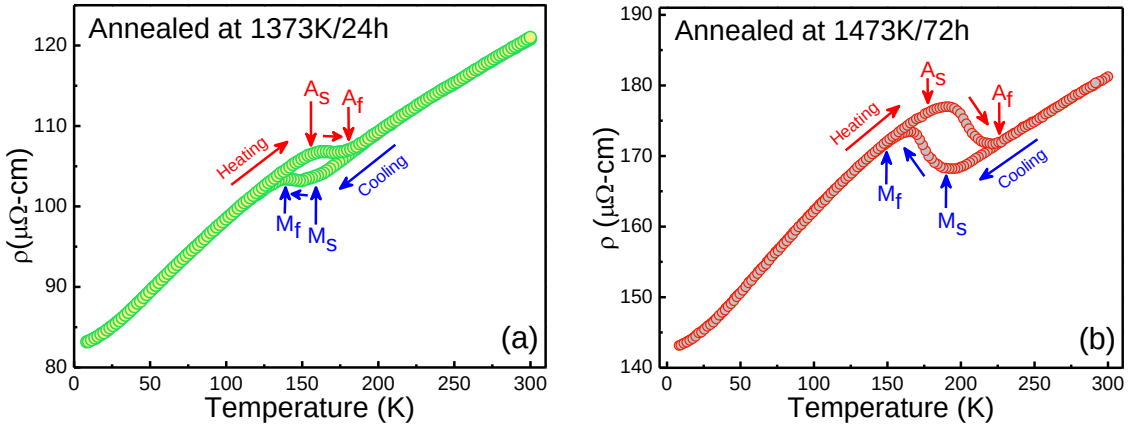

Figure 4.3: Temperature dependence of resistivity of $Co_{39}Ni_{34}Al_{27}$ alloys annealed at (a) 1373 K and (b) post annealed at 1473 K. The blue arrows indicate the Austenite start (A_s) and finish (A_f) and Martensite start (M_s) and finish (M_f) temperatures. Grey arrows indicate the direction of temperature change during resistivity measurements.

As the annealing temperature was increased, the γ phase fraction also increased, thus hindering the transformation of austenite to martensite phase transition and vice-versa resulting in prolonged transformation temperature regions [26]. The increase in γ phase fraction also causes increased disorder and consequently, increased electron scattering which is also evident from the higher value of resistivity for the alloy sample post-annealed at 1473 K compared to the one annealed at 1373 K. Because of annealing at higher temperature, local composition of β and γ phases also changed due to increased atom migration and consequently, e/a ratio also changes [26] resulting in the shift of structural transition at higher temperatures. The structural transition temperatures are given in table 4.3.

Table 4.3: Structural transition temperatures and thermal hysteresis obtained from ρ vs T curve.

Sample	T_{M_s} (K)	T_{M_f} (K)	T_{A_s} (K)	T_{A_f} (K)	T_M (K)	ΔT(K) $\left(T_{M_s} - T_{M_f}\right)$	ρ (Ωm) at 300K
1373K/24h	156	136	160	181	146	20	1.2×10^{-6}
1473K/72h	202	147	191	223	174.5	55	1.8×10^{-6}

To explore the effect of annealing in the low temperature behaviour, electrical resistivity of $Co_{39}Ni_{34}Al_{27}$ was analyzed. We have considered the contributions in resistivity, the total resistivity $\rho_{tot} = \rho_o + \rho_{ph} + \rho_{mag}$ where ρ_o is the temperature independent part of the resistivity due to the presence of defects and disorder in the system, ρ_{ph} and ρ_{mag} are the resistivity components arising out of electron-phonon and

electron-magnon scattering respectively. For 3*d* transition metals and alloys, in the higher temperature limit ρ_{ph} is given by Bloch-Wilson formula

$$\rho_{ph} = A_{ph}\left(\frac{T}{\theta_D}\right)^3 \int_0^{\frac{\theta_D}{T}} \frac{x^3 dx}{(e^x - 1)(1 - e^{-x})} \qquad [4.1]$$

where θ_D is the Debye temperature. The low temperature magnetic phase of most FSMA materials are either ferromagnetic or spin glass [83]. For a ferromagnetic system, the temperature variation of electron-magnon scattering induced resistivity has T^2 dependence whereas spin glass systems show $T^{3/2}$ temperature dependence [83, 84]. So the composite behaviour can be written as,

$$\rho(T) = \rho_o + A_{mag}^{FM} T^2 + A_{mag}^{sg} T^{3/2} \qquad [4.2]$$

where the fits will determine which one of the two interactions is present [84]. Therefore, analysis of the low temperature resistivity of alloys will give information about the possible low temperature magnetic phases and whether post-annealing at higher temperatures changed the nature of low temperature magnetic phase. We found that low temperature resistivity of alloys, for both the samples annealed at 1373 K and post-annealed at 1473 K, follow $T^{3/2}$ temperature dependence (shown in Figs. 4.4(a) – (d)) for T < 25 K.

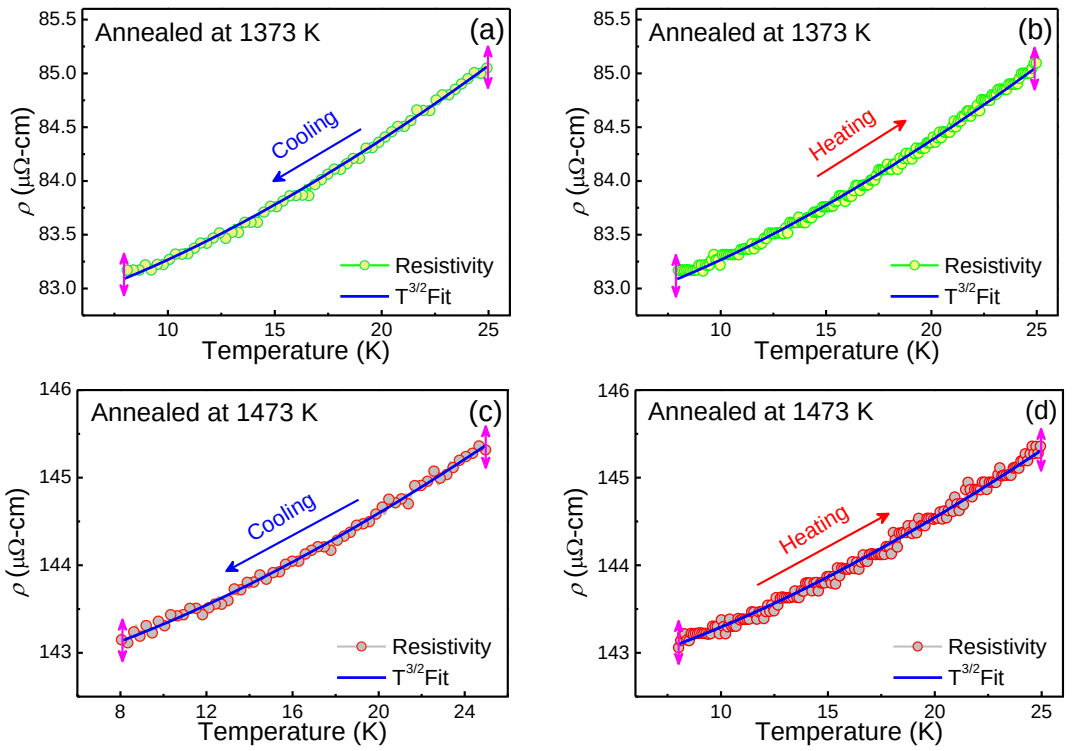

Figure 4.4: $T^{3/2}$ temperature dependence of low temperature resistivity of $Co_{39}Ni_{34}Al_{27}$ alloys annealed at (a), (b) 1373 K and (c), (d) post-annealed at 1473 K.

This indicates that the system has a low temperature glassy magnetic phase and annealing at higher temperature does not considerably affect the low temperature magnetic phase. This is consistent with similar findings in other FSMA alloys like $Mn_2Ni_{1.6}Sn_{0.4}$ [85], NiMnAl [86, 87] and is a new finding in Co-Ni-Al system. As temperature increases, the electron-phonon scattering induced resistivity ρ_{ph} becomes the dominant contribution. For 30 K < T <100 K, the fit of resistivity considering only ρ_{ph} is shown in Figs. 4.5 (a-b). The obtained Debye temperatures θ_D from the fits are 143 K and 171 K for the samples annealed at 1373 K and post-annealed at 1473 K, respectively and shown in table 4.4.

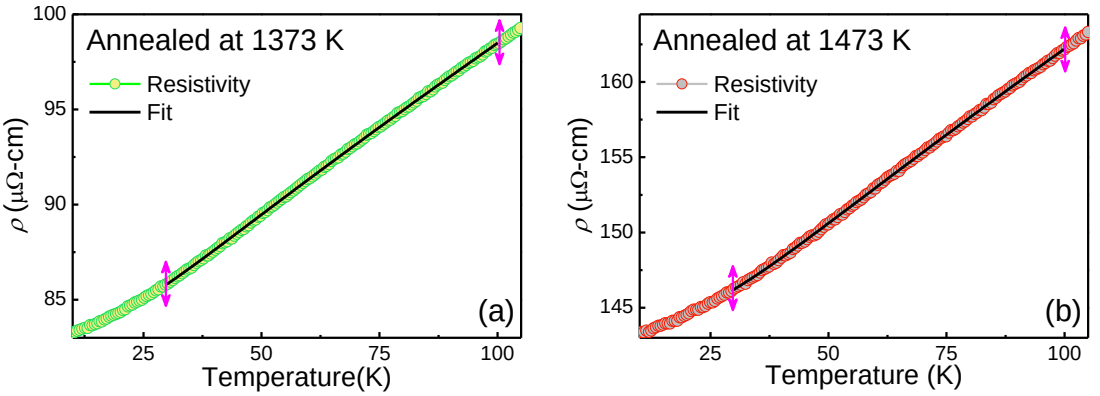

Figure 4.5: Fitting of resistivity of $Co_{39}Ni_{34}Al_{27}$ alloys annealed at (a) 1373 K and (b) post-annealed at 1473 K with electron-phonon scattering induced resistivity ρ_{ph} given by Bloch-Wilson formula.

Table 4.4: Magnetic and phonon contributions obtained from the fitting of resistivity data of $Co_{39}Ni_{34}Al_{27}$ alloys; parameters ρ_o and A_{mag}^{sg} obtained below 25 K with $T^{3/2}$ fitting. ρ'_o, A_{Ph} and Debye temperature θ_D obtained from the fitting of resistivity data of $Co_{39}Ni_{34}Al_{27}$ with Bloch-Wilson formula.

Annealing temperature (K)	$\rho(T) = \rho_o + A_{mag}^{sg} T^{3/2}$		$\rho(T) = \rho'_0 + A_{ph}\left(\frac{T}{\theta_D}\right)^3 \int_0^{\frac{\theta_D}{T}} \frac{x^3}{(e^x-1)(1-e^{-x})}$		
	ρ_o (μΩ-cm)	A_{mag}^{sg} (μΩ-cm/K$^{3/2}$)	ρ'_0 (μΩ-cm)	A_{ph} (μΩ-cm/K^3)	θ_D(K)
1373K/24h	82.66	0.019	83.5	46.5	143
1473/72h	142.6	0.022	143.9	70.6	171

The increase in θ_D value with increasing annealing temperature is due to γ phase fraction at the cost of β one is the consistent with the previous findings that increase in gamma brings in more mechanical strength in the system. The values of ρ_o obtained from the fits are 83 μΩ-cm and 144 μΩ-cm for the samples annealed at 1373 K and post-annealed at 1473 K, respectively. The increased value of ρ_0 with increasing annealing temperature indicates the increased disorder in the system, which arises from the increase of γ phase fraction with increase in annealing temperature.

4.1.3. DC Magnetization:

Temperature variations of FC and ZFC magnetizations in a magnetic field of H = 150 Oe for both the samples annealed at 1373 K and post-annealed at 1473 K are shown in Fig. 4.6 (a-b). Preceding the austenite–martensite transition, a ferromagnetic to ferromagnetic transition appears in the austenite phase marked by T_C^A in Fig. 4.6 (a) and 4.6 (b) in both the alloys as the temperature decreases from room temperature [88]. We call them ferromagnetic low (FL) and ferromagnetic high (FH) phases. This type of behavior is commonly encountered in these systems, for example, see ref. [42, 82].

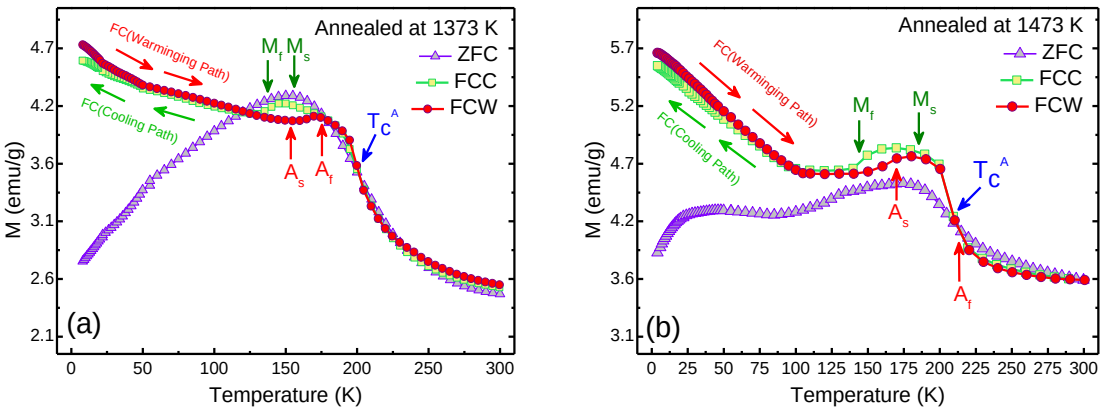

Figure 4.6: Temperature variations of ZFC, FCC and FCW magnetizations measured at H = 150 Oe of $Co_{39}Ni_{34}Al_{27}$ alloys annealed at (a) 1373 K and (b) post-annealed at 1473 K. Arrows show the transition temperatures obtained from resistivity data.

The inter-ferromagnetic Curie temperature increased on post annealing in a higher temperature (1473K) and increased from 200K to 208K. The FC curves, which were taken in both cooling and heating modes showed no hysteresis. These true thermodynamic curves show that the systems were in ferromagnetic phases; however, the ferromagnetic low (FL) phase is a complicated one. Indeed, the bifurcation seems to start from just after T_C. The general nature of low-temperature behavior of ZFC is similar in both the cases; that is, after a small peak, there is a continuous fall in magnetization until lowest temperature but after displaying a plateau in the mid-temperature range. The plateau is not very conspicuous in the 1373 K sample but is quite broad for the other case, reflecting the change in microstructure between them.

Following the explanation given for Ni_2MnGa type systems [86] this means that there is a low-temperature disordered phase (spin glass) in these systems, swamped by the remnants of ferromagnetic phase. This comes out in zero- or low-magnetic field experiments, like resistivity or ZFC, but masked under a higher magnetic field applied at FC protocol, or during M-H measurements. This is corroborated from low-temperature resistivity too; the lowest temperature resistivity has a very low coefficient (i.e., interaction strength) showing that the contribution is quite weak, as are shown in Table 4.4. Similarly, Fig. 4.7 shows that under high magnetic field, the systems remain indistinguishable from a pure ferromagnet, and the break in Hc curve below 180 K signals FC and FH phase differences. The increase of H_C may be signaling a possible exchange bias effect developing at further low temperature. However, with some problem in squid system further low temperature M-H study was not possible.

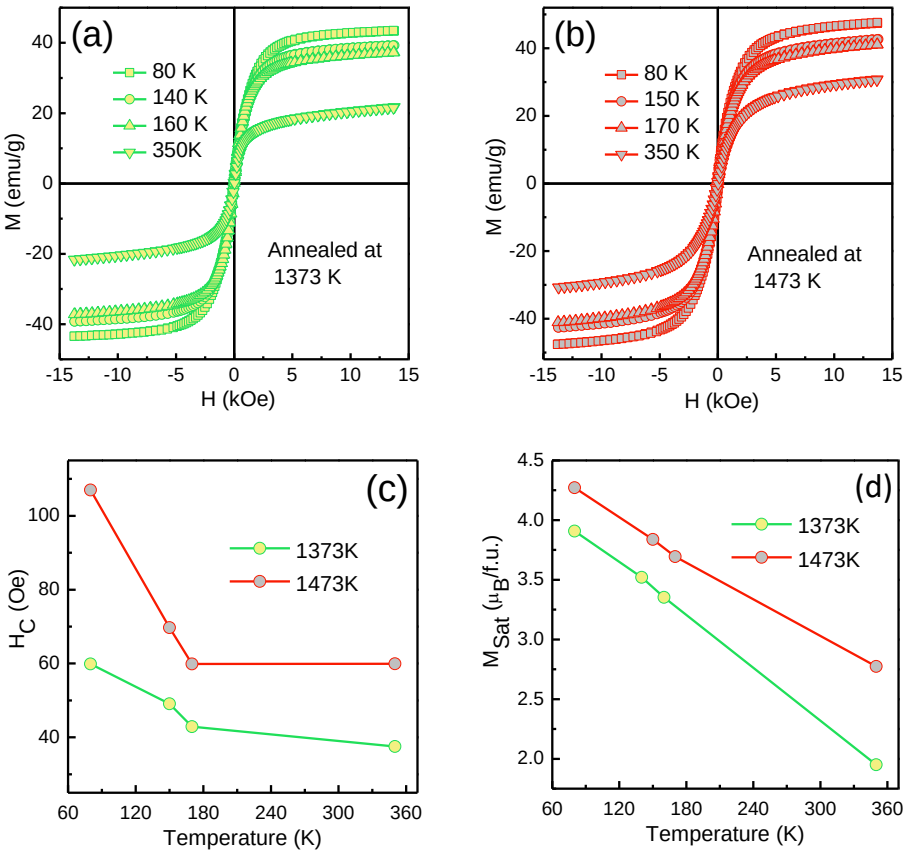

Figure 4.7: Isothermal magnetizations (M-H) of $Co_{39}Ni_{34}Al_{27}$ alloys annealed at 1373 K and post-annealed at 1473 K. Variations of (c) coercivity and (d) saturation magnetization of $Co_{39}Ni_{34}Al_{27}$ alloys with temperature.

4.1.4. AC Susceptibility:

Susceptibility measurements were performed on the $Co_{39}Ni_{34}Al_{27}$ annealed at 1473K for 72h from 300 K to 110 K at a frequency of 111 Hz for both heating and cooling cycle and the data of ac susceptibility are shown in the Fig. 4.8. The real part (χ') of ac susceptibility are shown in Fig. 4.8 (a) and the imaginary part (χ'') in Fig. 4.8 (b). Both χ' and χ'' showed peak near M_s while cooling and heating, and breaks in the curves near the structural transformation. Since from M-T graph Fig. 4.6 we know that there are two types of FM system in the sample, the characteristic as shaped χ curves is not found here. We need to use M-T curves to estimating T_C^A (found at 210K)

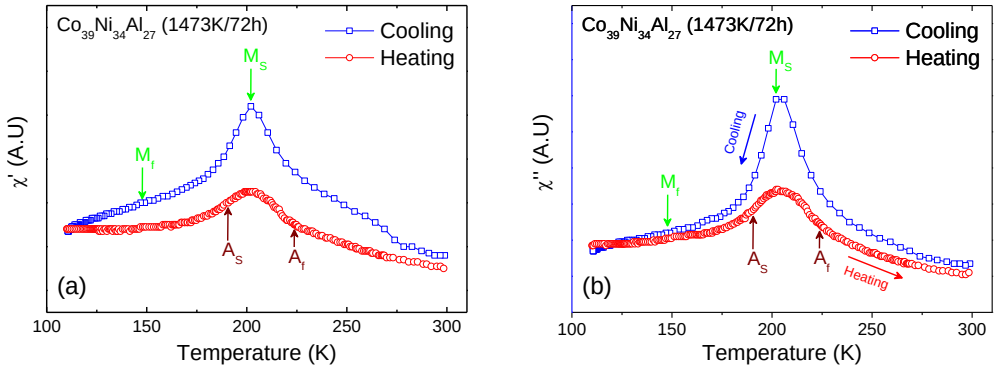

Figure 4.8: The real part of AC susceptibility in heating and cooling cycle at the frequency of 111Hz for $Co_{39}Ni_{34}Al_{27}$ (a) Real part and (b) imaginary part.

4.1.5. Sound velocity and Internal friction:

Sound velocity $\left(\frac{\delta V}{V}\right)$ and internal friction (Q^{-1}) measurements were done on reed-shaped samples, about 12 mm long, 2.8 mm wide and 600 μm thick with the vibrating reed technique as before. The effect of annealing on $\left(\frac{\delta V}{V}\right)$ and (Q^{-1}) is also drastic. Fig. 4.9 (a) shows the sound velocity changes in the two samples.

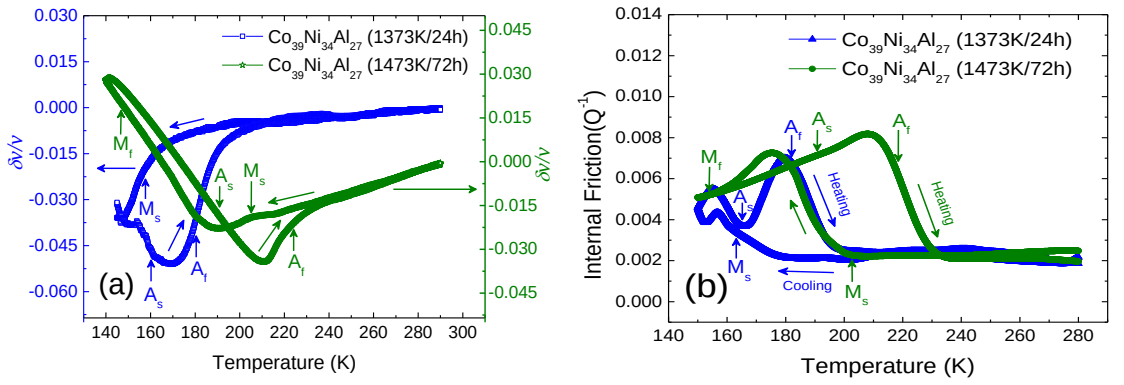

Figure 4.9: (a) SV $\left(\frac{\delta v}{v}\right)$ and (b) internal friction (Q^{-1}) of CoNiAl FSMA for low temperature cycle.

The heating and cooling curves show remarkable elastic property changes near the transformations. The velocity in the austenite phase initially decreased from room temperature values; this seems to be the general trend of the FSMA materials. We found this previously also [47, 89]. However, below T_{Ms} the elastic property was regained at a marked pace. On heating up the sample when it was deep inside the martensite phase, the system became softer until T_{As} was reached and then the elastic recovery occurred until T_{Af} when the original value was reached. The two samples behaved nearly identically; however, due to limitation of the present setup, we could not go deeper into the martensite phases to fully see the nature of elasticity there in both the cases. Nevertheless, the recovery effect was still about the same. In case of attenuation, the behaviour was even more drastic (Fig. 4.9 b). In case of the as-prepared sample, two of the transformations-martensitic start and austenite end points-can be clearly seen. The sample had a higher value of Q^{-1} initially that rose about 4 times during the state change. It was falling to a low value, but we could not take the measurements to a lower temperature due to limitations in the used setup. The same jump in Q^{-1} was also seen during heating up. The previous low value was also regained once the transition was over. In case of the other sample, similar behaviour at lower temperature was seen, but because the transition temperatures are now on the higher side, all of them can now be seen. One important observation is that although the changes in $\delta v/v$ decreased by about 1.5 times (0 to -0.034 vs. 0 to -0.051) during the structural transitions between the two samples (when compared to the same reference values at 300 K), the values of Q^{-1} were far less affected in a similar situation.

Continuing on the analysis of the $(\delta v/v)$, i.e. the real part of E, as was done before in Chapter-3 we bifurcate two different regions for elasticity that are before and after the transition starts and ends shown in Fig. 4.7 (a). These correspond to pure austenite and martensite regions. Assuming the similar contributions and with the Debye type model as discussed before we fitted $\delta v/v$ in those region and resultant curves are shown in Fig. 4.10 (a-d).

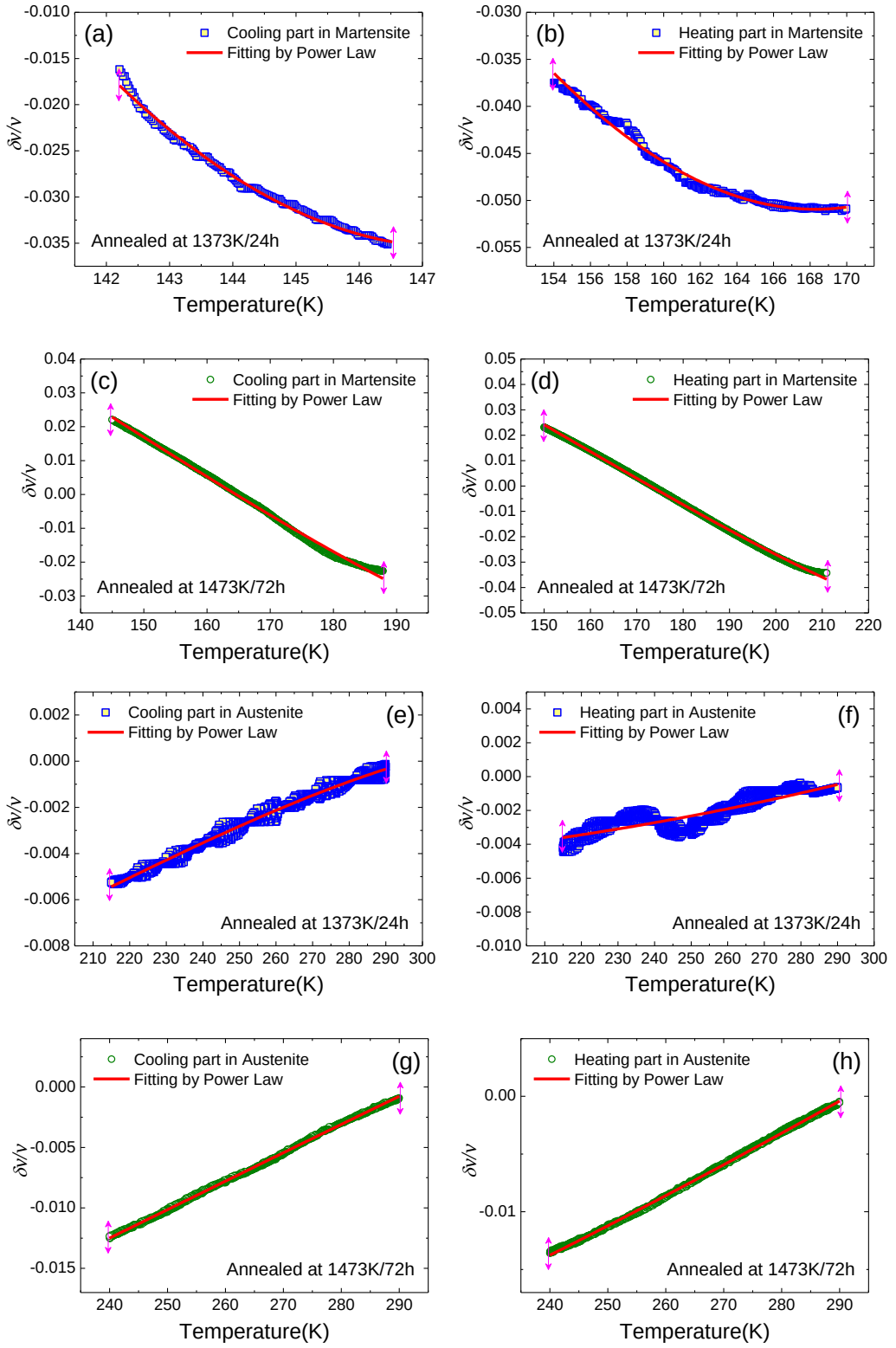

Figure 4.10: (a and b) Elastic contributions to cooling and heating cycles for 1373K/24h sample, below T_{Mf}; (c and d) show the same for the 1473K/72h sample; (e and f) show elastic contributions to cooling and heating cycles of the 1373K/24h sample, above T_{Af}; (g and h) show the same for the 1473K/72h sample.

Table 4.5: variation of different contributions with the crystal structure calculated by power law fitting, B and C express from electronic contribution and lattice contribution respectively in $Co_{39}Ni_{34}Al_{27}$

Annealing Temp.	Cycle	Martensite region				Austenite region			
		Temp. Range (K)	A	B	C	Temp. Range (K)	A	B	C
1373K For 24h	Cooling	142-146	1.61	-1.5×10^{-4}	3.2×10^{-9}	215-290	-0.02	2.9×10^{-7}	-1.2×10^{-12}
	Heating	154-170	0.49	-3.9×10^{-5}	6.8×10^{-10}	215-290	-0.01	5.6×10^{-8}	2.0×10^{-13}
1473K For 72h	Cooling	145-188	0.13	-6.2×10^{-6}	5.1×10^{-11}	240-290	-0.02	6.8×10^{-7}	-1.7×10^{-12}
	Heating	150-211	0.12	-5.1×10^{-6}	3.4×10^{-11}	240-290	-0.02	6.1×10^{-7}	-7.5×10^{-13}

One can see that while the electronic contribution has decreased in the heating parts, similar changes were higher for the lattice part. The reason for this type of difference comes from the different rates at which the transformations were approached or departed because of some difference in the cooling and heating rates (and these transitions are quite dependent on the rates) in the present setup. Next important observation is that the values of *B* and *C* are much higher in case of lower annealed sample (1373 K/24 h) than the corresponding ones in the other one. Final noteworthy point is that the changes in *B* and *C* for the lower temperature annealed sample are more (~ 4-6 times) than those annealed at higher temperature (~ 1.1-2.3 times only). Taken together with the shifts in structural transition temperatures, these all indicate the profound nature of annealing that was brought in due to enhanced annealing. As stated before, the microstructural and chemical composition changes are the root causes for these effects.

4.1.6. Stress and magnetic field induced Sound velocity and IF (Q^{-1})*:*

The composition $Co_{39}Ni_{34}Al_{27}$ annealed at 1473K/72h being a good FSMA combines the 84% of volume fraction of β phase with and 16% of γ phase. Hence, we are motivated to study the stress induced $\delta v/v$ and Q^{-1} as well as in a uniform magnetic field also. The stress depends on the square of the square of impressed drive signal, and can be calculated from the amplitude of drive and geometrical factors of sample geometry and electrode-samle distance. We choose four convenient drive voltages and calculated the associated stress.

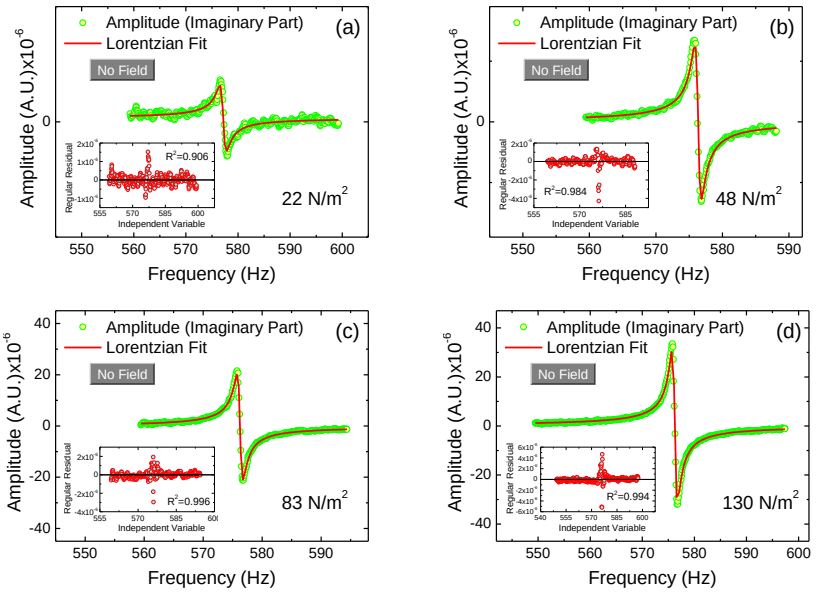

Figure 4.11: Imaginary parts of single resonance for the reed where the width of resonance Δf and resonance frequency f_c obtained by Lorentzian fitting and $Q^{-1} = \Delta f / f$

Table 4.6: Stress Dependent Q^{-1} in $Co_{39}Ni_{34}Al_{27}$ at room Temperature

Stress (N/m^2)	Q^{-1}
22	0.00211
48	0.00167
83	0.00166
130	0.00164

We determined the room temperature Q^{-1} without presence of magnetic field but under those four stresses, following the same procedure as discussed in Sec. 2.7.1. The fitting of the imaginary part of single resonance for a reed shown in Fig. 4.11 (a-d) and Q^{-1} calculated from the fitting are given in table. 4.6. it is interesting to find that the lowest stress gave higher Q^{-1} than the higher hysteresis. It can be rationalized by assuming the higher stress values have bought the grains in some forms of alignment and so reduced the grain misorientation loss.

The stress dependent temperature variations of $\delta v/v$ and Q^{-1} are shown in Fig. 4.12. The trend is almost same as discussed before. From lower to higher level of stress there is structural recovery during heating except there is a shift of austenitic start temperature (T_{As}) to the higher side as stress is lowered. The transition temperature is put in the table 4.7.

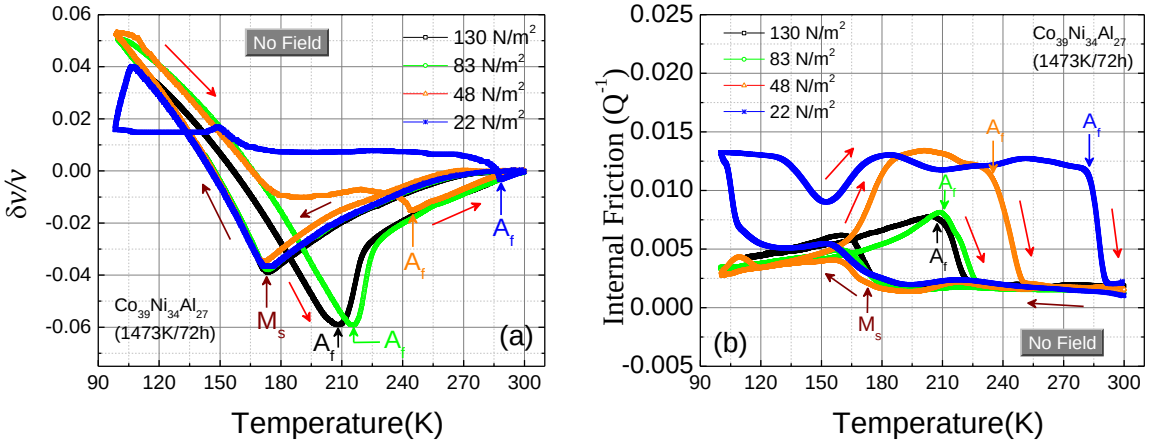

Figure: 4.12: SV $(\delta v/v)$ and Internal friction (Q^{-1}) in $Co_{39}Ni_{34}Al_{27}$ for different applied stresses.

Table 4.7: The transition temperature T_{Ms} and T_{As} evaluated from the $\delta v/v$ vs T graph.

Stress	$T_{M_s}\ (K)$	$T_f\ \ (K)$	$\Delta T\ (K)\ \left(T_{M_s} - T_{A_f}\right)$
130	173	208	35
83	173	215	42
48	172	244	72
22	171	288	117

From the sound velocity changes it is seen that the martensitic start temperature T_{Ms} are less effected by the applied stress during cooling. But in the heating path the Austenitic temperature T_{As} is highly effected by stress. However, below T_{Ms} the elastic property was regained at a marked pace. On heating up the sample when it was deep inside the martensite phase, the system became softer until T_{As} was reached and then the elastic recovery occurred until T_{Af} when the original value was reached. All the samples behaved nearly identically. In case of attenuation, interesting behaviour was seen (Fig. 4.12b). During martensiting transition almost same jump is found as before for all the applied stresses. But while heating the recovery is even more drastic. In case of lower stress the sample had a higher value of Q^{-1} during the state change. It was falling to a lower value as the stress increased. The behaviour of the $\delta v/v$ as the stress increased was to decrease the A_f monotonically, along with making the sample softer in the initial phase, from the lowest temperature. The other transition temperatures are not so markly changed these values are given in table 4.7. in case of Q^{-1}, the effect of strain was equally drastic, while the lowest stress gave more Q^{-1} and a large thermal hysteresis loop. The loss kept on decreasing as more stress was applied. Eventfully for the higher two stresses the loop areas were quite well behaved and reasonably low.

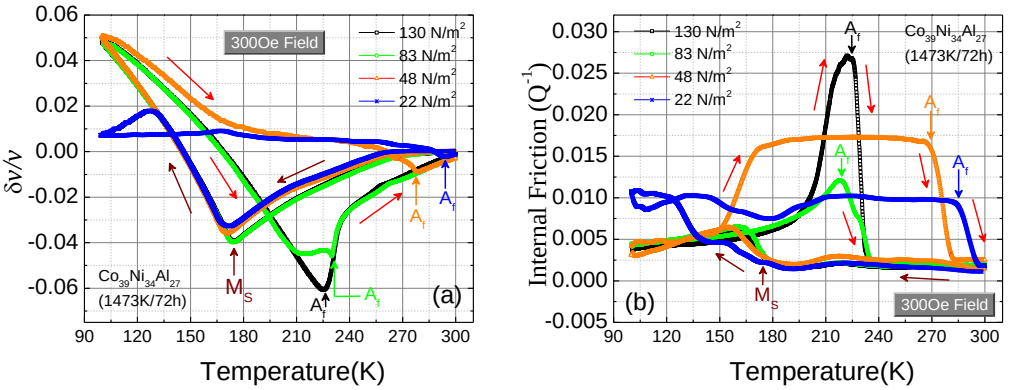

Figure: 4.13: Sound velocity ($\delta v/v$) and Internal friction (Q^{-1}) in $Co_{39}Ni_{34}Al_{27}$ for uniform 300 Oe field and different applied stresses.

Under applied magnetic field, we also see the similar trend. The $\delta v/v$ behaved except that the associated temperatures seems to have increased. These are given in table 4.7. the interesting point is that the Q^{-1} values tended to peak near T_C^A, while being heated from low temperature Martensitic phase, but while cooling down the effect was barely

noticeable. If it ought to be hysteresis effect because it depends stress level. These behaviour is currently under investigation.

Table 4.8: The transition temperature T_{Ms} and T_{As} evaluated from the $\delta v/v$ vs T graph for $H = 300Oe$

Stress	$T_{M_s}\ (K)$	$T_f\ \ (K)$	$\Delta T\ (K)\left(T_{M_s} - T_{A_f}\right)$
130	174	226	52
83	173	230	57
48	171	278	107
22	169	294	125

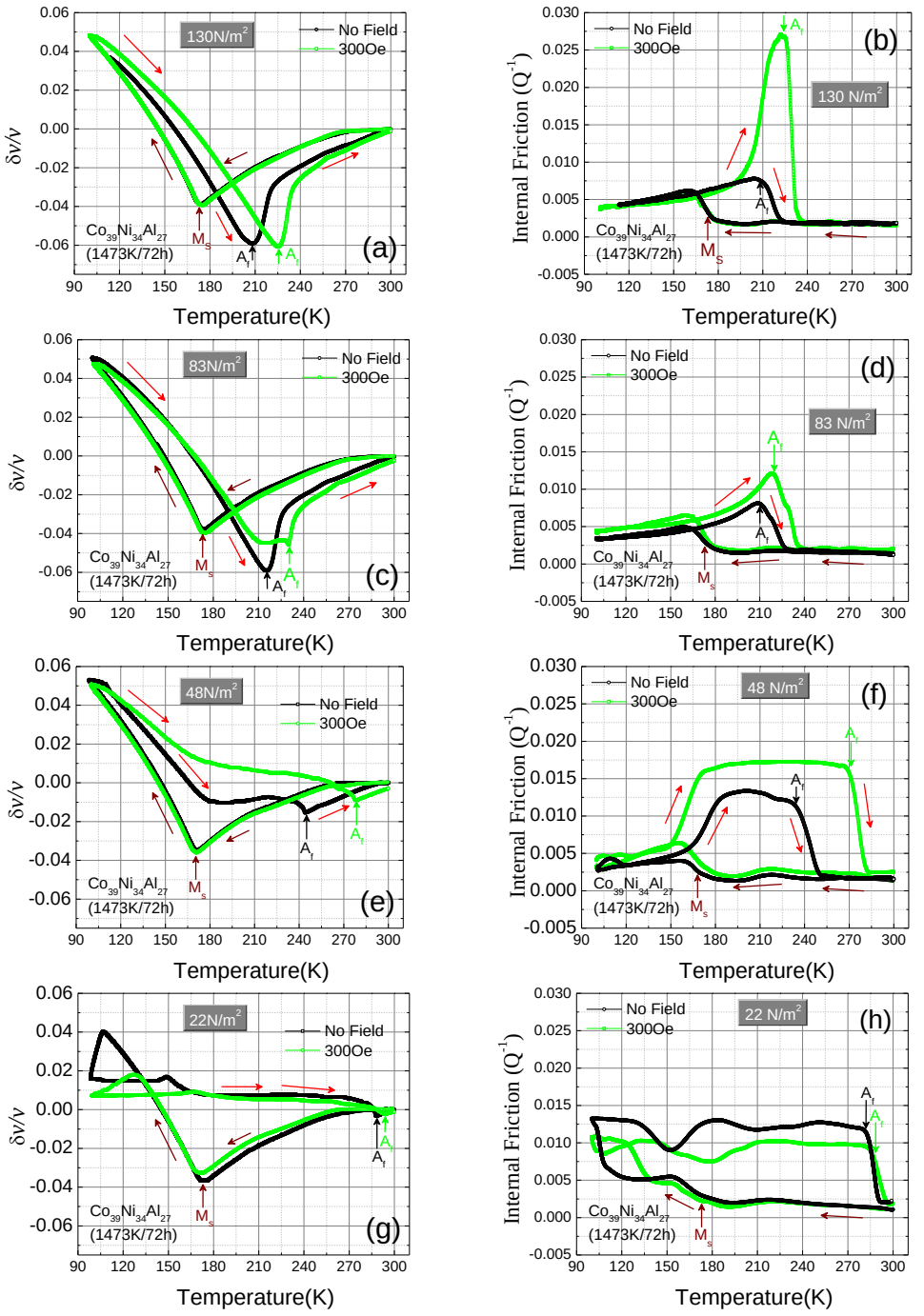

Figure: 4.14: Sound velocity $(\delta v/v)$ and Internal friction (Q^{-1}) in $Co_{39}Ni_{34}Al_{27}$ for different applied stresses compared for $H = 0Oe$ and $H = 300Oe$.

From the analysis of $\left(\frac{\delta v}{v}\right)$, i.e. the real part of E shown in Fig. 4.14 (a) two different regions are clear as before and hence we fitted the graph in the pure Austenite and Martensite region as before shown in Fig. 4.15 The contributions extracted are given in table 4.8.

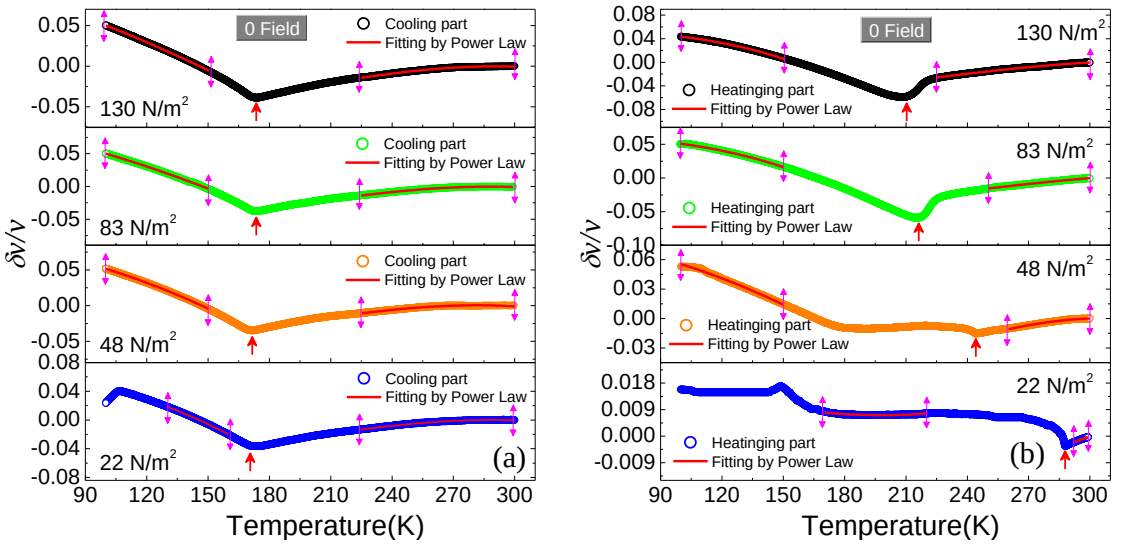

Figure 4.15: Elastic contributions (a) during cooling cycle and (b) heating cycles in $Co_{39}Ni_{34}Al_{27}$ for different applied stresses.

Table 4.9: Variation of different contributions with the crystal structure calculated by power law fitting, B and C express from electronic contribution and lattice contribution respectively in $Co_{39}Ni_{34}Al_{27}$ at different stress level.

Stress N/m^2	Cycle	Martensite region				Austenite region			
		Temp. Range (K)	A	B	C	Temp. Range (K)	A	B	C
130	Cooling	100-150	0.1	-5.5×10^{-6}	3.5×10^{-11}	225-300	-0.09	2.09×10^{-6}	-1.2×10^{-11}
	Heating	100-150	0.6	-8.6×10^{-7}	-6.6×10^{-11}	225-300	-0.09	1.7×10^{-6}	-8.1×10^{-12}
83	Cooling	100-150	0.09	-5.0×10^{-6}	2.2×10^{-11}	225-300	-0.09	2.2×10^{-6}	-1.3×10^{-11}
	Heating	100-150	0.06	-1.1×10^{-6}	-5.2×10^{-11}	225-300	-0.08	1.3×10^{-6}	-5.1×10^{-12}
48	Cooling	100-150	0.09	-4.5×10^{-6}	7.4×10^{-13}	225-300	-0.08	2.2×10^{-6}	-1.3×10^{-11}
	Heating	100-150	0.08	-3.3×10^{-6}	-5.3×10^{-13}	260-300	-0.14	3.0×10^{-6}	-1.6×10^{-11}
22	Cooling	130-160	0.08	-3.2×10^{-6}	-3.0×10^{-11}	225-300	-0.08	2.1×10^{-6}	-1.2×10^{-11}
	Heating	170-220	0.02	-6.1×10^{-7}	7.7×10^{-12}	292-300	-0.2	5.1×10^{-6}	-2.7×10^{-11}

From the fitting of the temperature dependent $\delta v/v$ as discussed before we extracted the contributions (Table. 4.10). in Fig. 4.16 the fitted graphs are shown.

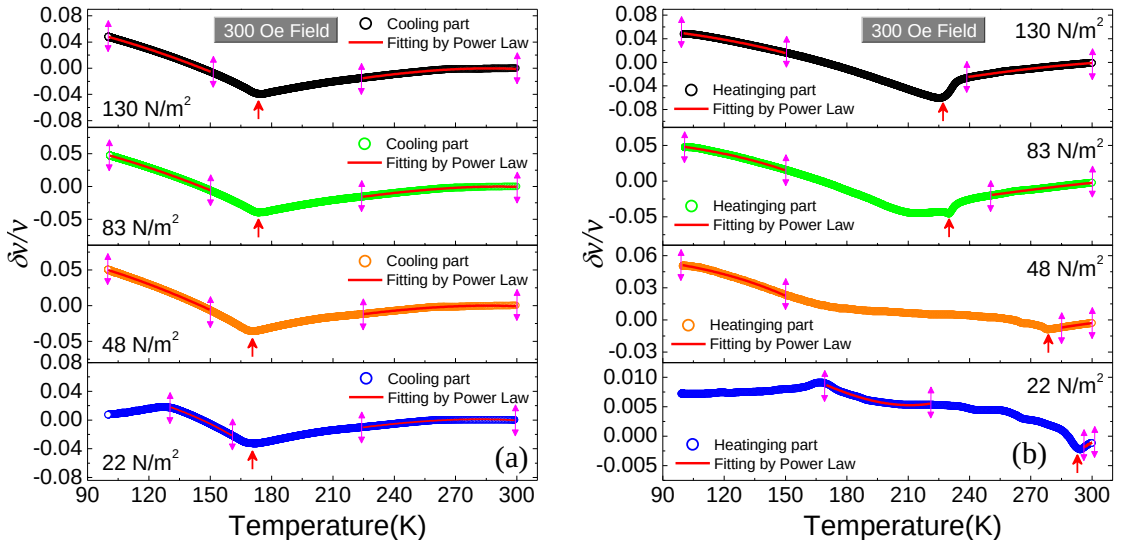

Figure 4.16: Elastic contributions (a) during cooling cycle and (b) heating cycles in $Co_{39}Ni_{34}Al_{27}$ for different applied stresses and in a uniform magnetic field of 300 Oe.

Table 4.10: Variation of different contributions with the crystal structure calculated by power law fitting, B and C express from electronic contribution and lattice contribution respectively in $Co_{39}Ni_{34}Al_{27}$ at different stress level and in uniform 300 Oe field.

Stress N/m^2	Cycle	Martensite region				Austenite region			
		Temp. Range (K)	A	B	C	Temp. Range (K)	A	B	C
130	Cooling	100-150	0.09	-4.47×10^{-6}	6.4×10^{-12}	225-300	-0.1	2.5×10^{-6}	-1.5×10^{-11}
	Heating	100-150	0.07	-1.9×10^{-6}	-2.5×10^{-11}	240-300	-0.1	2.2×10^{-6}	-1.2×10^{-13}
83	Cooling	100-150	0.09	-4.6×10^{-6}	8.6×10^{-12}	225-300	-0.09	2.2×10^{-6}	-1.3×10^{-11}
	Heating	100-150	0.06	-1.1×10^{-6}	-4.7×10^{-11}	250-300	-0.09	1.5×10^{-6}	-5.6×10^{-12}
48	Cooling	100-150	0.1	-4.7×10^{-6}	6.0×10^{-12}	225-300	-0.08	2.0×10^{-6}	-1.2×10^{-11}
	Heating	100-150	0.06	-8.0×10^{-7}	-4.5×10^{-11}	284-300	-0.11	1.9×10^{-6}	-8.5×10^{-12}
22	Cooling	130-160	0.06	-1.2×10^{-6}	-7.8×10^{-11}	225-300	-0.08	2.1×10^{-6}	-1.3×10^{-11}
	Heating	170-220	0.03	-1.3×10^{-6}	1.4×10^{-11}	295-300	-0.44	9.7×10^{-6}	-5.3×10^{-11}

The observed v contains basically two parts, a lattice part v_L and a magnetic contribution v_M and therefore the total contribution becomes as

$$\frac{\delta v(T)}{v} = \left(\frac{\delta v}{v}\right)_L + \left(\frac{\delta v}{v}\right)_M \qquad [4.3]$$

$(\delta v/v)_L$ arises from lattice anharmonicity. However, at lower temperature it contains a small electronic part, coming from electronic Grüneisen parameter. It is virtually impossible to estimate it from higher temperature data. From the data (Fig. 4.17), we can see that for T→125K, $(\delta v/v)_M \to 0$. The task is to estimate $(\delta v/v)_L$ for $T < 125K$ by extrapolation from $T > 125K$ inorder to find out $(\delta v/v)_M$. The best thing will be to give

an estimate of uncertainty. For the background estimation, apart from the power law, there is another method as suggested by Varshni [90] and found to be valid for metals and alloys (both single and polycrystals) [90 - 92] and the relation is as,

$$v(T) = v(0) - \frac{S}{e^{\frac{t}{T}} - 1} \qquad [4.4]$$

The relation is based on Einstein oscillator model of solids. Here, t is some characteristic temperature of the model and s/t is the high temperature ($T \gg t$) derivative dv/dT and $v(0)$ is the zero temperature sound velocity. Points down to $\approx 125K$ are used here to evaluate $(\delta v/v)_L$ down to 115K. The general form of the equation 8 we used for fitting the $\delta v/v$ as,

$$\frac{\delta v}{v} = A - \frac{B}{e^{\frac{C}{T}} - 1} \qquad [4.5]$$

Where A, B and C are the constants evaluated from the fitting curve. By subtracting the $(\delta v/v)_L$ from the whole $\delta v/v$ in the temperature range between 115K to 130K we estimate the $(\delta v/v)_M$. At the lower applied stress magnetic contribution goes to minimum as lowering the temperature.

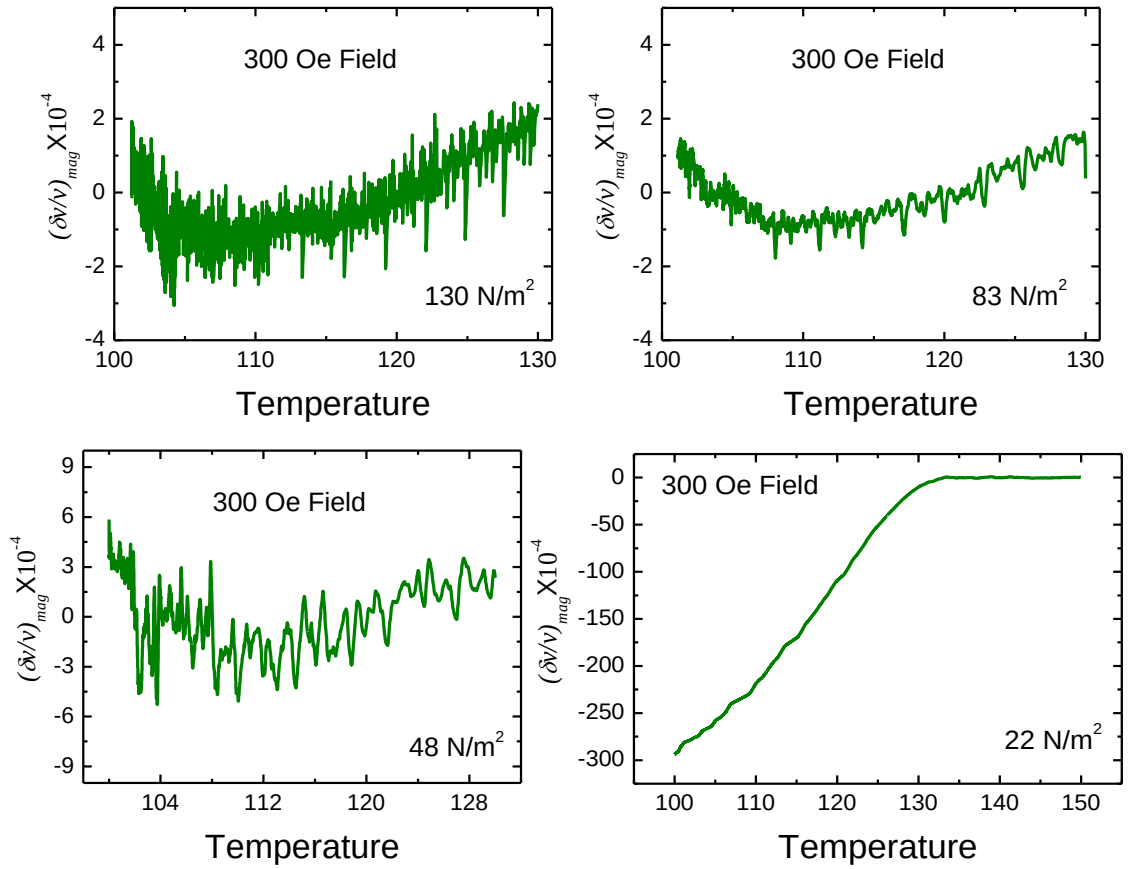

Figure 4.17: Magnetic contribution to $\delta v/v$ at low temperature for $Co_{39}Ni_{34}Al_{27}$ in presence of external magnetic field.

4.2. *Effect of Annealing on $Co_{36}Ni_{36}Al_{28}$:*

A polycrystalline ingot of Co-Ni-Al alloy with a nominal composition of 36 at.% Co, 36 at.% Ni, 28 at% Al was prepared by arc melting method in an argon atmosphere with high purity (99.9%) metals as discussed before. The ingot was cut into five pieces, from which four pieces were then vacuum sealed with argon in separate quartz ampoules. Alloy-A is the as prepared piece that is without heat treatment. Two pieces were annealed at 1273K for 72 hours followed by water quenching. Between these two pieces, one was further heat treated at 573K for 24 hours followed by slow furnace cooling. Similarly, the remaining two pieces were annealed at 1473K for 72 hours followed by water quenching, and one of them was further heat treated at 573K for 24 hours. These samples are called as Alloy-B, Alloy-C, Alloy-D and Alloy-E respectively. XRD patterns of alloys heat treated at different temperatures are shown in Fig. 4.18. Major peaks corresponded to two main phases of an ordered matrix (Co, Ni)Al with space group Pm3m of "BCC" structure (B2 or β or A for Austenite) and a disordered "FCC" cobalt rich solid solution with space group of Fm3m (γ Phase). Hence, the two phase ($\beta + \gamma$) region is found in the alloys which agrees to the reported phase diagram [42].

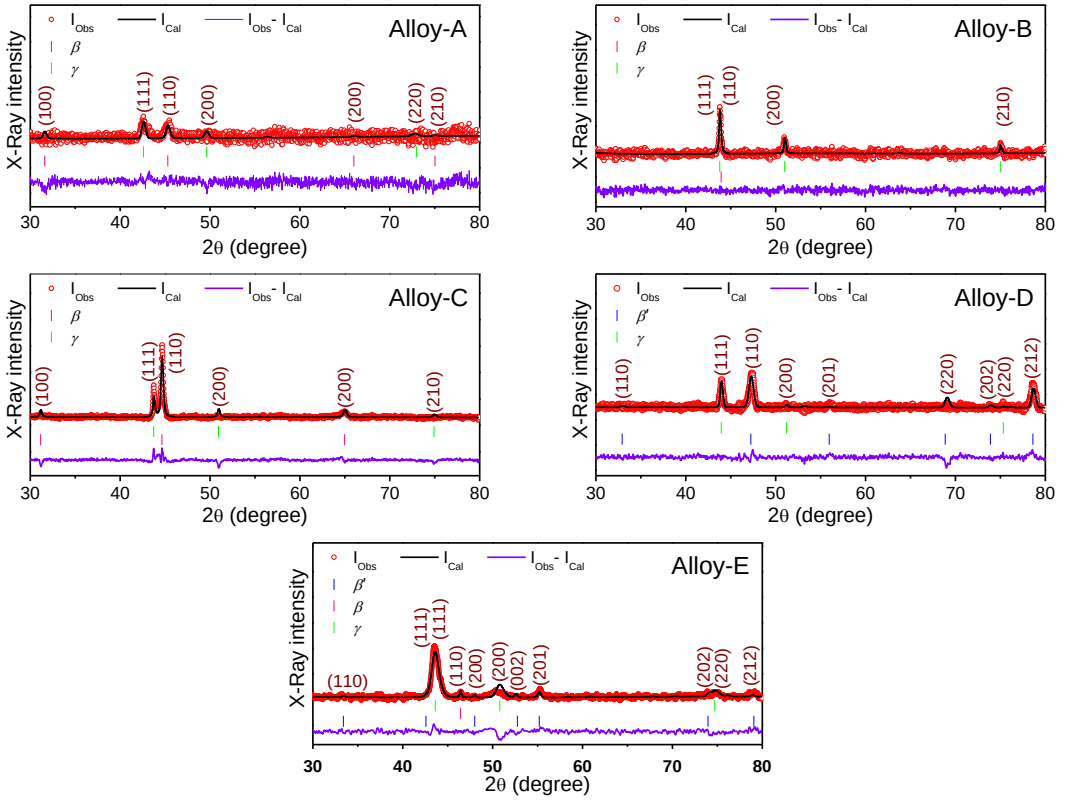

Figure 4.18: XRD patterns (I_{Obs}) of $Co_{36}Ni_{36}Al_{28}$ samples under different heat treatment conditions along with the, calculated patterns (I_{Cal}), differences between the observed patterns and calculated patterns ($I_{Obs} - I_{Cal}$) and peak positions fitted (vertical bar)

The FSMA β-phase surrounding by γ phase is responsible for the odd/even alignment of superlattice peaks of (100), (111), (110) and (200) [59]. But, the sample annealed at 1473 K/72h (Alloy-D) and the one with further heat treatment of 573 K/24h are of mixed B2 and martensitic β' (M or $L1_0$) phases, along with the usual γ precipitates. All structural parameters were obtained by Reitveld refinement [57-60] using Fullproof software and are given in Table.4.11. Amount of each phase for each sample is indicated there.

Table 4.11: XRD data analysis of $Co_{36}Ni_{36}Al_{28}$ samples for evaluating the structural parameters of the unit cell and phase fraction computation, obtained by Rietveld refinement.

Sample	Crystal Structure		Phase Fraction (%)	Cell Parameters (Å)	χ^2
	Phase	Space Group			
Alloy-A	β (B2)	Pm-3m	83.5±7.7	a = b = c = 2.81 (1)	1.33
	γ (Al)	Fm3m	16.5±1.4	a = b = c =3.64 (10)	
Alloy-B	β (B2)	Pm-3m	71.9±2.5	a = b = c =2.86 (1)	1.09
	γ (Al)	Fm3m	28.1±3.7	a = b = c =3.58 (1)	
Alloy-C	β (B2)	Pm-3m	84.4±0.4	a = b = c =2.87 (1)	1.03
	γ (Al)	Fm3m	15.6±0.4	a = b = c =3.58 (1)	
Alloy-D	β' ($L1_0$)	P4/mmm	69.8±2.0	a = b = 3.84 (5), c = 3.08 (5)	2.31
	γ (Al)	Fm3m	30.2±0.3	a = b = c = 3.56 (1)	
Alloy-E	β (B2)	Pm-3m	9.5±0.2	a = b = c = 2.83 (1)	1.8
	β' ($L1_0$)	P4/mmm	75.4±0.2	a = b = 3.79 (1), c = 3.06 (1)	
	γ (Al)	Fm3m	15.1±0.2	a = b = c = 3.68 (1)	

The SEM microstructure photographs are shown in Fig. 4.19 (a-e). Following procedures as in [26], the darker grains are assumed to be β and/or $\boldsymbol{\beta'}$ phases, therefore, the brighter regions have to be the $\boldsymbol{\gamma}$ phase.

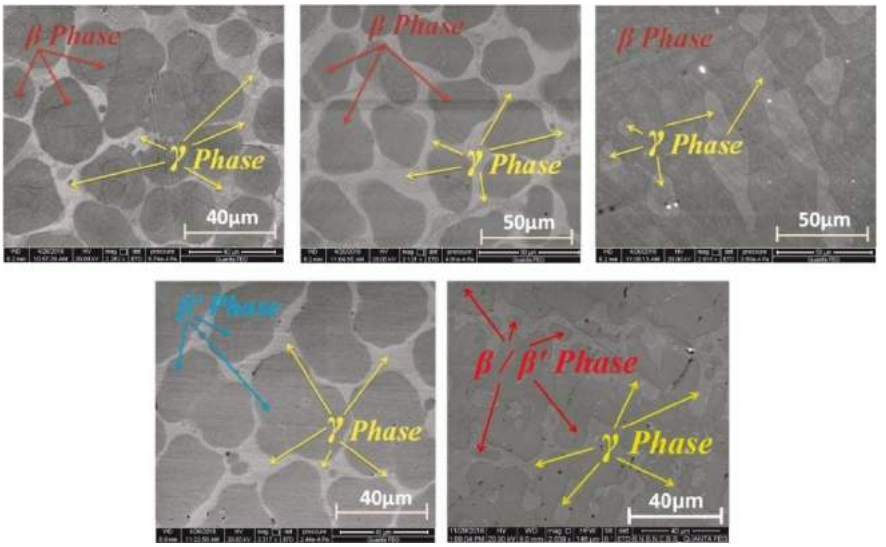

Figure 4.19: (a-e) Room temperature microstructures of samples A – E respectively.

The micrographs can be used to follow the evolution of the phases due to heat treatments. The as prepared sample, Alloy-A, seems to be a simple mixture of regular shaped β grains immersed in the sea of γ phase precipitates. Ratio of $\beta:\gamma$ phases is about 85:15%. In Fig. 4.19 (b), Alloy-B is found to have similar morphology but the intergrain separation appears to have increased. Correspondingly XRD found more γ phase in this case (about 70:30%). In one such extensive microscopy studies (TEM equipped with Energy Dispersive X-ray Spectrometer (EDS) composition analyzer (EDAX Inc.), with scanning TEM and High-angle Annular Dark-Field (STEM-HAADF) imaging and spectrum-image elemental-mapping capabilities) in similar type of Co-Ni-Al systems [93], it was demonstrated that at elevated temperatures, some Co atoms migrated to the γ region, making it Co rich and the Ni-Al region (β phase) shrunk due to this. The grains are sparsely distributed therefore. However, after annealing in 573K for sometime the Co atoms returned to the β phase, but being a diffusion based process, it is so random in nature (Fig. 4.19 c). The shapes of the grains are hence arbitrary, but the final stable ratio of about 84:16% is regained. Similar sequence of effects occurred while the sample was taken to a higher temperature, as shown in Fig. 4.19 (d). The ratio of $\beta':\gamma$ is again reduced to about 70:30%. This β' phase is a higher temperature phase of β, has the same composition but with a different crystal structure [42]. Due to rapid quenching, the high temperature structure is preserved here, including the grain morphology and phase ratio. From the phase diagram study of such systems [42], it is already known that minor composition variation can make β phase more stable at lower temperatures and the β' phase is a higher temperature. So on annealing at a lower temperature, the low temperature stable β phase started to form, most of the Co atoms from γ phase went back to the β (orβ') phase, and the β' phase also started transforming to the β phase, by Martensitic transformation. Due to the short time exposure, the transformation was not completed. This is shown in Fig. 4.19 (e), here the dark regions are identified to be β and β' phases and cover most of the sample, while the brighter patches are γ phase. Since the first two phases are chemically the same, only differing in the crystal structures, SEM is unable to distinguish between them. The important point is that the ratio of 84:16% is achieved here too, although all these transformations made the system most random. Indeed it is evident that the micrographs in Fig. 4.18 (c) and 4.19 (e) are rather similar, due to the regeneration of β phase, whereas the morphologies in Figs. 4.19 (a), 4.19 (b) and 4.19 (d) are similar to themselves.

4.2.1. Resistivity:

Four probe electrical resistivity measurements were done by a standard four probe resistivity measurement method with a.c. excitation (111.11 Hz) between 100 and 350K.

This temperature range encompasses the range of phase transition temperature for Co-Ni-Al alloy [26, 27]. The results of resistivity measurements are shown in Fig.4.19. During heating, the material, initially in a thermally-induced martensitic state (M), changes into a two-phased state (i.e. M and A) and ends up in a pure austenitic state (A). The results show that the Martensite start (M_S), Martensite finish (M_f), Austenite start (A_S) and Austenite finish (A_f) temperatures of system increases, depend critically upon the heat treatment of the sample and have variations from 209 to 340K and 203 to 319K, respectively. Another important point is that the resistivity continuously increased as more and more heat treatment was given indicating that more disorder was getting introduced in the process. Evidently different heat treatments were affecting the shapes, sizes, crystal structures etc. of the grains, thereby increasing the number of scattering surfaces for electrons.

It is further seen that while the heat treatment sharpened the A-M transitions as compared to the as prepared sample, subsequent heat treatments actually made it worse. In case of higher temperature anneal (1473K), the A-M transition shifted to above room temperature as shown in table 4.12. The cause can be ascribed to the enhancement of $\boldsymbol{\beta}'$ phase. However, $\boldsymbol{\beta}'$ phase is a relatively unstable phase and so on further lower temperature annealing (573K) partially recovered to more stable β phase. This opened up the A-M loop, in an attempt to bring it to normal $\beta - \gamma$ two phase structure system. The transition temperatures are deduced from break in the resistivity curves and are marked in the graph and given in the table 4.12.

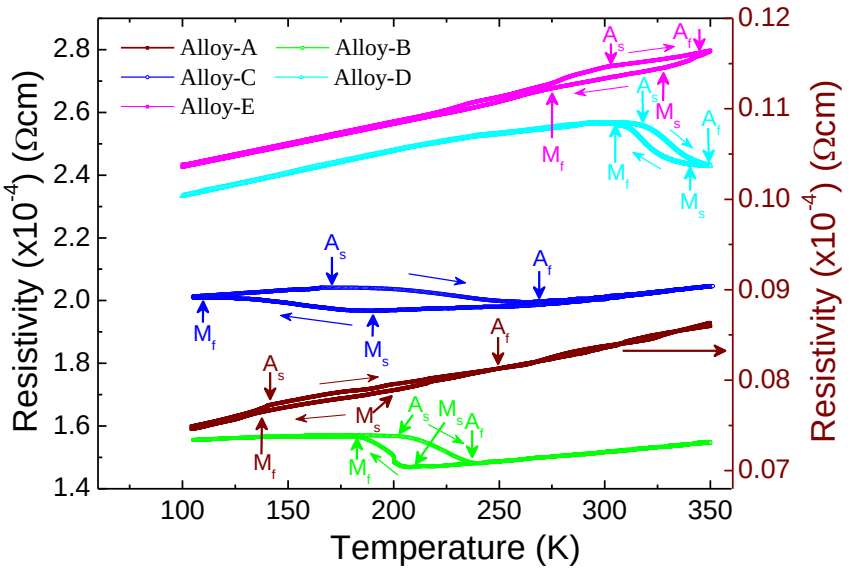

Figure 4.20: Resistivity (ρ) vs temperature of various samples. The arrows mark the transition temperatures. Data for only Alloy-A corresponds to the right side.

Table 4.12: Martensitic start (T_{Ms}), Martensitic finish (T_{Mf}), Austenic start (T_{As}), austenitic finish (T_{Af}) temperatures and $\Delta\rho_A^{M^T}$ is difference between resistivities of Martensite and Austenite state.

Samples	T_{MS} (K)	T_{MF} (K)	T_{AS} (K)	T_{AF} (K)	T_M (K)	$\Delta\rho_A^{M^T}$ (Ωcm)
Alloy-A	200	136	141	249	168.0	6.2×10^{-8}
Alloy-B	209	183	203	236	196.0	9.3×10^{-6}
Alloy-C	190	109	171	269	149.5	8.7×10^{-6}
Alloy-D	340	304	319	349	322.0	1.11×10^{-5}
Alloy-E	326	276	303	343	301.0	3.24×10^{-6}

4.2.2. DC Magnetization:

Magnetization measured between 80K and 400K by using a Lake Shore® vibrating sample magnetometer, at a field strength of 150 Oe, is shown in Fig. 4.21. It shows equally clearly remarkable changes brought about due to different annealing conditions.

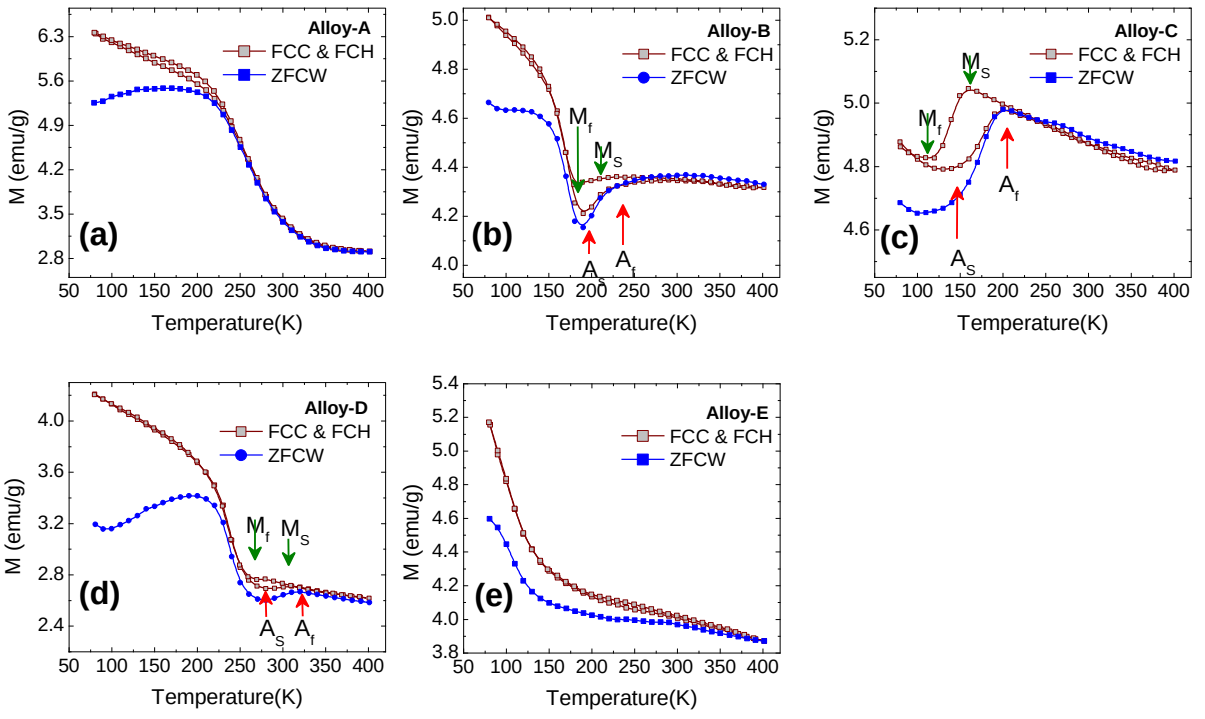

Figure 4.21: ZFC and FC M vs T plots for under field of 150 Oe for (a) Alloy-A, (b) Alloy-B, (c) Alloy-C, (d) Alloy-D, and (e) Alloy-E

Obviously that all samples were in ferromagnetic (FM) phases in the measured temperature range (80K to 400K). The as prepared sample showed simple FM-FM transition, Fig 4.21 (a), and Alloy-B, C and D (Fig. 4.21 (b, c and d) respectively) undergoing martensitic transformation from ferromagnetic β (B2) phase to ferromagnetic β' ($L1_0$) phase are accompanied by the shape memory effects. Steps at M_S and A_S shown in Fig. 4.21 (b, c and d) are observed because magnetization saturation is more easily accomplished in the β phase than in the β' phase [42]. These results are similar to those seen in the case of Ni_2MnGa type systems, and occur due to similar effects because of magnetic anisotropy in Austenite and Martensite phases. In field cooled cooling (FCC) and field cooled warming (FCW) curves, the arrows mark A-M transitions temperatures. Besides, it can be seen that the maximum changes in magnetic moments occurred around structural transformation temperatures in Alloys B and D, and there is a remarkable similarity of behavior between these two. These two systems are similar magnetically too.

4.2.3. Dynamic ultrasonic properties:

Elastic modulli of $Co_{36}Ni_{36}Al_{28}$ alloys for different heat trantment were studied using Resonance Ultrasound Spectroscopic (RUS) method (RUSpec, Quasar International). The method has been discussed in chapter. For this study, each sample was cut into a rectangular parallelepiped shape, about 2.5 mm long, 2.4 mm wide and 1.8mm thickness. Fig. 4.22. represents a typical resonance spectrum of all alloys by using RUS technique and shows extraction method (Lorentzian fitting) of Q^{-1} values. Calculations of elastic constants $C_{\alpha\beta}$ is a highly involved procedure. During the frequency sweep various resonance frequencies and amplitudes were obtained as stated before. Individual elastic constants were then found by non linear fitting of the full curve with preliminary estimates of them given as initial guess input parameters. This is a highly involved and lengthy process [66], however, the spectrometer has inbuilt program to handle it.

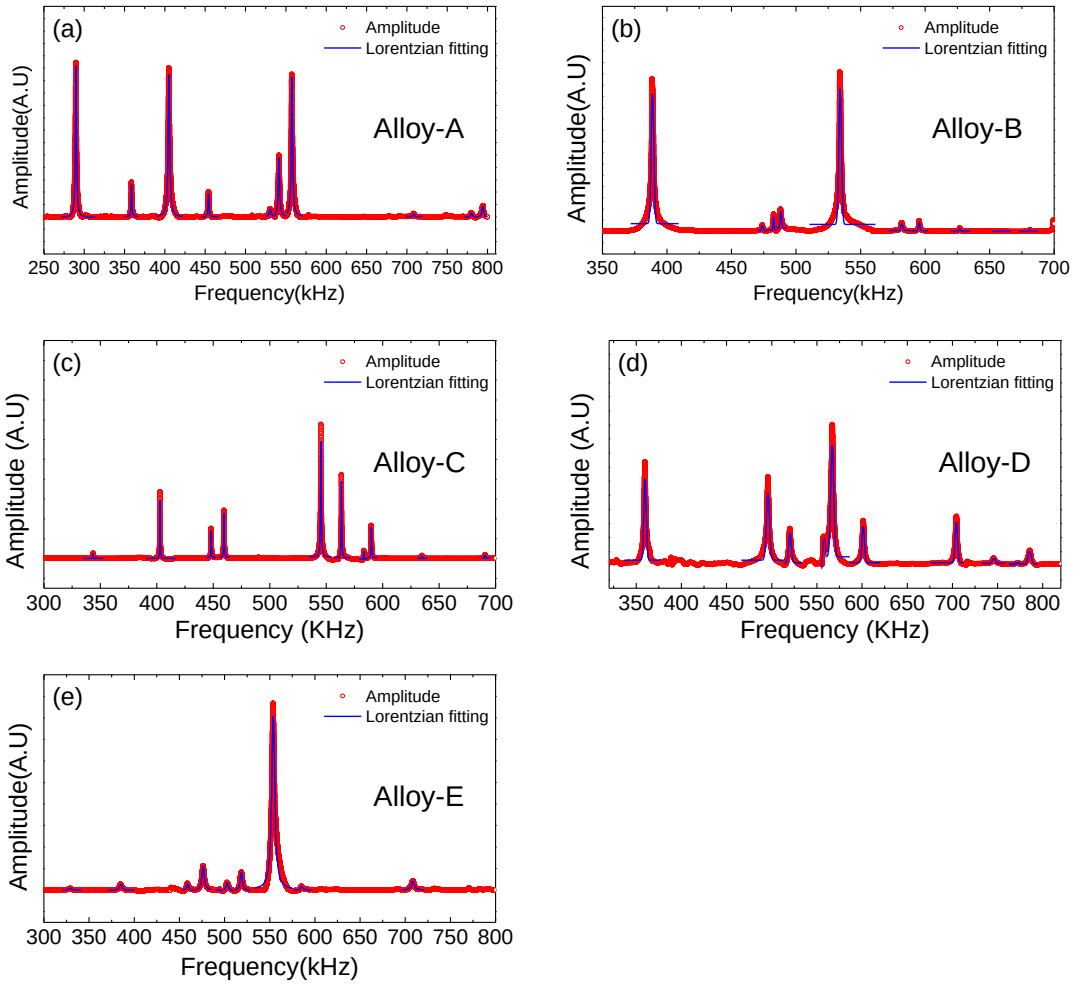

Figure 4.22: Resonance frequencies and Lorentzian fitting of samples, (a) for Alloy-A and (b) Alloy-B (c) Alloy-C (d) Alloy-D and (e) Alloy-E. The fitting lines are in blue.

Of all the constants, the C_{11} which is the uniaxial or Young's modulus and $C_{44,}$ i.e. the shear modulus are important to us, these are calculated and tabulated in table 4.13. Results of measurements for all alloys are compiled in Table 4.13. .

Table 4.13. Elastic moduli and phase fraction calculations for the samples. Sample volume for each rectangular sample used is given along with internal friction (Q^{-1}).

Sample	V (mm^3)	Q^{-1} (X10-3)	C_{11} (GPa)	C_{44} (GPa)	E (GPa)	K (GPa)
Alloy-A	12	5.3±1.1	49.61±1.03	22.86±0.79	49.04	19.13
Alloy-B	12	2.4±1.2	64.72±0.08	35.17±0.08	63.65	17.83
Alloy-C	16	1.0±0.1	52.18±0.36	20.46±0.16	48.19	24.89
Alloy-D	11	5.8±0.9	63.10±1.68	31.51±1.60	63.10	21.09
Alloy-E	12	6.4±1.2	40.03±1.08	15.63±0.66	36.88	19.19

Again taking Alloy-A as the base material, elastic property changes brought by the heat treatments can be compared among the alloys about. It is obvious that heating and subsequent annealing had greatly affected the Cs and Q^{-1}. It is found to be generally the increase and decrease in elastic constants (i.e. Cs) are directly related to the γ phase fraction, but Q^{-1} correlation is more complicated. In case of Alloys B and C, the elastic constants, Cs have improved, but Q^{-1} decreased for Alloy B and increased for Alloy D. Since the morphology seems to be similar between these two, one has to assume that intergrain coupling with γ matrix is better for β, so is this reduction. The phonons were less scattered here. However, further drop in Q^{-1} for Alloy C is not explainable in this way, however, it is satisfying to find that Cs have come round to those in Alloy A. In case of Alloy E, while Cs are the lowest, Q^{-1} is the highest. A possible explanation may be that here the amount of phase is the highest here, so like in β' case of Alloy D, the Q^{-1} is also largest, and being three phase system, phonon scattering is also the highest here, thereby increasing the loss factor Q^{-1}.

All these findings are condensed in a master graph of Fig. 4.23, showing the effect of heat treatment on various properties. There seems to be bunching of structural transformation temperatures in two compositions where γ phase proportion is higher, here the elastic properties also showed higher values. Since these are obviously correlated, measurement of ultrasonic properties is a useful tool to judge the characteristics and usefulness of a particular alloy. Therefore, by adjusting heating schedule, it is possible to tune mechanical properties of the alloy to the desired values for use in a given application.

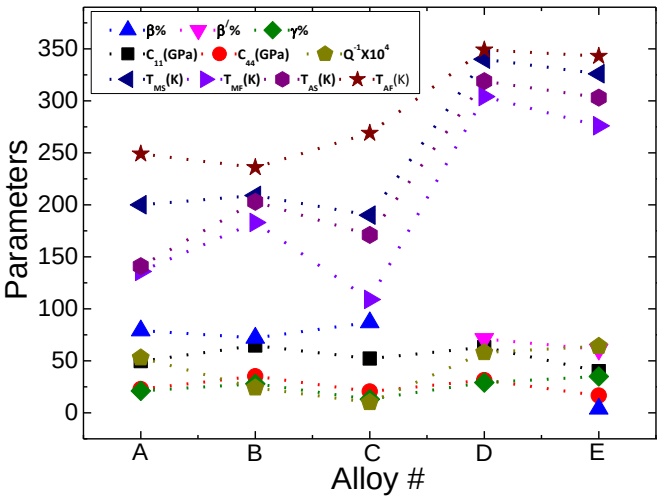

Figure 4.23: Various properties are plotted against each sample, labelled as Alloy number. Units of Y axis are in the same units as for each parameter. The lines are only a guide to eye.

4.3. Discussions:

In summery, we have prepared the nominal compositions of $Co_{39}Ni_{34}Al_{27}$ and $Co_{36}Ni_{36}Al_{28}$ and annealed these at different temperatures and for different times. In $Co_{39}Ni_{34}Al_{27}$ showed that the γ phase fraction increased due to annealed at high temperature. In this sample the percentage of γ phase fraction increased to 16% from 6.3%. This impacted on the dynamic elastic part. So we did the analysis of the mechanical behaviour at different stresses and also in the uniform magnetic field of 300Oe. At very low temperature (below 25K) for this sample there is found a glassy magnetic field interestingly. The other sample of nominal composition $Co_{36}Ni_{36}Al_{28}$ was also analyzed by structures and dynamic ultrasonic properties under different heat treatment. The dynamic part for this sample was optimized by the elastic moduli and correlated with the microstructures.

Chapter 5

Stress locking effects in a CoNiAl FSMA

Since the Austenite – Martensitic structural transformation involve movement of groups of atoms, the effect of lattice strain must be very important here. Many experiments were done before on this and showed that indeed the transition temperatures did shift on application of external mechanical force. These were generally on Ni_2MnGa type of Full-Heusler alloy systems. We measured and reported on the Half-Heusler CoNiAl systems, and a part is included in chapter-4. However, these were all of instantaneous types, meaning the effect of stress was measured while in that stress. Here we report on aspect of stress locking, whereby the system was kept under stress for six months and then released. The effect of stress locking for an extended period is unique. This may also be important in real life systems where FSMA materials would be used under stressed conditions for a long time. Such ageing effect study was not done before.

5.1. Co-Ni-Al system under stress locking condition

The nominal composition of $Co_{37}Ni_{34}Al_{29}$ alloy in reed shape was made from pure Co, Ni and Al metals using arc melting method and annealed at 1473 K/72h. The preparation process of the sample was exactly as was described chapter-2. The internal structure of the primary sample showed the presence of both β and γ phases along with small amount of martensitic phase β' at room temperature. While measuring $\delta v/v$ the sample was kept inside the VBR apparatus for a long time (~6 months). The sample showed very interesting result which originated due to extended time stress locking inside the sample. The actual stressed part was the one that was clamped between two copper blocks tightened with screws as shown in Fig. 5.1 and stress was about 100 MPa. The stress locked inside material showed changes in structure, which affected the physical properties of this sample. the characterization measurements were done as before.

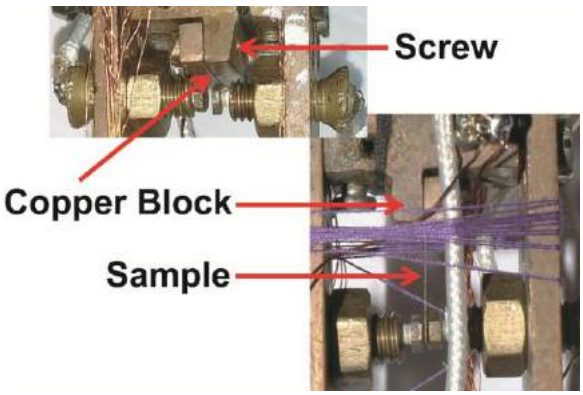

Figure 5.1: The reed shaped $Co_{37}Ni_{34}Al_{29}$ sample in between two copper blocks for long time (~180 days)

We are using the same sample in two different conditions, one that was used in initial measurements is called stress unlocked sample and after keeping it in stressed condition is called stress locked.

5.1.1. Structure and microstructure:

The structure and microstructure has been analyzed for the nominal composition $Co_{37}Ni_{34}Al_{29}$ annealed at 1473K/72h followed by quenching into ice water. The XRD patterns at the room temperature presented in Fig. 5.2 for sample shows that most of the peaks corresponding to both β and γ phases in the samples. The odd/even super lattice peaks of (100), (111), (110) and (200) found in these samples is the confirmation of presence of FSMA β phase and non-FSMA γ phase [59]. There are some extra peaks of

(001), (110), (111), (200) and (201) which is due to presence of martensitic β' phase along with the β and γ phases at room temperature. The structural parameters and phase fractions calculated by the same method of Reitveld refinement shown in table 5.2. The β' phase is increased in stress locked sample due to atom migration by stress.

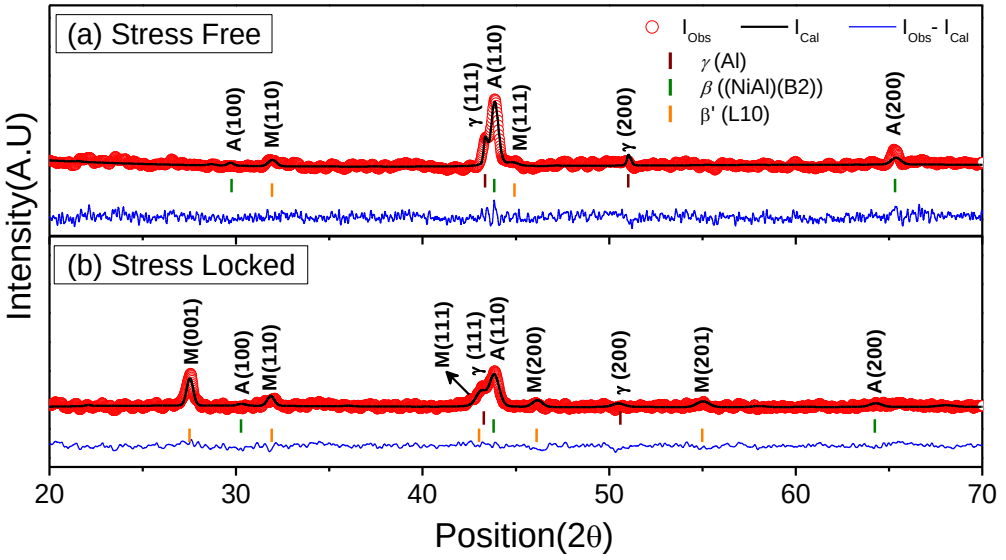

Figure 5.2: Rietveld refinement plot of XRD data of $Co_{37}Ni_{34}Al_{29}$ (a) Stress Unlocked and (b) Stress Locked.

Table 5.1: XRD data analysis of the $Co_{37}Ni_{34}Al_{29}$ and Structural parameters of the unit cell obtained by Rietveld refinement; χ^2 shows the Goodness of fitting $\left(\text{GOF} = \sqrt{\chi^2}\right)$.

Samples	Crystal Structure	Phase Fraction (%)	Cell Parameters	χ^2
Stress Unlocked	Phase: β (B2) Space group: Pm-3m	74.9 ± 2.5	a = b = c = 2.748 (1) Å V = 20.76 (2) Å^3	1.33
	Phase: β' ($L1_0$) Space group: P4/mmm	23.2 ± 2.8	a = b = 3.643 (5) Å, c = 2.834 (10) V = 37.62 (5) Å^3	
	Phase: γ (Al) Space group: Fm3m	1.8 ± 0.1	a = b = c = 3.399 (2) Å V = 39.29(3) Å^3	
Stress Locked	Phase: β (B2) Space group: Pm-3m	23.7 ± 1.2	a = b = c = 2.76 Å V = 23.3 Å^3	2.31
	Phase: β' ($L1_0$) Space group: P4/mmm	74.1 ± 4.0	a = b = 3.855 (5) Å, c = 3.129 (6) Å V = 46.5 (1) (Å^3)	
	Phase: γ (Al) Space group: Fm3m	2.2 ± 0.3	a = b = c = 3.59 (1) Å V = 44.7 (1) (Å^3)	

In SEM Micrograph shown in Fig. 5.3, the multiple β and β' phases together with γ phase can be confirmed from the contrast differences. As discussed before in chapter-4, γ phase contains excess Co. In Table 5.2 the elemental at% in different phases are reported.

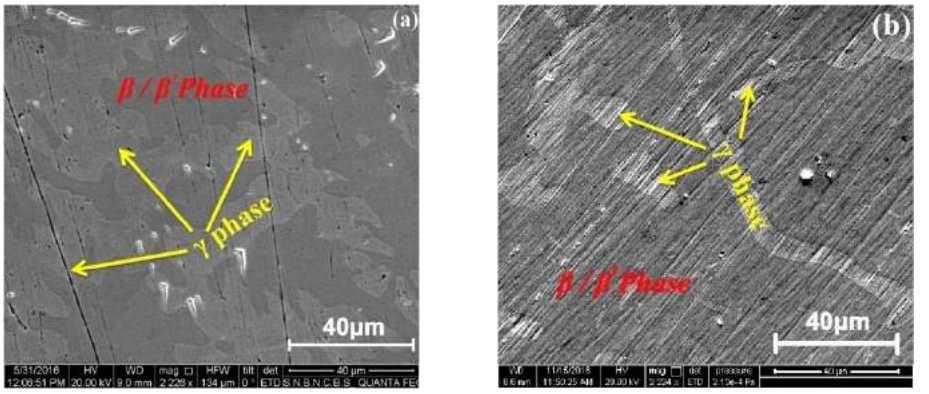

Figure 5.3: SEM micrograph showing B2 or $L1_0$ matrix surrounded by γ phase in homogenized annealed $Co_{37}Ni_{34}Al_{29}$ (a) Stress free and (b) stress locked.

The EDS mapping was done in different specific regions of SEM micrograph where β/β' and γ phases are marked. Hence, the difference came out in the elemental concentrations and the data is given in table 5.2. It is showing that in stress locked sample Co had migrated forming γ phase. Ni concentration remained overall same.

Table 5.2 Elemental at% in different phases in $Co_{37}Ni_{34}Al_{29}$ for stress free and stress locking.

Alloy Compositions	β (at%) or β' (at%)		γ (at%)	
	Co	Al	Co	Al
Stress Unlocked	34.1	34.0	39.5	29.6
Stress Locked	36.8	32.3	52.6	20.3

5.1.2. Resistivity:

Resistivity measurement of $Co_{37}Ni_{34}Al_{29}$, was done in a cryocooler model PT403, made by Oxford Instruments, between 8K and 300K that encompassed the transition ranges. Measurements were done at 111.11Hz to avoid mains borne noise at 50 and 100Hz. The transformation temperatures of Austenitic to Martensitic phase were obtained from the slope changes in the cooling and heating parts of resistivity curve and marked in the graphs shown in Fig. 5.4 (a) as M_s, M_f, A_s and $A_{f..}$ Table 5.3 is the presentation of these points. We see that in the stress locked sample, all transformation temperatures moved up, compared to the stress free one, even if the electrical resistivity was lowered by 1:2.6 times in higher temperatures austenitic phase. The simple possibility is due to more β phase getting transformed into β' phase under loading.

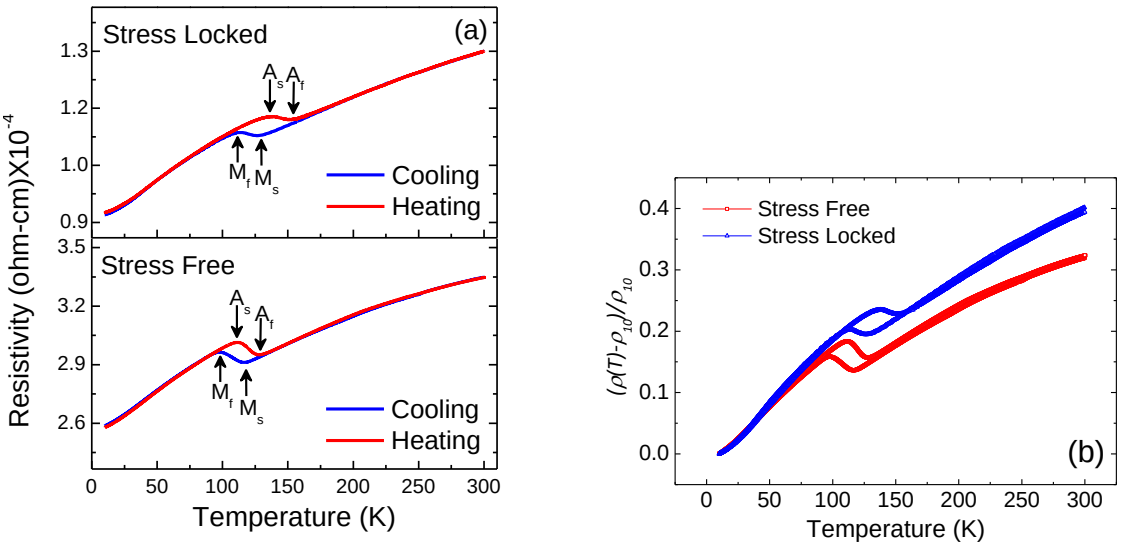

Figure 5.4: Temperature dependent resistivity (ρ) where (a) Resistivity in stress locked and stress free sample (b) Normalized resistivity (ρ)

Table 5.3: Austenite-Martensite transition temperatures of $Co_{37}Ni_{34}Al_{29}$ before and after stress locking obtained from resistivity where $\Delta T = \left(T_{M_s} - T_{M_f}\right)$ and $T_M = ½ \left(T_{M_s} + T_{M_f}\right)$.

Stress	T_{M_s}(K)	T_{M_f}(K)	T_{A_s} (K)	T_{A_f}(K)	ΔT (K)	T_M (K)	ρ (Ωcm) at 300K
Stress Free	117	98	110	129	19	107.5	3.358×10^{-4}
Stress Locked	130	110	136	154	20	120	1.299×10^{-4}

5.1.3. DC Magnetization:

Fig. 5.5 shows the temperature dependent magnetization (M– T) curves in both the stress locked and stress free samples for cooling and heating cycle at a field strength H=150Oe. During field cooling and field heating, i.e. austenitic ↔ martensitic transition can be detected from the steps at Ms and As temperatures., respectively, as shown in Fig. 5.5 (a) and 5.5 (b). Magnetization saturation is more easily accomplished in stress attenuated sample shown in Fig. 5.5 (a) due to higher β' phase inside the sample at room temperature compared to stress free sample [42]. For this stress locked sample magnetic moment is also higher. At the lower temperature below 120K parent β phase completely transform to β' phase in both the samples. So the M-H curves also confirms that magnetic saturation is higher at 100K (Pure martensitic β') shown in Fig. 5.6 as found previously in Co-Ni-Al alloy.

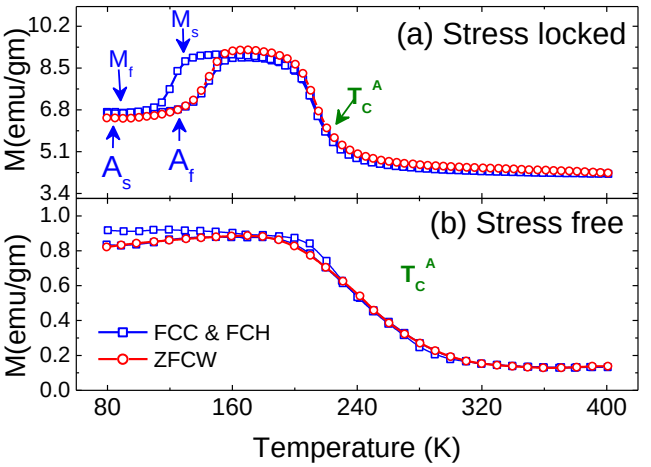

Figure 5.5: Temperature dependent ZFC, FCC and FCW magnetizations at H = 150Oe of stress free and locked samples.

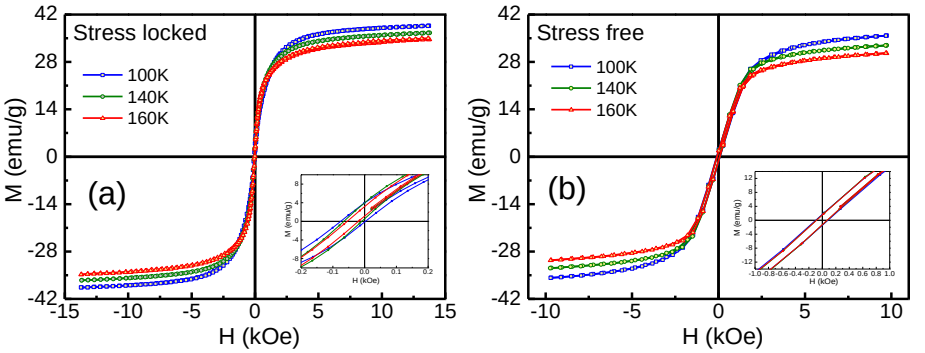

Figure 5.6: *M–H* curves for both the samples at 100 K, 140K and 160 K upon heating that are before and after structural transitions.

5.1.4. AC Susceptibility:

Susceptibility measurements were performed on the samples from 300K to 80K at a frequency of 111 Hz and with the field of 7 Oe for both heating and cooling cycles. The data are shown in the Fig. 5.7. The real part (χ') of ac susceptibility are shown in Fig. 5.7 (a) and the imaginary part (χ'') in Fig. 5.7 (b). As temperature was lowered (χ') increased at the beginning and the peak fell, which shows that upon subsequent martensitic transition. Simultaneously measured $\chi(2\omega)$ and $\chi(3\omega)$ data are also shown in the next two panels. These data show that even if only T_C^A for samples are seen clearly, there were considerable nonlinearities in the vicinities.

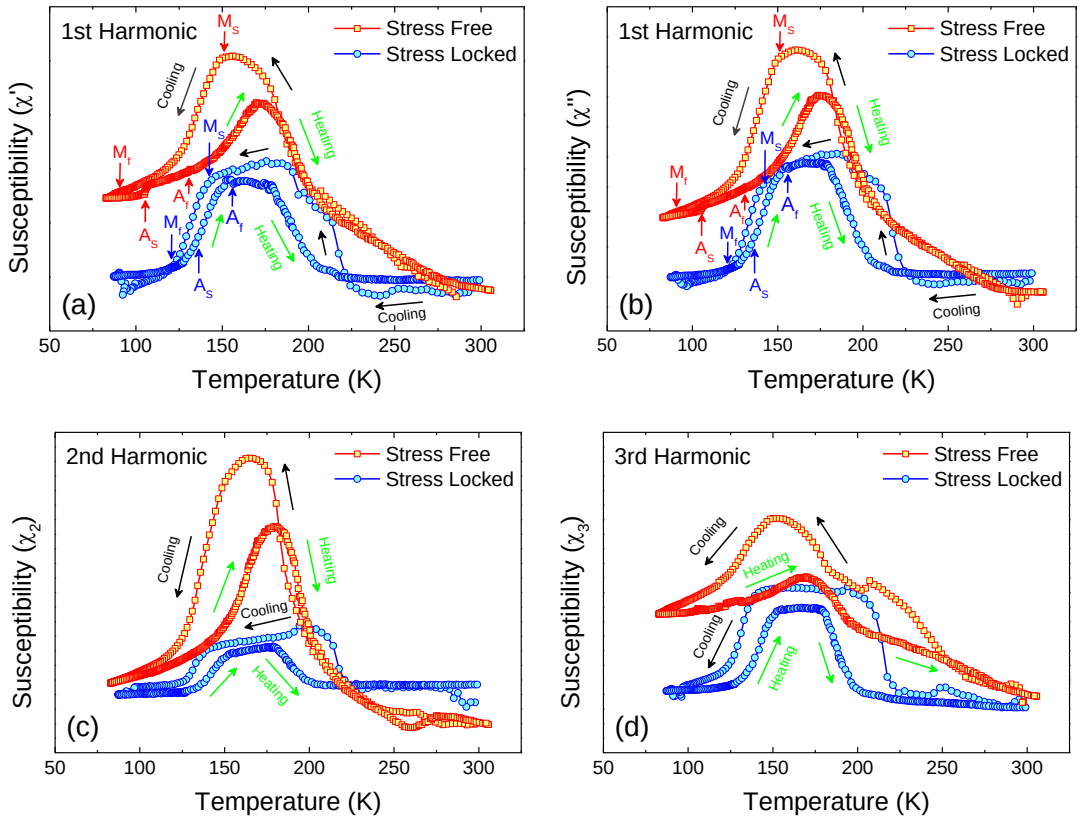

Figure 5.7: Normalized Ac susceptibility data for the stress unlocked and stress locked sample (a) 1st harmonic real part (b) 1st harmonic Imaginary part (c) 2nd harmonic modulus (d) 3rd harmonic modulus.

5.1.5. Sound velocity and Internal friction:

Stress locking effect is the main factor that highly impacted on the structures of $Co_{37}Ni_{34}Al_{29}$ and hence we measured the temperature dependent $\frac{\delta V}{V}$ and Q^{-1} in both the stress locked and free condition. The measurement techniques are same as we discussed before and the results are shown in Fig. 5.8. For both the conditions, more or less elastic recovery is present. Same jump is found in the IF (Q^{-1}) measurement. The transition temperature regions are marked by the arrow.

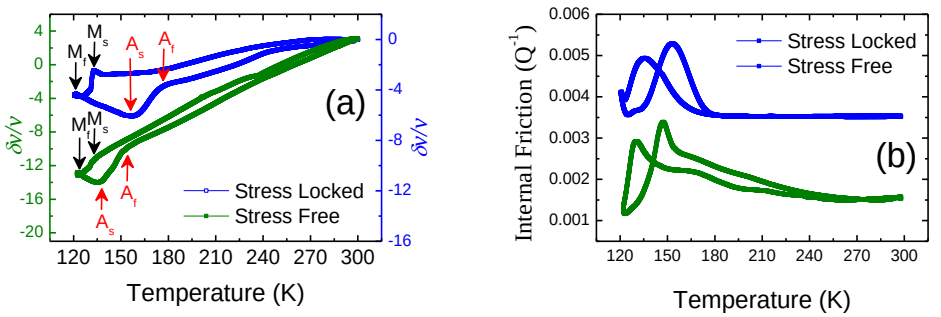

Figure 5.8: (a) Sound velocity and (b) internal friction (Q^{-1}) in $Co_{37}Ni_{34}Al_{29}$ FSMA at low temperature cycling.

The impact of stress-locking in the sample on $\frac{\delta V}{V}$ and Q^{-1} is also drastic. For both the conditions, more or less elastic recovery is present. Table 5.4 is the transition temperatures listed from the relative change in sound velocity with temperature. Same jump is found in the IF (Q^{-1}) measurement.

Table 5.4: Austenite-Martensite transition temperatures of a CoNiAl alloy system in stress free and locked condition obtained from sound velocity.

Samples	Stress	T_{M_s} (K)	T_{M_f} (K)	T_{A_s} (K)	T_{A_f} (K)
$Co_{37}Ni_{34}Al_{29}$	Stress Free	131	124	137	153
	Stress Locked	133	122	157	177

To analyze the $\frac{\delta V}{V}$ i.e. the real part of E, we see from the Fig. 5.8 (a) that, as before, there are two different regions for elasticity that corresponds to pure Austenite and Martensite phases. During this thermo-elastic transition several contributions play role inside the Co-Ni-Al alloy [26]. Assuming the Debye type model [46, 47] total contribution to the real part of E was a sum of a temperature independent part coming static background, and temperature dependent electronic and lattice contributions as

$$\frac{\delta v}{v} = A + BT^2 + CT^4 \qquad (5.1)$$

where $B = (d^2E/d\varepsilon^2), C = d^2L/d\varepsilon^2$, E is electronic and L is lattice contributions and ε is the elastic strain. Each contribution has been evaluated from the fitting lines using equation 5.1 shown in Fig. 5.9 (a-d) for the Pure Martensitic and Pure Austenitic phases only. Table 5.5 gives the numerical values. For both heating and cooling cycles stress-locked sample is showing higher value of electronic contribution and lattice contribution in pure austenitic and martensitic phases.

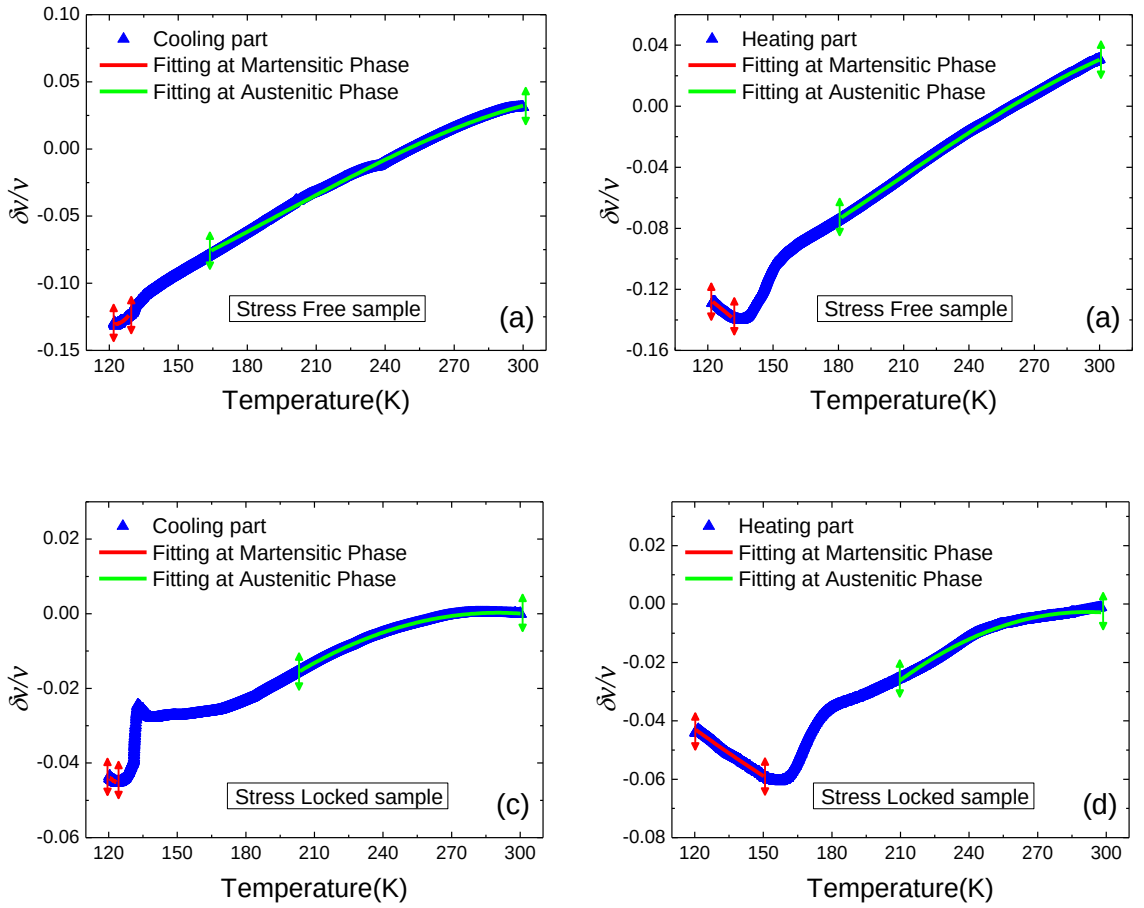

Figure 5.9: Power law fit at pure martensitic and austenitic phase; (a and b) show elastic contributions to cooling and heating cycles of the $Co_{37}Ni_{34}Al_{29}$ at stress free sample, (c and d) show the same for stress locked sample.

Table 5.5: Variation of different contributions during structural transition calculated by power law fitting, B and C express from electronic contribution and lattice contribution respectively.

Stress	Cycle	Martensitic Region				Austenite Region			
		Temp. Range (K)	A	B	C	Temp. Range (K)	A	B	C
Free	Cooling	122-129	0.44	-7.6×10^{-5}	2.5×10^{-9}	164-299	-0.16	3.5×10^{-6}	-1.5×10^{-11}
	Heating	122-132	-0.06	-4.7×10^{-6}	3.2×10^{-12}	181-299	-0.02	3.5×10^{-6}	-1.3×10^{-11}
Locked	Cooling	119-124	6.6×10^{-5}	-0.02	0.99	203-300	$-2.1X10^{-6}$	0.001	-0.17
	Heating	210-300	1.1×10^{-5}	-8.3×10^{-4}	0.04	120-150	$-3.5X10^{-6}$	0.002	-0.30

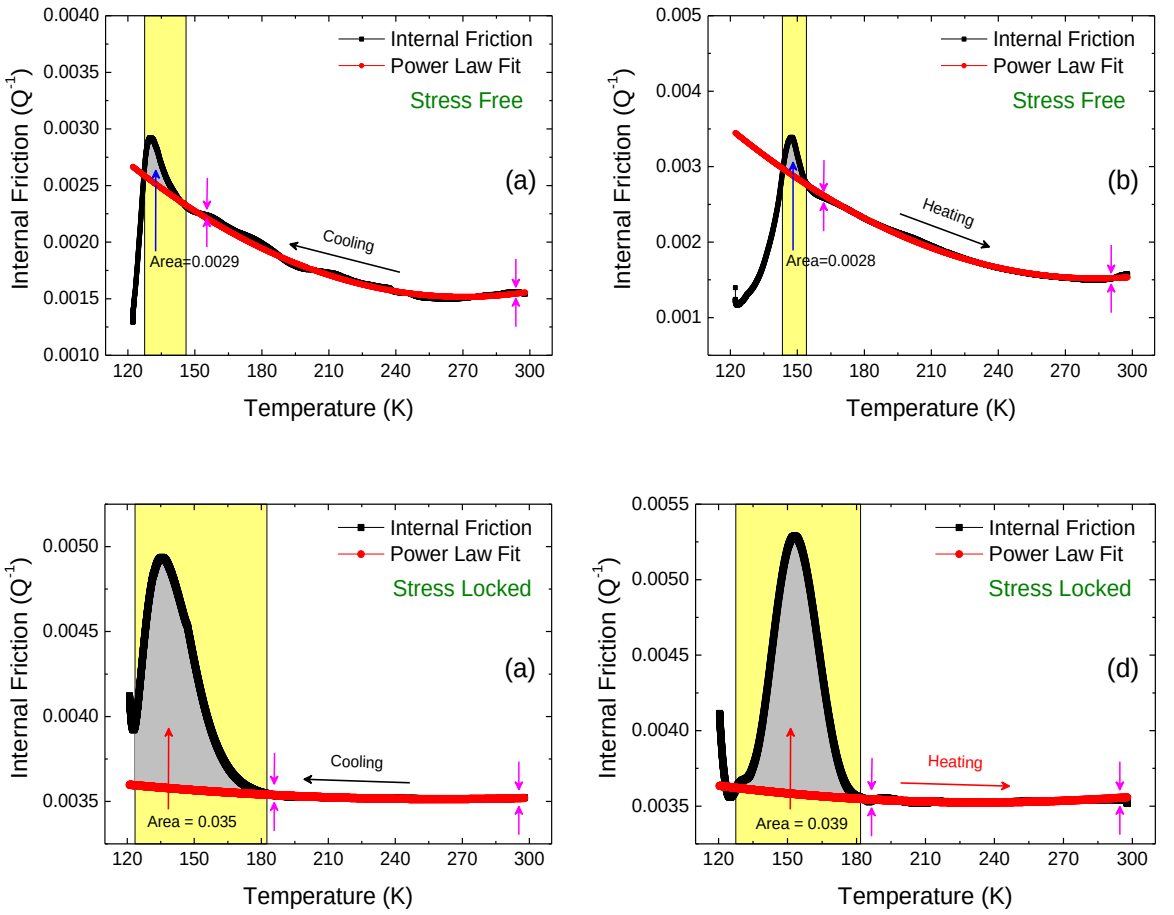

Figure 5.10: Stress induced area of internal friction during structural transition in $Co_{37}Ni_{34}Al_{29}$ determined by background correction using power law fitting.

From temperature dependent IF measurement same jump is found where the SV drops. In stress-locked sample the jump is 1.5 times from room temperature value whereas in stress-unlocked sample the jump is 2 times. But the room temperature IF (Q^{-1}) is 2.3 times higher in stress-locked sample compared to stress-unlocked sample. The area under curve has been measured from the background correction of Q^{-1} done same we did for $\delta v/v$ using Equation 5.1 to find the value of total IF during the structural transition. This area is shown in table.5.6 and it is showing about 12 times higher value in stress locked sample. This means that stress locked sample has higher damping properties due to stress locked inside it. This must be due to stress induced reorientation of the martensites or inter conversion of β to β', or both, however, it is not possible to pinpoint the cause.

Table 5.6: Room temperature Internal Friction under the application of stress locked 8.45MPa and the area during transitions for $Co_{37}Ni_{34}Al_{29}$ alloy.

Stress	Cycle	Area	Q^{-1} at RT	R^2
Stress locked	Cooling	0.035	0.0035	0.93
	Heating	0.039	0.0035	0.70
Stress Free	Cooling	0.003	0.0015	0.98
	Heating	0.003	0.0016	0.99

5.2. Discussions:

Therefore, we find that due to stress locking inside a Co-Ni-Al FSMA has increased the amount of martensitic β' phase at room temperature and modified the transition temperatures. In such condition the electronic and lattice contributions also increased much and structural transition temperatures are shifted to the higher side. The nonlinearity of magnetization study also reported significant non-linearities near T_C^A, but the difference between stress locked and free systems are not as great as in $\delta v/v$ or Q^{-1}. So we can conclude that the effect of stress was more on modification of structural properties rather than magnetic nature.

Chapter 6

Investigations on Metallic glass Materials

Metallic glass materials are are an important class of material that have short-range atomic order and structurally they form amorphous structure in the asprepared state. These materials are prepared by the rapid quenching techniques for chilling metallic liquids at very high rates of 10^5-10^6 K/s. Hence, the process of nucleation and growth of crystalline phase could be kinetically bypassed in some alloy melts to yield a so called frozen liquid configuration resulting high resistivity, low magnetocrystalline anisotropy and no microstructural inhomogeneities. Since amorphous state is metastable, some nanocrystalline grains can be dispersed easily in a residual amorphous matrix with increasing temperature. In this chapter we shall discuss about the structure and microstructures of three compositions of metglass material named Finemet®.

6.1. Investigations on $Fe_{76.5}Cu_1Si_{13.5}B_9$

6.1.1. Structure and microstructure of $Fe_{76.5}Cu_1Si_{13.5}B_9$:

A FINEMET$^{(R)}$ alloy $Fe_{76.5}Cu_1Si_{13.5}B_9$ (nominal composition) metallic glass ribbon samples were prepared with the dimensions- 6mm width and 20 to 22 µm thickness by melt spinning technique as indicated in chapter 2. The X-ray diffraction technique has been used to identify the crystallized phases as well as the grain size of the nanocrystallites that developed during preparation. X-ray analysis of the sample in this as-quenched phase was found to be partially amorphous with a peak at $2\theta = 44^o$ corresponding to the (110) plane of the crystalline bcc-Fe (Si) phase, and a broad hump at 82° signifying amorphousness of the sample as shown in Fig. 6.1. The origin of this hump is short range atomic ordering. The X-ray diffractometry is a rather convenient method for studies of sizes of crystallites constituting materials. The grain size (D_g) of the crystallites have been calculated from the line broadening of the fundamental peak (110) using Scherrer's formula as

$$D_g = \frac{k\lambda}{\beta \cos(\theta)} \qquad [6.1]$$

Where D_g is the grain size and λ is the wave length of Cu-Ka radiation. β is the full width at half maximum (FWHM) measured in radians and is the half of angle of Theta that reflected from crystalline plane, K is the Sherrer constant dependent on crystallite's shape. For oblate shape of the crystallite K value is 0.9 [94, 95]. Grain Size calculated from the fundementa peak is about 8.50 nm from the Lorentzian fitting. Such value in general conforms with the size of the huge amount of smallest particles found on the AFM topography maps.

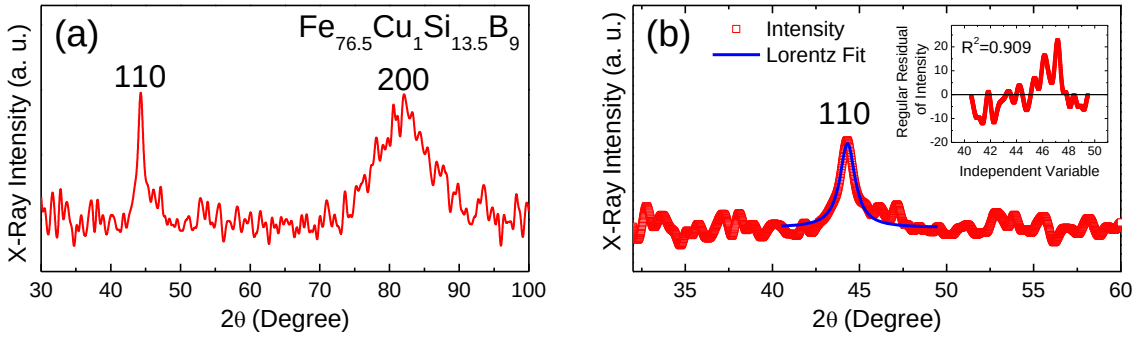

Figure 6.1: X-ray diffractogram of $Fe_{76.5}Cu_1Si_{13.5}B_9$ (a) the overall XRD peak in the range of $60° < 2\theta < 80°$ (b) fitting of the fundamental peak.

On the other hand, the SEM scans, taken at 5 different places for each two faces and one of such images is presented in Fig. 6.2. Crystallite was hardly observed in the micro structure even for the magnification of 800 kX shown in Fig. 6.2 (b), implying that the ordering was short ranged.

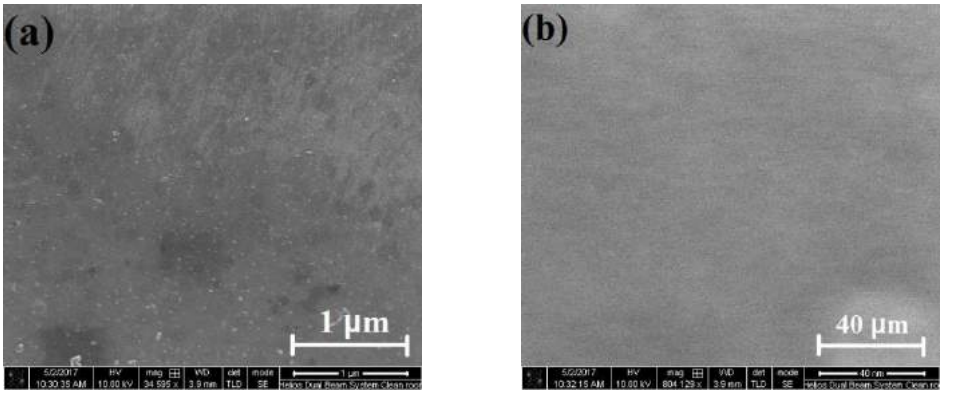

Figure 6.2: SEM image of as prepared $Fe_{76.5}Cu_1Si_{13.5}B_9$ sample, at (a) 34 k× zoom and (b) 804 k× zoom

The partial amorphousness in $Fe_{76.5}Cu_1Si_{13.5}B_9$ is confirmed from the atomic force microscopy (AFM) measurement. The investigated area of 10 µm by 10 µm of the FINEMET sample had a root mean square (RMS) roughness of 6.4 nm and an average roughness of 4.5 nm. The topography of the sample surface reflects the presence of some particles on the right edge side of its surface with different sizes. In this case, average size of the larger particle is 114 nm with an average height of 135 nm. The rest part of the total surface is covered with many small particles that resulted into the amorphousness. The surface view in 2D and 3D view is shown in Fig. 6.3 (a) and (b).

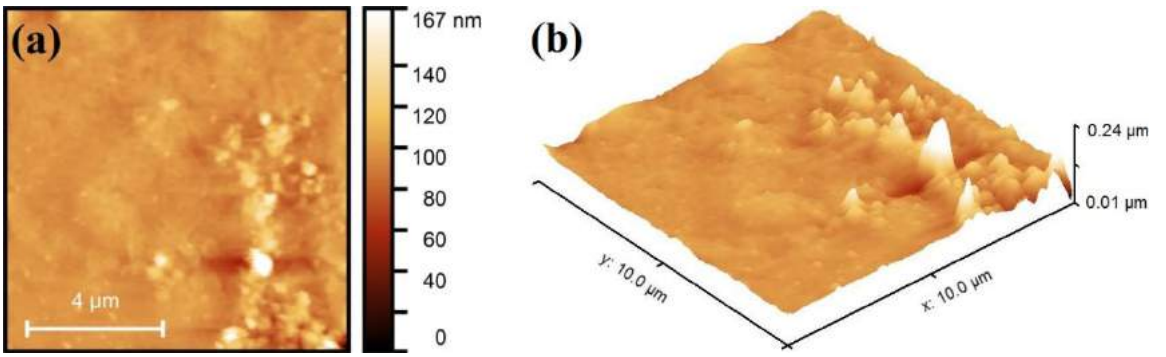

Figure 6.3: $Fe_{76.5}Cu_1Si_{13.5}B_9$ ribbon with thickness of 20 µm (a) 2D topography and (b) 3D topography in real scales.

6.1.2. Magnetic properties of $Fe_{76.5}Cu_1Si_{13.5}B_9$:

Magnetic hysteresis curves of the samples were measured upto a maximum field of 15 kOe for two different temperatures 80K and 300K as shown in Fig. 6.4. The sample was soft ferromagnetic with low coercivity (H_C), between 80 and 300K, and table 6.1 summarizes the data.

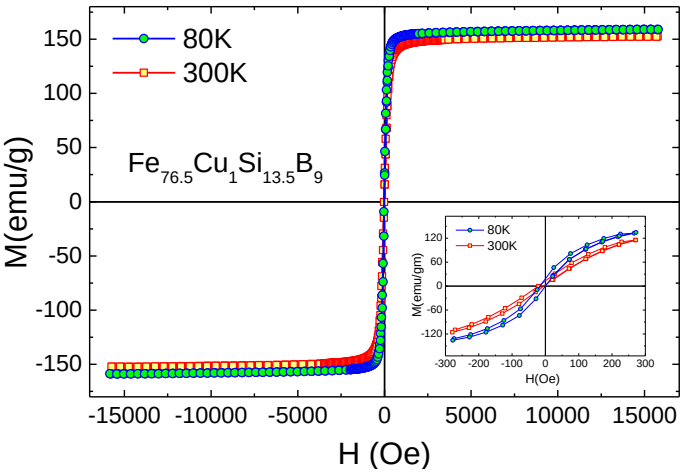

Figure 6.4: Hysteresis loops in $Fe_{76.5}Cu_1Si_{13.5}B_9$ at 80 and 300K (inset shows expanded view around 0 field)

The high field behavior showed easy saturation within 1kOe, and the magnetic saturation (Ms) was around 150emu/gm, similar to bulk Fe (217.6 emu/gm) and Ni (55 emu/gm) systems [96]. This showed that the system had a very low magnetocrystalline anisotropy energy and consequently low magnetostriction. These two are important technical parameters for applications.

Table 6.1. Values of magnetic parameters at two temperatures

Sample	Temp	M_s (emu/g)	H_c (Oe)
$Fe_{76.5}Cu_1Si_{13.5}B_9$	80K	159	8
	300K	153	10

6.1.3. Resistivity of $Fe_{76.5}Cu_1Si_{13.5}B_9$:

The law temperature resistivity of $Fe_{76.5}Cu_1Si_{13.5}B_9$ was measured in the range of 4K to 300K by four probe method as discussed in chapter-2. The temperature dependent resistivity curve are shown in Fig. 6.5 during a heating and cooling cycle. The trend was entirely metallic over the full range, showing mainly linear behavior over the full temperature range.

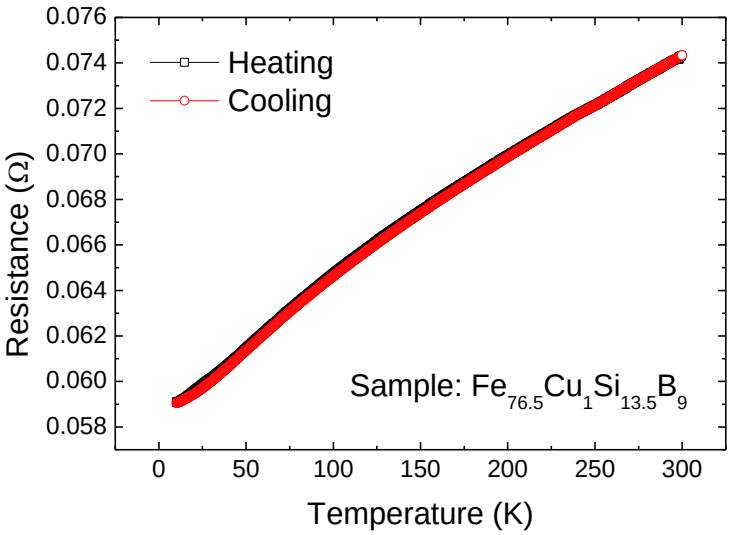

Figure 6.5: Resistance of the sample under no magnetic field in $Fe_{76.5}Cu_1Si_{13.5}B_9$.

6.1.4. Sound velocity and Internal friction in $Fe_{76.5}Cu_1Si_{13.5}B_9$:

The resonance plot of $Fe_{76.5}Cu_1Si_{13.5}B_9$ at room temperature shown in Fig. 6.6 (a) for both real and imaginary parts. Fig. 6.6 (b) shows the fitting curve for the real part of resonance to calculate IF (Q^{-1}). Amplitude of oscillation of $72\mu V$ was obtained for $130N/m^2$ stress. We operated the temperature scan experiment at this stress level.

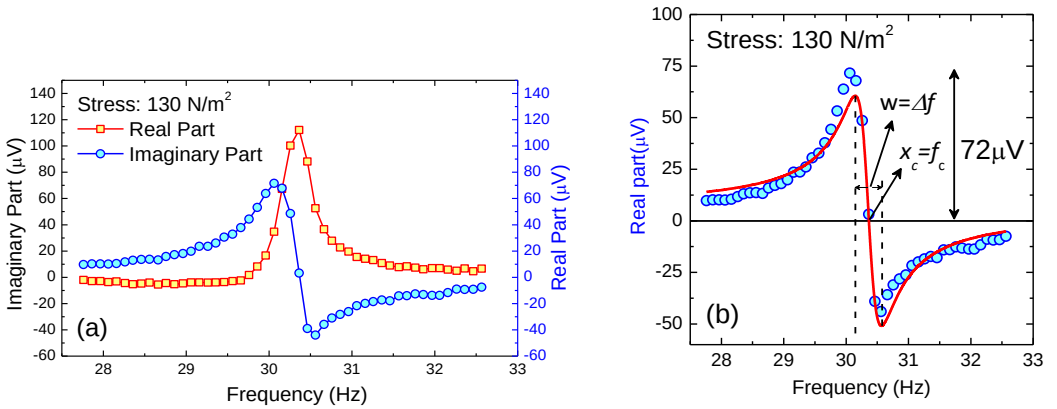

Figure 6.6: (a) the real and imaginary parts of single resonance for the reed. (b) The width of resonance Δf and resonance frequency f_c obtained by fitting.

The elastic properties were measured continuously as a function of temperature by the VBR technique as discussed in Chapter-2, cooled from 300K down to 140K and then heated back. Initially this was under no field condition. Now, with the same drive voltage, same set of measurements were done on the sample with full 1A current in the coil, applying 300 Oe on the sample. Since it is shown in chapter-4, the Q^{-1} depends on these

systems on applied stress level, hence this parameter was carefully kept constant. Fig. 6.7 shows both $\left(\frac{\delta V}{V}\right)$ and Q^{-1} with and without magnetic field, in heating and cooling cycles.

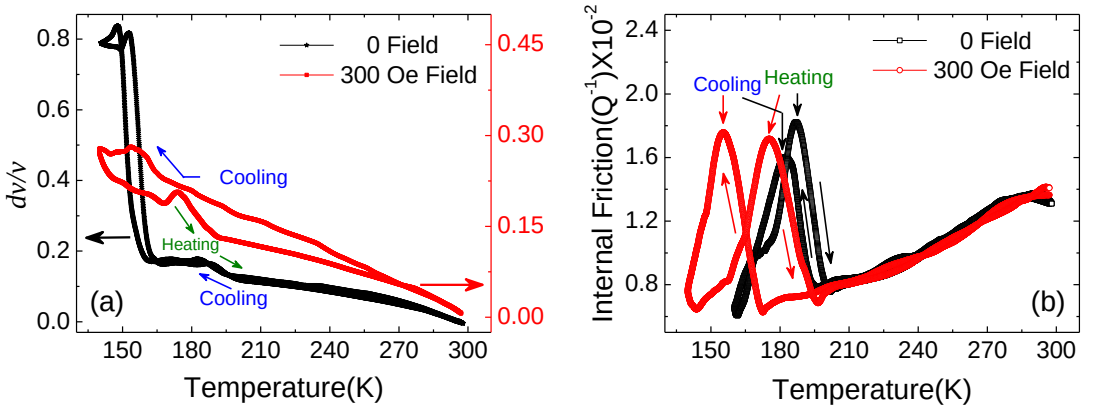

Figure 6.7: (a) Sound velocity $\left(\frac{\delta V}{V}\right)$ and (b) internal friction (Q^{-1}) changes in the sample, without and with applied field in $Fe_{76.5}Cu_1Si_{13.5}B_9$.

First observation is that there are peaks in the behaviour of both $\frac{\delta v}{v}$ and Q^{-1} at about 180K, with a small hysteresis, even though evidently $\frac{\delta v}{v}$ underwent a much smaller change in-field from the zero field behaviour. It is interesting to note that in comparison with similar sized and shaped polycrystalline alloys in previous chapters, the Q^{-1} was about an order of magnitude larger, this increase in attenuation must be coming from amorphousness of metglass, wherein the fine particles were presumably offering more scattering to the phonons. The peaks in both $\frac{\delta v}{v}$ and Q^{-1} got shifted to lower temperature under the application of H and with a larger hysteresis. It is noteworthy that even with a marked change in Q^{-1} and even in $\frac{\delta v}{v}$, the high temperature behaviour was always fully regained in all cases. The cause of much stronger peak in $\frac{\delta v}{v}$ at lower temperature is probably of magnetic origin, for it was absent under magnetic field. It was not found under magnetic field, presumably it went down even further. It was not evident in the Q^{-1} curves. Since this could not be explored any more due to the limitations in the existing setup, it is not discussed any further. We focus on the real part of the sound velocity $\left(\propto \sqrt{E}\right)$ here. We assume as before that the sound velocity is described by the Debye type model, written as $\frac{\delta v}{v} = A + BT^2 + CT^4$, where A is the temperature independent static part, B has electronic contribution and C is the lattice part. The fittings are done in two

regions- above the peak (high temperature) and below the peak, but excluded the very low temperature region. The results of the fitting are shown in the fig. 6.8 and given in table 6.2.

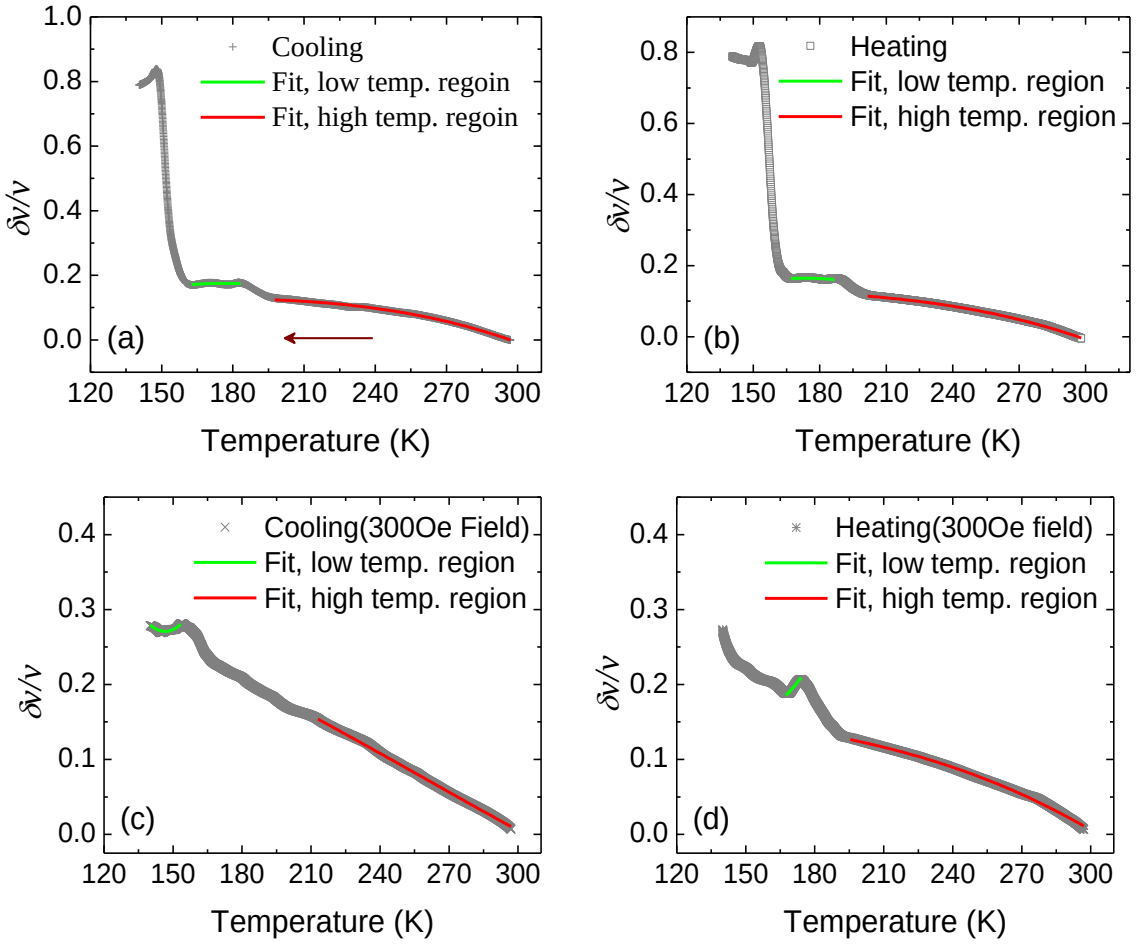

Figure 6.8: Power Law fits at low and high temperature regions of sound velocity in $Fe_{76.5}Cu_1Si_{13.5}B_9$ (a, b) shows without magnetic field and (c, d) in presence of magnetic field of 300 Oe.

Table 6.2: Variation in different contributions in $Fe_{76.5}Cu_1Si_{13.5}B_9$ calculated by power law fitting, B and C express electronic and lattice contributions respectively.

Field (Oe)	**Cycle**	**Low temperature region**				**High temperature region**			
		Temperature range (K)	A	B	C	Temperature range (K)	A	B	C
0	Cooling	162 - 183	0.04	8.6×10^{-6}	-1.4×10^{-10}	197 – 297	0.1	2.1×10^{-6}	-3.6×10^{-11}
	Heating	167 - 186	0.01	1.0×10^{-5}	-1.7×10^{-10}	201 – 297	0.1	7.7×10^{-7}	-2.5×10^{-11}
300	Cooling	153 - 140	1.4	-1.0×10^{-4}	2.4×10^{-9}	212 – 297	0.2	-8.6×10^{-7}	-1.8×10^{-11}
	Heating	168 - 174	1.1	-6.7×10^{-5}	1.3×10^{-9}	195 – 297	0.2	-3.0×0^{-7}	-1.6×10^{-11}

The table shows that in magnetic field, the electronic part was severely affected, all contributions changing from positive to negative. Moreover, the low temperature electronic part in magnetic field decreased in field by a significant margin, as with the other high temperature parts. The phononic part was similarly affected only in the magnetic field, below the peak temperature. Since there is no previous work on the structural aspects of these materials at such a low temperature, there is no structural transition expected in any case and finally because it was so strongly affected by external field, we can only assume that the transition was magnetic in origin, and the changes in elastic properties were due to strong magnetoelastic coupling in these materials.

6.2. Investigations on $Fe_{75.5}Cu_1Nb_1Si_{13.5}B_9$ and $Fe_{56}Cr_{17.5}Cu_1Nb_3Si_{13.5}B_9$

We focused on the FINEMET ribbons with grain growth inhibitor Nb and Cr and prepared a nominal compositions $Fe_{75.5}Cu_1Nb_1Si_{13.5}B_9$ and $Fe_{56}Cr_{17.5}Cu_1Nb_3Si_{13.5}B_9$ to study their physical properties as well as the dynamic elastic properties at low temperature.

6.2.1. Structure and microstructure of $Fe_{75.5}Cu_1Nb_1Si_{13.5}B_9$:

We doped the previous metglass material ($Fe_{76.5}Cu_1Si_{13.5}B_9$) with a small amount of Nb to prepare the nominal composition $Fe_{75.5}Cu_1Nb_1Si_{13.5}B_9$ and study its structure and microstructure. Here Nb will act as the grain growth inhibitor. X-ray analysis shown in Fig. 6.9 of the $Fe_{75.5}Cu_1Nb_1Si_{13.5}B_9$ composition in the as-quenched phase shows the fundamental peak at $2\theta = 44^o$ and the other peak at $2\theta = 82.5°$ with broad humps resulting more amorphousness. The grain size calculated from the broad fundamental peak (110) drops to 3.68 nm from 8.50 nm for the Nb undoped Finemet. Yoshizawa [44] claimed that the Nb existence in alloy stabilizes the amorphous state in Nb-rich area and thus inhibits the α-Fe(Si) grain growth. It was a metglass having a composition $Fe_{75.5}Cu_1Nb_1Si_{13.5}B_9$, and could be crystallized by subsequent annealing above recrystallization temperature, giving a bcc Fe-Si solid solution with the grain sizes of around 10 nm embedded in a residual amorphous matrix.

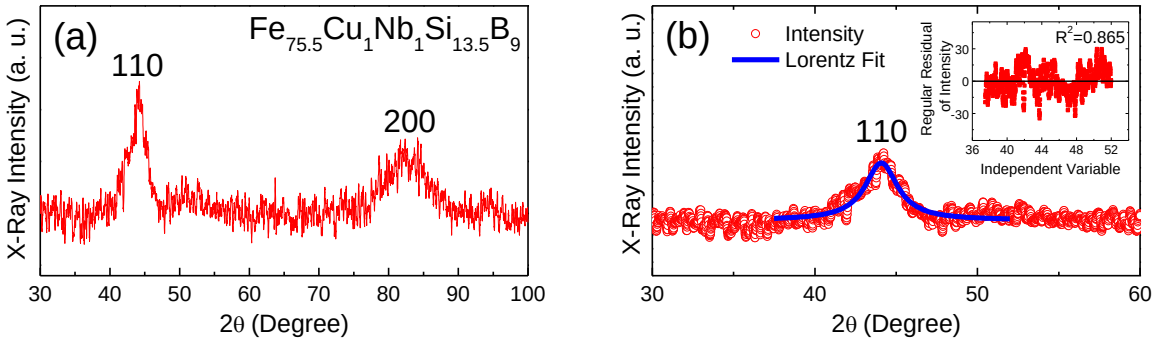

Figure 6.9: X-ray diffractogram of the sample $Fe_{75.5}Cu_1Nb_1Si_{13.5}B_9$ (a) overall XRD peak in the range of $60° < 2\theta < 80°$ (b) fitting of the first peak.

The SEM micrograph of this alloy ($Fe_{75.5}Cu_1Nb_1Si_{13.5}B_9$) was also observed at 5 different places for the lowest possible scale range (400nm) and one of such images is presented in Fig. 6.10. No crystallite was observed in the micro structure implying that the ordering was only short ranged.

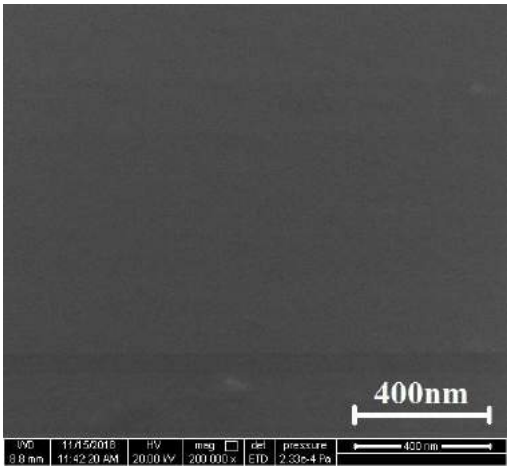

Figure 6.10: SEM image of as prepared $Fe_{75.5}Cu_1Nb_1Si_{13.5}B_9$ sample, at 200 k× zoom.

The composition, $Fe_{75.5}Cu_1Nb_1Si_{13.5}B_9$ is more free of nanoparticles than $Fe_{76.5}Cu_1Si_{13.5}B_9$. From the atomic force microscopy (AFM) measurement the topography of this sample reflects some small particles that kept the sample apart from being fully amorphous. The investigated area of 6μm by 6μm of this alloy had a root mean square (RMS) roughness of 2.2nm and an average roughness of 1.7nm. In this case, average size of the maximum particle is 17 nm with an average height of 11.08 nm. The rest part of the total surface is covered with many small particles that result into the amorphousness. The surface view in 2D and 3D view is shown in Fig. 6.11 (a) and (b).

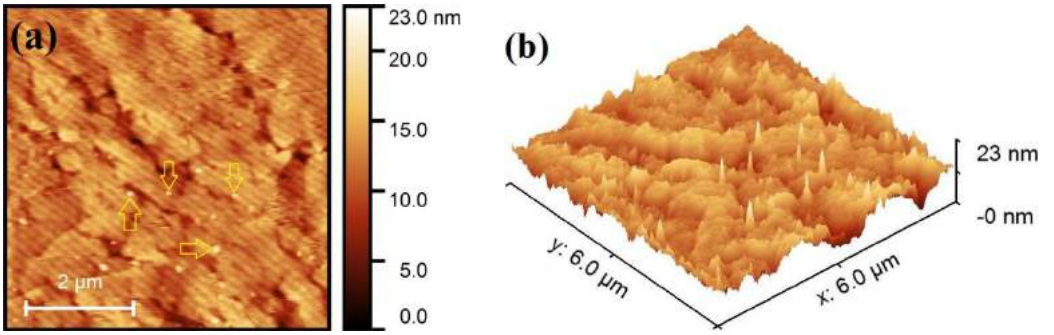

Figure 6.11: $Fe_{75.5}Cu_1Nb_1Si_{13.5}B_9$ ribbon with thickness of 20 μm (a) 2D topography and (b) 3D topography in real scales.

6.2.2. Structure and microstructure of $Fe_{56}Cr_{17.5}Cu_1Nb_3Si_{13.5}B_9$:

We further modified the previous compositions adding more Nb and Cr with the base Finemet alloy to prepare the composition of $Fe_{56}Cr_{17.5}Cu_1Nb_3Si_{13.5}B_9$ using the same rapid solidification technique. Here more Nb and Cr will act as the grain growth inhibitor strongly. X-ray analysis shown in Fig.6.12 of the $Fe_{56}Cr_{17.5}Cu_1Nb_3Si_{13.5}B_9$ composition in the as-quenched phase shows the fundamental peak at $2\theta = 44^o$ to be more broading and the other peak vanishes. The grain size calculated from the broad fundamental peak (110) drops to the lowest value of 1.42nm compared to our other prepared samples resulting to more amorphous.

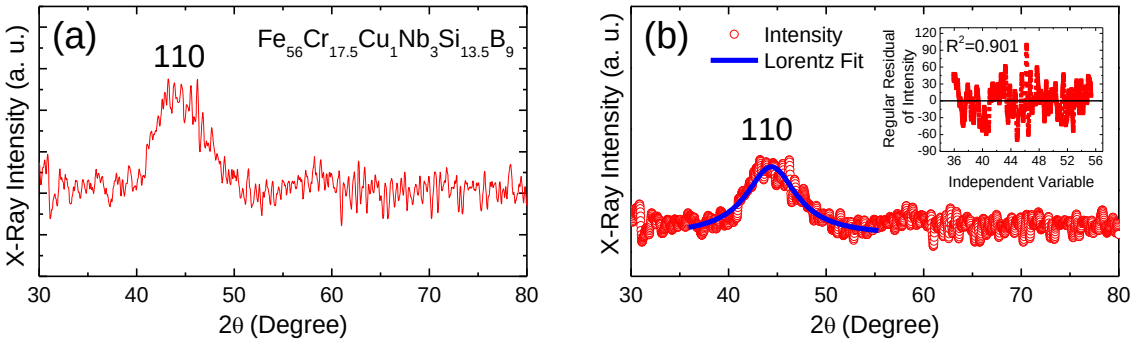

Figure 6.12: X-ray diffractogram of the sample $Fe_{56}Cr_{17.5}Cu_1Nb_3Si_{13.5}B_9$ (a) Fundamental peak that confirms the amorphousness and (b) Lorentzian fitting of (100) broad peak.

The SEM micrograph for this Cr doped $Fe_{56}Cr_{17.5}Cu_1Nb_3Si_{13.5}B_9$ sample shown in Fig. 6.13 is also consistent with the XRD data and there is no identical particle to be present in the whole sample. Same type of images were found even when we repeated the scans for five times.

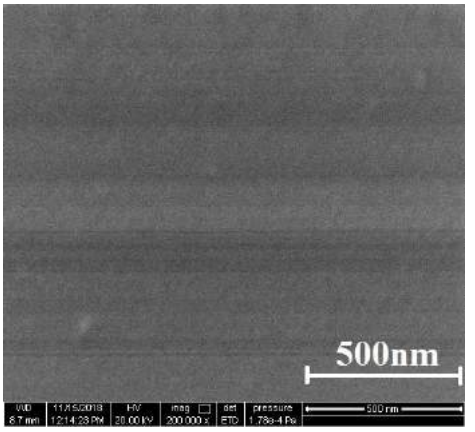

Figure 6.13: SEM image of as prepared $Fe_{56}Cr_{17.5}Cu_1Nb_3Si_{13.5}B_9$ sample, at 200 k× zoom.

Fig. 6.14 is the typical AFM image of quenched $Fe_{56}Cr_{17.5}Cu_1Nb_3Si_{13.5}B_9$ alloy ribbon cross-section. No characteristic structure can be recognized except some visible defect groove that resulted into some roughness of the surface. The investigated area of 1.3 μm by 1.3 μm of this sample had a root mean square (RMS) roughness of 1.49 nm and an average roughness of 1.14 nm.

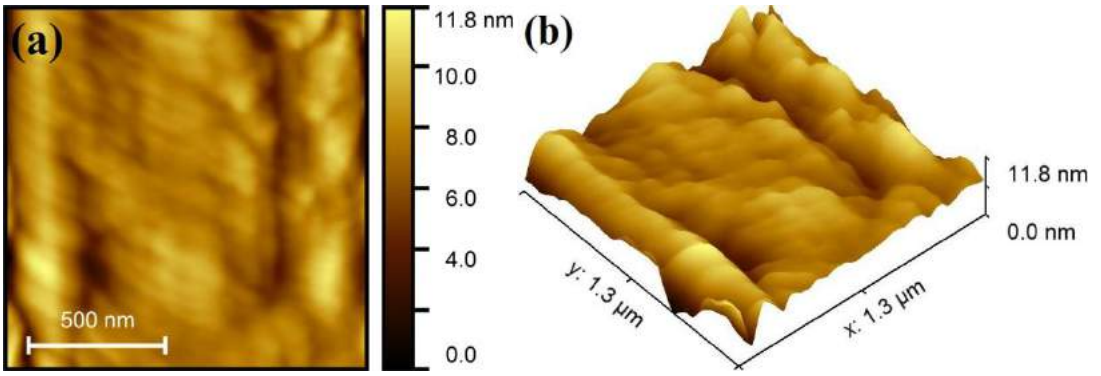

Figure 6.14: $Fe_{56}Cr_{17.5}Cu_1Nb_3Si_{13.5}B_9$ ribbon with thickness of 20 μm (a) 2D topography and (b) 3D topography in real scales.

6.2.3. Magnetization of $Fe_{75.5}Cu_1Nb_1Si_{13.5}B_9$ and $Fe_{56}Cr_{17.5}Cu_1Nb_3Si_{13.5}B_9$:

The high field behavior shown in Fig. 6.15 at 80K showed easy saturation within 1kOe, and the Ms was around 164 emu/gm in $Fe_{75.5}Cu_1Nb_1Si_{13.5}B_9$, similar to bulk Fe (217.6 emu/gm) and Ni (55 emu/gm) systems [96]. This showed that the system had a very low magnetocrystalline anisotropy energy and consequently low magnetostriction. On the other hand $Fe_{56}Cr_{17.5}Cu_1Nb_3Si_{13.5}B_9$ magnetocrystalline anisotropy is very high in $Fe_{56}Cr_{17.5}Cu_1Nb_3Si_{13.5}B_9$ due to low Ms at 80K. The data are shown in table 6.3.

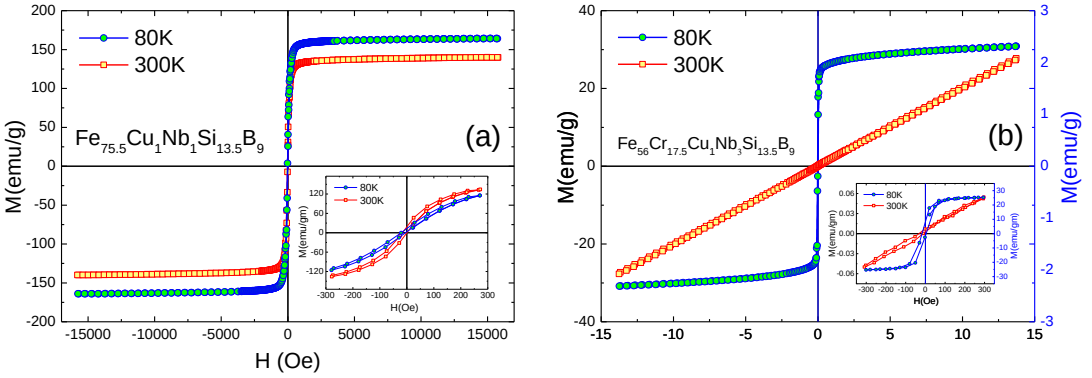

Figure 6.15: Hysteresis loops of the sample at 80 and 300K (inset shows expanded view around 0 field) (a) for sample $Fe_{75.5}Cu_1Nb_1Si_{13.5}B_9$ and (b) for $Fe_{56}Cr_{17.5}Cu_1Nb_3Si_{13.5}B_9$

Table 6.3: Values of magnetic parameters at two different temperatures.

Sample	Temp	M_s (emu/g)	H_c (Oe)	H_{EB} (Oe)
$Fe_{75.5}Cu_1Nb_1Si_{13.5}B_9$	80K	164	24	15
	300K	140	16	8
$Fe_{56}Cr_{17.5}Cu_1Nb_3Si_{13.5}B_9$	80K	30	17	6.5
	300K	--	32	22

The thermo-magnetization below 150K also confirms the presence of a spin wave excitation to follow the relation $M(T) = M(0)\left(1 - BT^{3/2} - CT^{5/2}\right)$ and can be written as

$$\frac{\Delta M}{M(0)} = \frac{M(0) - M(T)}{M(0)} = BT^{3/2} + CT^{5/2} \qquad [6.2]$$

where the leading term gives the Bloch's $T^{3/2}$ law. As seen from the Fig. 6.16, the fitting is quite good. The temperature dependence of the magnetization is due to the excitation of the long-wavelength spin waves. The values of the coefficients B and C obtained from the fitting are given in table 6.4 and the values of B and C is much larger compared to crystalline Fe resulting to amorphous ferromagnetic at low temperature [97].

The C/B ratio is characteristic of the amorphous ferromagnets. The small value of the C/B ratio suggests that the exchange interaction is of short range in this amorphous ferromagnet.

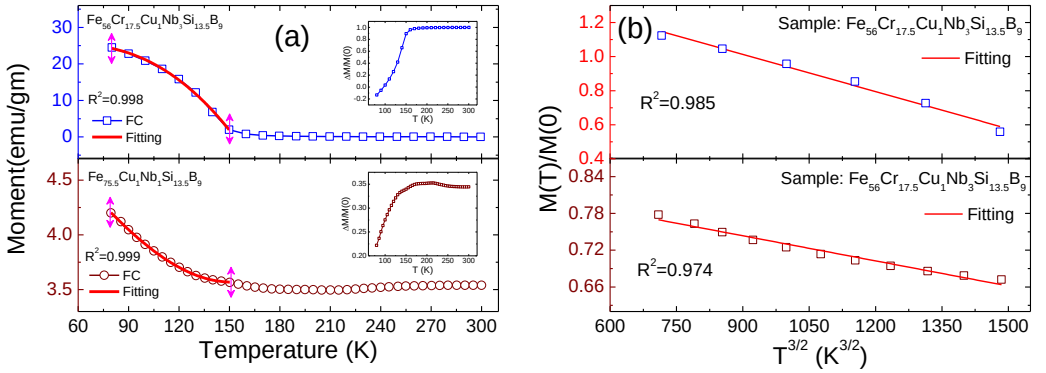

Figure 6.16: Temperature dependent magnetization (a) M-T curve of $Fe_{75.5}Cu_1Nb_1Si_{13.5}B_9$ and $Fe_{56}Cr_{17.5}Cu_1Nb_3Si_{13.5}B_9$ fitting below 150K (low-temperature magnetization data with spin-wave model in 80K to 300K) (b) reduced magnetization $M(T)/M(0)$ as a function of $T^{3/2}$

Table 6.4: The parameters determined by comparing magnetization data with equation 6.1.

Sample	B ($\times 10^{-4}$)	C ($\times 10^{-6}$)	C/B ($\times 10^{-2}$)	M(0)
Nb1	1.36 ± 0.07	1.81 ± 0.02	0.75	5.4
Cr17.5	7.34 ± 0.39	9.36 ± 0.18	1.27	21.8

6.2.4. Resistivity of $Fe_{75.5}Cu_1Nb_1Si_{13.5}B_9$ and $Fe_{56}Cr_{17.5}Cu_1Nb_3Si_{13.5}B_9$:

The low temperature resistivity for $Fe_{75.5}Cu_1Nb_1Si_{13.5}B_9$ and $Fe_{56}Cr_{17.5}Cu_1Nb_3Si_{13.5}B_9$ was measured by the same four probe technique as discussed before and the measurement was for both heating and cooling inbetween 300K to 4K. The temperature dependent resistivity shown in Fig. 6.17 during a heating and cooling cycle confirms entirely metallic behaviour over the full range as before.

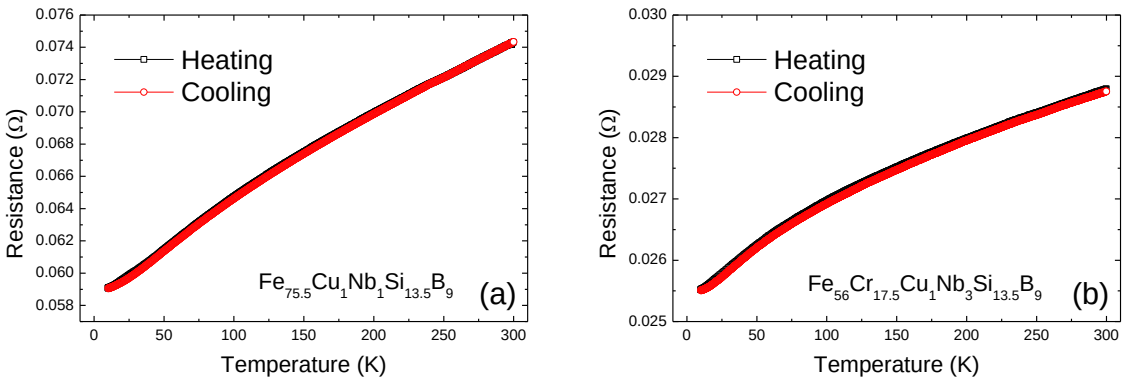

Figure 6.17: Temperature dependent magnetization resistance (a) for $Fe_{75.5}Cu_1Nb_1Si_{13.5}B_9$ and (b) for $Fe_{56}Cr_{17.5}Cu_1Nb_3Si_{13.5}B_9$.

6.2.5. SV and IF in $Fe_{75.5}Cu_1Nb_1Si_{13.5}B_9$ and $Fe_{56}Cr_{17.5}Cu_1Nb_3Si_{13.5}B_9$:

The elastic properties we measured as before continuously as a function of temperature from 300K down to 140K and then heated back. Fig. 6.18 shows SV and Q^{-1} for $Fe_{75.5}Cu_1Nb_1Si_{13.5}B_9$. This was under no field condition. Of course, the earth's magnetic field was not shielded (assumed to be small enough). Small anomalies is observed in $\left(\frac{\delta v}{v}\right)$ near room temperature that is also highly focused in IF (Q^{-1}) measurement.

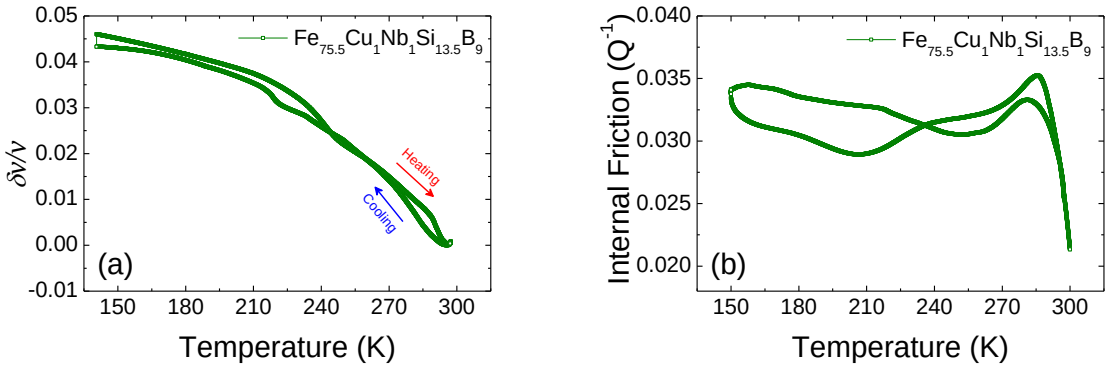

Figure 6.18: (a) Sound velocity $\left(\frac{\delta V}{V}\right)$ and (b) internal friction (Q^{-1}) changes in the sample $Fe_{76.5}Cu_1Nb_1Si_{13.5}B_9$.

The fitting of $\left(\frac{\delta V}{V}\right)$ was done before and after transition temperature as before and extracted the contributions in sample and shown in table 6.5.

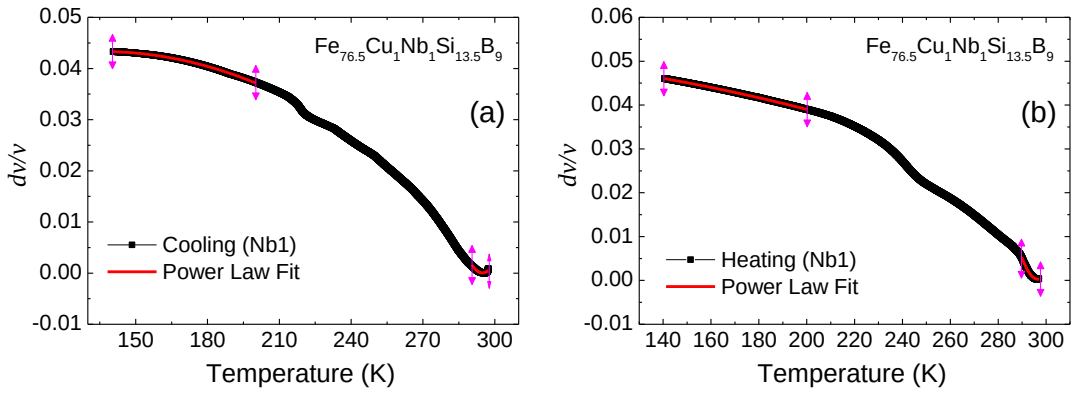

Figure 6.19: Power Law fits at low and high temperature regions of sound velocity of sample $Fe_{76.5}Cu_1Nb_1Si_{13.5}B_9$ (a) during cooling and (b) during heating.

The Cr doped $Fe_{56}Cr_{17.5}Cu_1Nb_3Si_{13.5}B_9$ is also characterized by elastic properties as a function of temperature from 300K down to 150K and then heated back. The dilution of the Fe magnetic moment by Cr in Finemet® alloy strongly affects on the mechanical spectroscopy i.e. sound velocity and internal friction (Fig. 6.20) in low temperature with a

small hysteresis and shifting of transition temperature. Initially we measured without applied magnetic field and then we repeated the measurement in presence of 300 Oe uniform magnetic field as discussed in chapter-2.

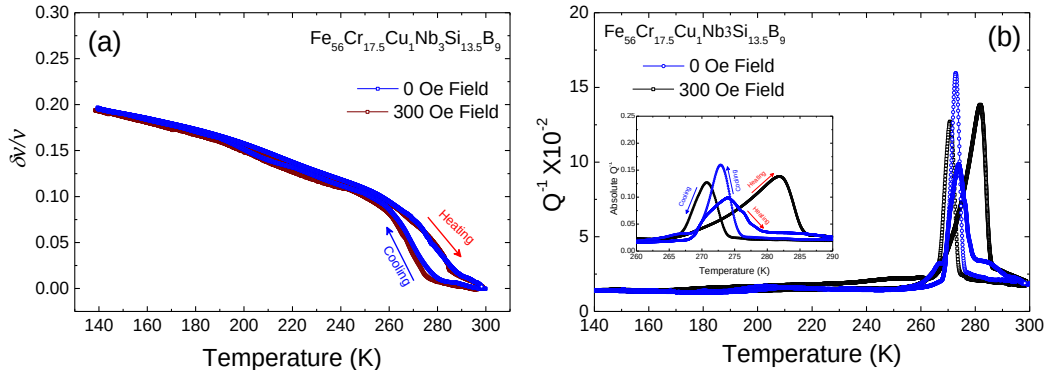

Figure 6.20: (a) Sound velocity $\left(\frac{\delta V}{V}\right)$ and (b) internal friction (Q^{-1}) changes in the sample $Fe_{56}Cr_{17.5}Cu_1Nb_3Si_{13.5}B_9$ in presence magnetic field and without magnetic field.

It is seen from the temperature dependent $\left(\frac{\delta v}{v}\right)$ near room temperature a hysteresis is present and IF (Q^{-1}) also shows the same jump at the same region. So we further measured in presence of magnetic field and extract the contributions by Power-law fitting as before. The combined fitting parameters are shown in Table.6.5.

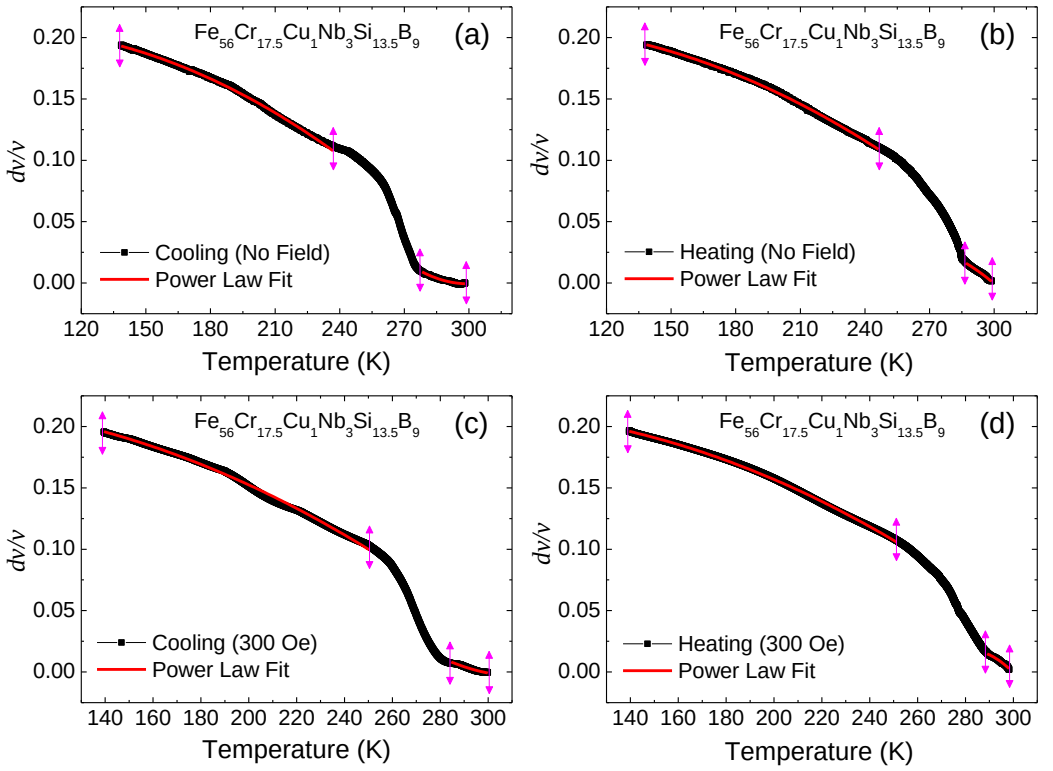

Figure 6.21: Power Law fits at low and high temperature regions of sound velocity in $Fe_{56}Cr_{17.5}Cu_1Nb_3Si_{13.5}B_9$ (a, b) shows without magnetic field and (c, d) in presence of magnetic field of 300 Oe.

Table 6.5: Variation in different contributions calculated by power law fitting, B and C express electronic and lattice contributions respectively.

Sample	Field (Oe)	Low temperature region					High temperature region			
		Cycle	Temp. Range	A	B	C	Temp. Range	A	B	C
Nb1	0	Cooling	140-200	-1.5×10^{-6}	4.0×10^{-4}	0.02	290-297	8.0×10^{-5}	-0.1	6.9
		Heating	140-200	-3.6×10^{-7}	6.0×10^{-4}	0.05	290-297	1.1×10^{-4}	-0.1	9.8
Cr17.5	0	Cooling	138-236	-4.2×10^{-6}	6.1×10^{-4}	0.18	278-298	2.1×10^{-5}	-0.13	1.9
		Heating	138-246	-3.2×10^{-6}	4.2×10^{-4}	0.19	286-298	-8.4×10^{-6}	0.01	-0.3
	300	Cooling	139-249	-3.1×10^{-6}	3.4×10^{-4}	0.21	284-298	1.3×10^{-5}	-0.01	1.29
		Heating	139-250	-3.1×10^{-6}	4.1×10^{-4}	0.2	288-298	-5.3×10^{-5}	0.03	-4.2

The table 6.5 shows that in magnetic field, the electronic part and phononic contribution were not so much affected in the low temperature region for both the samples. Large variations of the contributions are only seen in Cr doped Finemet only at high temperature and in presence of magnetic field the variation decreases.

6.3. Discussion:

In summary, the nominal composition of $Fe_{76.5}Cu_1Si_{13.5}B_9$ metglass, was characterized for amorphousness, microstructure and composition. Magnetization measurements showed it was basically a soft ferromagnet at and below room temperature. Resistivity analysis did not show any structural or magnetic transition in this temperature range. However, the low temperature magnetoelastic measurements showed some transition that was strongly affected by applied magnetic field. This is an unexpected finding, and we claim that this has some magnetic origin that a bulk measurements could not detect. Then we modified the base sample with the addition of Nb and Cr and analyzed the dynamic elastic properties. These samples showed weak transformation compared to the base material. We have reported the electronic and phononic contributions also for Nb and Cr doped samples in this chapter.

Chapter 7

Conclusions and Future Plan of work

In this chapter we summarize all the findings in the previous chapters and conclude. We also indicate some of the areas where future work can be continued.

7.1. Conclusions:

We investigated on two different types of metallic alloy systems in which one is ferromagnetic shape memory alloy and another one is Finemet®. Both the systems are commercially important and hence we focused mainly on the mechanical properties.

At first we prepared different compositions of CoNiAl alloy. We started work with the composition of $Co_{42}Ni_{31}Al_{27}$. Then we replaced the Co by Ni keeping Al concentration fixed. In this way, we synthesized $Co_{42}Ni_{31}Al_{27,}$ $Co_{41}Ni_{32}Al_{27}$ and $Co_{39}Ni_{34}Al_{27}$. These three samples were annealed at the 1473K/72h and quenched into cooled water. In all the samples β and γ phase were present. Here β phase is the main FSMA phase and γ phase improved the mechanical strength. The ratios in $\beta:\gamma$ varied with Co replacement by Ni where less Co shows more γ phase fraction (%) inside. And also the transition temperatures are also changed. The change in phase fractions also affected on the dynamic elastic properties of these alloys. Among these three samples $Co_{39}Ni_{34}Al_{27}$ shows 16% of γ phase, which shows the best properties among all the samples we prepared. The mechanical strength can also be enhanced by heat treatment also, where annealing at higher temperature increases the volume fraction (%) of γ. But in the sample $Co_{36}Ni_{36}Al_{28}$ the annealing at higher temperature, actually drastically effected on the structure and hence the variations in elastic moduli. We have reported all of these structures and elastic nature in room temperature. This sample was observed under ultrasonic dynamic properties. In another one CoNiAl system with the nominal composition of $Co_{37}Ni_{34}Al_{29}$ we found an interesting result due to stress locking effect. For the long time loading the structure and dynamic elastic properties were also changed.

Another composition of Fe based alloy named Finemet® has been analyzed by the physical properties at low temperature and the anomalies are observed in temperature dependent $\delta v/v$ and Q^{-1}. We prepared $Fe_{76.5}Cu_1Si_{13.5}B_9$ as the base material which was then doped my Cr and Nb to see the mechanical behaviour. These samples were partially amorphous and the Cr doped sample is showing almost fully amorphous at the as prepared condition. And finally we find anomalies in SV and IF at low temperature. There may be a structural change at low temperature which is highly effected in presence of magnetic field. This is the possibly arises from the magnetoelastic properties at low temperature and we have reported this for the first time for the Finemet alloys.

The sound velocities and internal frictions under magnetic fields were done for the first time. They were found to have very complicated relation, due to Curie temperature being near the structural transformation temperatures. We tried to analyze them as much as possible. However, to understand properly, more systems need to be studied in the same manner.

7.2. Future plan of work:

As we are working on the dynamic elastic properties of metallic alloys, the VBR technique we used for our present work, is a setup which was made by ourselves in the laboratory. Hence the apparatus needs more modification so that it can be utilized for the great variety of samples. This is the only instrument which can catch any kind of phase transition or any structural anomalies inside the materials. So there need a very high vacuum level to optimize very low signal. The temperature range should be increase from 4K up to above room temperature. And also we have develop the program we used the measurement to the labview interfacing program.

Now regarding FSMA samples, there in day by day, it is needed more and more strength material for the practical application. So we need to do work on the great variety of compositions and also heat treatment on this CoNiAl system in search of the best one. On the other hand we analyzed the Finemet alloys only in the as prepared condition. We need to annealed the sample for the formation crystalline structure inside it and to analyze the dynamic elastic properties.

References

[1] D. A. Porter, K. E. Easterling, and M. Sherif, Phase transformations in metals and alloys, (revised reprint) (CRC press, 2009).

[2] J. W. Christian, The theory of transformations in metals and alloys (Pergamon Press, 2002).

[3] F. C. Nix and W. Shockley, Rev. Mod. Phys. 10, 1 (1938).

[4] Akimasa Sakuma, J. Phys. D: Appl. Phys. 48, 164011 (2015).

[5] A. R. Troiano, Metallography, Microstructure, and Analysis 5 (2016).

[6] Akihisa Inoue, Acta materialia, 48, 279-306 (2000).

[7] M. I. Ojovan, W. E. Lee, J. Non-Cryst Solids, 356 (44–49): 2534 (2010).

[8] W. Klement, R. H. Willens, Duwez, POL, Nature. 187 (4740), 869–870 (1960).

[9] Q. Pan and R. D. James, J. Appl. Phys. 87, 4702 (2000).

[10] Y. W. Lai, N. Scheerbaum, D. Hinz, O. Gutfleisch, R. Schäfer, L. Schultz, and J. McCord, Appl. Phys. Lett. 90, 192504 (2007).

[11] F. Zuo, X. Su and K. H. Wu, Phys. Rev. B. 58, 11127 (1998).

[12] Wang, W. H. Chen, J. L. Gao, S. X. Wu, G. H. Wang, Z. Zhen, Y. F. Zhao, L. C. Zhan, J. Phys.: Condens Matter. 13, 2607 (2001).

[13] T. Kubota, T. Okazaki, Y. Furuya, T. Watanabe, J. Magn. Magn. Mater., 239, 551 (2002).

[14] E. Hornbogen and N. Jost, Le. J. de. Physique IV1, C4 199 (1991).

[15] V.A. Chernenko, E. Cesari, J. Pons, C. Segui, J. Mater. Res., 15, 1496 (2000).

[16] M. Sato, T. Okazaki, Y. Furuya, M. Wutting, Matter Trans. JIM, 44, 372 (2003).

[17] V.A. Chernenko, B. Rajini Kanth, P.K. Mukhopadhyay, S.N. Kaul, E. Villa, A. Gambardella, S. Besseghini, Appl. Phys. Lett., 93, 141904 (2008).

[18] A. A. Mendonca, J. F. Jurado, S. J.Stuard, L. E. L. Silva, G. G. Eslava, L. F.Cohen, L. Ghivelder, A. M. Gomes, J. Alloys Compd. 738, 509–514 (2018).

[18] A. Sozinov, A. Soroka, N. Lanska, M. Rames, L. Straka, K. Ullakko, Scr. Mater. 131, 33–36 (2017).

[20] T. Lawrence, P. Lindquist, K. P. Ullakko, Mullner, Mater. Sci. Eng. A, 654, 221 - 227 (2016).

[21] H. Rekik, M. Krifa, T. Bachaga, L. Escoda, J. J. Sunol, M. Khitouni, M. Chmingue, Manuf. Technol. 90, 291 - 298 (2017).

[22] K. Sumida, K. Shirai, S. Zhu, M. Taniguchi, M. Ye, S. Ueda, Y. Takeda, Y. Saitoh, I.R. Aseguinolaza, J.M. Barandiarán, Phys. Rev. B, 91 (2015).

[23] Y. Wang, C. H. Huang, H. J. Wu, X.Q. Liao, J.H. Gao, D. Wang, S. Yang, X. Song, J. Mater. Sci. 52, 12854 - 12860 (2017).

[24] D. Dye, Nat. Mater. 14, 760 - 761 (2015)

[25] J. Ju, S. T. Lou, L. Yang, T. Li, S. Hao, C. Yan, J. Electron. Mater. 46, 1390–1395 (2017)

[26] Md Sarowar Hossain, B. Rajini Kanth, P. K. Mukhopadhyay, Shap. Mem. Superelasticity, 3, 199 (2017)

[27] B. Rajini Kanth, N. V. Ramarao, A.K. Panda, R. Gopalan, A. Mitra, P. K. Mukhopadhyay, Jour. Of Alloys and Compounds 491, 22 (2010)

[28] Wyckoff, R. W. G. Crystal Structures, 2nd ed.; John Wiley: New York, NY, USA, 1963.

[29] C. Felser, B. Hillebrands, J. Phys. D Appl. Phys. 42, 080301 (2009)

[30] T. Graf, C. Felser, S. S. P. Parkin, Prog. Solid State Chem., 39, 1 - 50, (2011)

[31] Z. Deng, C. Q. Jin, Q. Q. Liu, X. C. Wang, J. L. Zhu, S. M. Feng, L. C. Chen, R. C. Yu, C. Arguello, T. Goko, Nat. Commun. 2, 1425 (2011).

[32] Adewumi Isaac POPOOLA, Turk J Phys 41, 95-103 (2017).

[33] Sasan Dadbakhsh, Mathew Speirs, Jan Van Humbeeck and Jean-Pierre Kruth, Metallic materials for 3D printing, 41(10), 765-774 (2016)

[34] S. Barbarino, Flores, E.I.S., Ajaj, R.M., Dayyani, I., Friswell, M.I., Smart Mater. Struct. 23, 063001 (2014).

[35] S. Nemat-Nasser, W.-G. Guo, Mech. Mater. 38, 463 (2006).

[36] D. C. Lagoudas, *Shape Memory Alloys: Modeling and Engineering Applications* (Springer, 2008).

[37] K. Ullakko, J. Mater. Eng. Perform. 5, 405 (1996).

[38] J. Enkovaara, A. Ayuela, A. T. Zayak, P. Entel, L. Nordström, M. Dube, J. Jalkanen, J. Impola, and R. M. Nieminen, Mater. Sci. Eng. A 378, 52 (2004).

[39] P. K. Mukhopadhyay, M. Karmakar, B. Rajini Kanth, and S. N. Kaul, J. Alloys Compd. 577, S119 (2013).

[40] V. Yamakov, J. D. Hochhalter, W. P. Leser, J. E.Warner, J. A. Newman, G. P. P. Pun, Y. Mishin, J. Mater. Sci. 51, 1204–1216 (2016).

[41] H. Seiner, J. Kopecek, P. Sedlak, L. Bodnarova, M. Landa, P. Sedmak, O. Heczko, Acta Mater. 61, 5869–5876 (2013).

[42] K. Oikawa, L. Wulff, T. Iijima, F. Gejima, T. Ohmori, A. Fujita, K. Fukamichi, R. Kainuma, and K. Ishida, Appl.Phys. Lett. 79, 3290 (2001).

[43] R. Kainuma, M. Ise, C. C. Jia, H. Ohtani, and K. Ishida, Intermetallics 4, S151, (1996).

[44] Y. Yoshizawa, S. Oguma, and K. Yamauchi, J. Appl. Phys. 64, 6044 (1988).

[45] G. Herzer, J. Magn. Magn. Mat. 157/159, 133 (1996).

[46] H. M. Ledbetter, Cryogenics 22, 653-656 (1982).

[47] G. A. Alers, Physical Acoustics. Vol IV A ed P. Mason. Academic press, New York (1968).

[48] M .S. Blanter, I. S. Golovin, H. Neuhäuser and H. –R. Sinning, Internal Friction in Metallic Materials, Springer-Verlag Berlin Heidelberg, (2007).

[49] A. S. Nowick and B. S. Berry, "Anelastic relaxation in crystalline solids", Academic Press, New York and London, 677 (1972).

[50] J.-E. Bidaux, R. Schaller and W. Benoit, 37 (3), 803-811 (1898).

[51] J. San Juan and R.B. Pérez-Sáez, Materials Science Forum, 366-368, 416-436, (2001).

[52] P. K. Mukhopadhyay and A. K. Raychaudhuri, J. Phys. E. 20, 507 (1987); J. Phys. C 21, L385 (1988); J. Appl. Phys. 67, 5235 (1990).

[53] P. K. Mukhopadhyay and S. N. Kaul, Appl. Phys. Lett. 92, 101924 (2008).

[54] M. E. McHenry, M. A. Willard, and D. E. Laughlin, *Progress in Materials Science* 44, 291–433 (1999).

[55] Y. Leng, Materials Characterization: Introduction to Microscopy and Spectroscopic Methods (JohnWiley & Sons (Asia) Pte Ltd, Singapore, 2008).

[56] B. D. Cullity, Elements of x-ray diffraction (Addison-Wesley Pub. Co., 1978).

[57] H. M. Rietveld, Acta Crystallogr. 22, 151–152 (1967).

[58] H. M. Rietveld, 2, 65–71 (1969).

[59] S.K. Pradhan, S. Bid, M. Gateshki and V. Petkov, Mater. Chem. Phys. 93, 224, (2005).

[60] S. Bid, S. K. Pradhan, J. Appl. Crystallogr. 35, 517 (2002).

[61] R. J. Hill and C. J. Howard, J. Appl. Cryst. 20, 467- 474 (1987).

[62] V. V. Khovalio, V. Novosad, T. Takagi, D. A. Filippov, R. Z. Levitin and A. N. Vasil'ev, Phys. Rev. B. 70, 174413 (2004).

[63] Low level measurements handbook (6th ed., Keithley Instruments Inc., USA, 2004).

[64] A. Migliori and J. L. Sarrao, Resonant Ultrasound Spectroscopy (Wiley, New York, 1997).

[65] J. L. Sarrao, D. Mandrus, A. Migliori, Z. Fisk, I. Tanaka, H. Kojima, P. C. Canfield and P. D. Kodali, Phys. Rev. B, 50, 13125 (1994).

[66] T. J. Ulrich, K. R. McCall and R. A. Guyer, J. Acoust. Soc. Am. 4, 111 (2002).

[67] B. S. Berry and W. C. Pritchet, Phys. Rev. Lett. 34, 1022 (1975).

[68] B. S. Berry and W. C. Pritchet, J. Appl. Phys. 52, 1865 (1981).

[69] M. Barmatz and Brage Golding, Phys. Rev. B. 9, 3064 (1974).

[70] M. Barmatz and H. S. Chen, Phys. Rev. B 9, 4073 (1974).

[71] H. M. Simpson and A. Sosin, Rev. Sci. Instrum. 48, 1392 (1977).

[72] S. Foner, Review of Scientific Instruments 30, 548 (1959).

[73] B. D. Josephson, Physics letters 1, 251 (1962).

[74] M. Youssif, A. Bahgat, and I. Ali, Egypt. J. Solids (2000).

[75] R. A. Hein, T. L. Francavilla, and D. H. Liebenberg, Magnetic Susceptibility of Superconductors and Other Spin Systems (Springer, 1991).

[76] M. Hubert-Protopescu, H. Hubert, Aluminium-cobalt-nickel ternary alloys: a comprehensive compendium of evaluated constitutional data and phase diagram. Vol. 4: Al-Cd-Ce to Al-Cu-Ru, edited by G. Petzow & G. Effenberg (Weinheim: VCH), pp. 234, (1991).

[77] Y. Murakami, D. Shindo, K. Oikawa, R. Kainuma, K. Ishida, Acta Mater., 50, 2173 (2002).

[78] Jian Liu, Hua Xie, Yanqiu Huo, Hongxing Zheng and Jianguo Li, J. Alloys Compd. 420, 145–157, (2006).

[79] FULLPROF [http://www.ill.eu/sites/fullprof/]

[80] V. A. Chernenko, Scr. Mater. 40, 523-7 (1999).

[81] I. I. Kositsyna , V. A. Zavalishin, Mater. Sci. Forum, 635, 75-80, (2019).

[82] B. R. Kanth, N. V. Ramarao, A. K. Panda, R. Gopalan, A. Mitra, P. K. Mukhopadhyay, J. Alloys Compd. 22, 491 (2010).

[83] N. Rivier, K. Adkins, J. Phys. F: Met. Phys. 5, 1745 (1975).

[84] T. Ghosh, T. Fukuda, T. Kakeshita, S. N. Kaul, P. K. Mukhopadhyay, Phys. Rev. B. 95, 140401 (2017).

[85] N. Singh, B. Borgohain, A. K. Srivastava, A. Dhar, H. K. Singh, Appl. Phys. A. 122, 237 (2016).

[86] S. Agarwal, P. K. Mukhopadhyay, J. Alloys Compd. 329, 608 (2014).

[87] S. Agarwal, E. Stern-Taulats, L.Ma˜nosa, P. K.Mukhopadhyay, J. Alloys Compd. 244, 641 (2015).

[88] M. K. Ray, K. Bagani, S. Banerjee, J. Alloys Compd. 55, 600 (2014).

[89] P K Mukhopadhyay, Studies of dynamic elastic properties of spin glass and related magnetic systems across the transition region, Thesis, IISc, Bangalore, (1989).

[90] Y. P. Varshni, Phys. Rev. B, 2, 3952 (1970).

[91] H. M. Ledbetter, W. F. Weston and E. R. Naimon, J. Appl. Phys. 46, 3855 (1975).

[92] H. M. Ledbetter, Phys. Stat. Sol. 66, 477 (1981).

[93] A. Bagchi, Suman Sarkar, S. Bysakh, S. Sarkar, P K Mukhopadhyay, J. Appl. Phys. 125, 144505 (2019).

[94] S. Sun and C. B. Murray, J. Appl. Phys., 85. 4325–4330 (1999).

[95] P Scherrer, Mathematisch-Physikalische Klasse, 2, 98-100, 1918

[96] J. Crangle and G. M. Goodman, Proc. Roy. Soc. Lond. A 321, 477 (1971).

[97] S. M. Bhagat, M. L. Spano, and K. V. Rao, J. Appl. Phys. 50, 1580 (1979).